# Department of Electrical Engineering

[redacted]

**UNIVERSITY OF COLORADO**

**BOULDER, COLORADO**


# NON-RECIPROCAL DEVICES USING SOLID STATE MAGNETOPLASMAS AT MILLIMETER AND SUBMILLIMETER WAVELENGTHS

by

Motohisa Kanda

July 1971

Prepared under Grant No. NGL06-003-088 by

Electrical Engineering Department
University of Colorado
Boulder, Colorado

for

Electronics Research Center

National Aeronautics and Space Administration

ABSTRACT

The propagation of em waves in solid state plasmas made anisotropic by a dc magnetic field becomes of interest in the construction of non-reciprocal microwave devices. This report presents theoretical and experimental investigations of this behavior for the development of isolators at millimeter and submillimeter wavelengths.

Part I of this report presents a study of a 94 GHz waveguide isolator, which consists of an annular InSb column in a circular waveguide with a longitudinal dc magnetic field and is operated at 75°K. The basic operation of the isolator is due to exclusion or absorption of em waves in the semiconductor. In a mode matching analysis the characteristic equation is solved in order to determine the propagation constants in the waveguide with the annular InSb column. The attenuation constant was then calculated by matching the fields at the ends of the plasma column. The four gyromagnetic modes excited in the plasma column as well as the four evanescent modes excited in the empty waveguide are taken into account in the analysis.

Part II of this report presents a study of reflection beam isolators at millimeter and submillimeter wavelengths using the non-reciprocal behavior in solid

state magnetoplasmas at room temperature. Non-reciprocal reflection is observed when the incident electric field is polarized in the plane of incidence and propagates transversely to a dc magnetic field. Two geometries are considered: GaAs-dielectric interface at 94 GHz; and a free space-dielectric coated InSb interface for submillimeter wavelengths (337 μm). A physical explanation for the non-reciprocal reflection based on the electron orbits in the plasma is presented.

ACKNOWLEDGEMENTS

The theoretical and experimental work described in this report was performed under the direction of Professors W.G. May and R.E. Hayes, and the author wishes to express his sincere gratitude to them for their generous donation of time and effort in guiding him throughout the course of this work.

He is also indebted to Mr. N.W. Baer and D.W. Colvin for their help in setting up the experimental instrumentation, to a number of his colleagues at the Semiconductor Device Research Laboratory, especially to J.E. Young, for his assistance in fabrication of mechanical apparatuses, and to Mrs. C.M. Hedrick for the final typing of this report.

TABLE OF CONTENTS

## LIST OF SYMBOLS

### (a) Fundamental Constants

| | | |
|---|---|---|
| $c$ | $= (\varepsilon_o \mu_o)^{-\frac{1}{2}}$ | |
| | Velocity of Light in Free Space | $= 2.998 \times 10^{8}$ m/sec. |
| $e$ | Magnitude of Electronic Charge | $= 1.602 \times 10^{-19}$ C. |
| $h$ | Plank's Constant | $= 6.624 \times 10^{-34}$ Joule-sec. |
| $\hbar$ | $= \frac{h}{2\pi}$ | $= 1.054 \times 10^{-34}$ Joule-sec. |
| $k$ | Boltzmann's Constant | $= 1.380 \times 10^{-23}$ Joule/°C. |
| $m_o$ | Mass of Free Electron | $= 9.107 \times 10^{-31}$ kg. |
| $\beta$ | $= \frac{e\hbar}{2m_o}$ Bohr Magneton | $= 9.273 \times 10^{-24}$ A-m$^2$. |
| $\varepsilon_o$ | Permittivity of Free Space | $= 8.854 \times 10^{-12}$ F/m. |
| $\mu_o$ | Permeability of Free Space | $= 1.257 \times 10^{-6}$ H/m. |

### (b) Commonly Used Symbols

| | |
|---|---|
| $\vec{a}$ | Unit Vector |
| $\vec{B}$ | Magnetic Flux Density Vector |
| $\vec{D}$ | Electric Flux Density Vector |

$\vec{E}$ Electric Field Vector

G Wave Impedance

g g Value

$\vec{H}$ Magnetic Field Vector

$\bar{\bar{I}}$ Unit Matrix

$\vec{J}$ Current Density Vector

$J_m$ Bessel Function of First Kind of Order m

$j$ $= \sqrt{-1}$

K Relative Dielectric Constant

$\bar{\bar{K}}$ Relative Dielectric Tensor

$K_L$ Relative Lattice Dielectric Constant

$$K_{\perp} = K_L - \frac{j\omega_p^2(j\omega\tau+1)\tau}{\omega[(j\omega\tau+1)^2+\omega_c^2\tau^2]}$$

$$K_x = \frac{-j\omega_p^2\omega_c\tau^2}{\omega[(j\omega\tau+1)^2+\omega_c^2\tau^2]}$$

$$K_{||} = K_L - \frac{j\omega_p^2\tau}{\omega(j\omega\tau+1)}$$

$K_+ = K_{\perp} + jK_x$

$K_- = K_{\perp} - jK_x$

$k_o = \omega\sqrt{\mu_o\varepsilon_o} = \frac{\omega}{C}$ Wave Number in Vacuum

| | |
|---|---|
| $m^*$ | Effective Mass of Electron |
| $N_m$ | Bessel Function of Second Kind of Order m |
| $n$ | Number of Electrons in Conduction Band |
| $p$ | Number of Holes in Valence Band |
| $R_H$ | Hall Coefficient |
| $T$ | Temperature |
| $t$ | Time |
| $\vec{v}$ | Electron Velocity Vector |
| $Y_o = \sqrt{\frac{\varepsilon_o}{\mu_o}}$ | Free Space Intrinsic Admittance |
| $Z_o = \sqrt{\frac{\mu_o}{\varepsilon_o}}$ | Free Space Intrinsic Impedance |
| $\alpha$ | Attenuation Constant |
| $\beta$ | Phase Constant |
| $\vec{\Gamma}$ | Propagation Vector |
| $\varepsilon_L$ | Lattice Dielectric Constant |
| $\theta$ | Angle of Incidence |
| $\lambda$ | Wavelength |
| $\lambda_c$ | Cut-off Wavelength |
| $\mu_n$ | Electron Mobility |

$\mu_p$ Hole Mobility

$\nu$ Collision Frequency

$\bar{\bar{\sigma}}$ Conductivity Tensor

$$\sigma_{\perp} = \frac{e^2 n}{m^*} \left[\frac{(j\omega\tau+1)\tau}{(j\omega\tau+1)^2+(\omega_c\tau)^2}\right]$$

$$\sigma_x = \frac{e^2 n}{m^*} \left[\frac{\omega_c\tau^2}{(j\omega\tau+1)^2+(\omega_c\tau)^2}\right]$$

$$\sigma_{||} = \frac{e^2 n}{m^*} \left[\frac{\tau}{j\omega\tau+1}\right]$$

$\tau$ Collision Time

$\omega$ Radian Frequency

$\omega_c = \frac{eB}{m^*}$ Radian Cyclotron Frequency

$\omega_p = \left(\frac{ne^2}{\varepsilon_o m^*}\right)^{\frac{1}{2}}$ Radian Plasma Frequency

(c) Symbols Used in Appendix B and C

$q^2 = \Gamma^2 + k_o^2$

$D = (\Gamma^2 + k_o^2 K_+)(\Gamma^2 + k_o^2 K_-)$

$P^t = -\Gamma(\Gamma^2 + k_o^2 K_{\perp})/D$

$$P^r = \Gamma(\Gamma^2 + k_o^2 K_\perp)/D$$

$$R = j\omega\mu_o k_o^2 K_x/D$$

$$Q^t = \Gamma k_o^2 K_x/D$$

$$Q^r = -\Gamma k_o^2 K_x/D$$

$$S = j\omega\mu_o(\Gamma^2 + k_o^2 K_\perp)/D$$

$$a = (\Gamma^2 + k_o^2 K_\perp)K_{||}/K_\perp$$

$$b^t = j\omega\mu_o \Gamma K_x/K_\perp$$

$$b^r = -j\omega\mu_o \Gamma K_x/K_\perp$$

$$c = \Gamma^2 + k_o^2 K_+ K_-/K_\perp$$

$$d^t = -j\omega\varepsilon_o \Gamma K_x K_{||}/K_\perp$$

$$d^r = j\omega\varepsilon_o \Gamma K_x K_{||}/K_\perp$$

$$P_{1,2}^2 = \frac{1}{2}\left[\Gamma^2(K_{||}/K_\perp + 1) + k_o^2(K_{||} + K_+K_-/K_\perp)\right]$$

$$\pm \frac{1}{2}\sqrt{\{\Gamma^2(K_{||}/K_\perp - 1) + k_o^2(K_{||} - K_+K_-/K_\perp)\}^2 + 4\Gamma^2 k_o^2 K_{||} K_x^2/K_\perp^2}$$

$$h^t_{1,2} = (a - p^2_{1,2})/b^t$$

$$h^r_{1,2} = (a - p^2_{1,2})/b^r$$

$$\ell^t_{1,2} = p^2_{1,2}R/b^t - 1/\Gamma$$

$$\ell^r_{1,2} = p^2_{1,2}R/b^r + 1/\Gamma$$

$$L^t_{1,2} = p^2_{1,2}S/b^t - (1/\Gamma)(K_\perp/K_x)$$

$$L^r_{1,2} = p^2_{1,2}S/b^r + (1/\Gamma)(K_\perp/K_x)$$

$$Y^t_{1,2} = (p^2_{1,2}p^t + \Gamma)/b^t$$

$$Y^r_{1,2} = (p^2_{1,2}p^r - \Gamma)/b^r$$

$$y^t_{1,2} = p^2_{1,2}Q^t/b^t$$

$$y^r_{1,2} = p^2_{1,2}Q^r/b^r$$

$$\xi = -\Gamma/q^2$$

$$\zeta = jk_o/q$$

$$S_1(p_1x) = \frac{jm}{x}\ell^t_2 J_m(p_1x) + L^t_2 p_1 J'_m(p_1x)$$

$$S_2(p_1x) = \frac{jm}{x}\ell^t_2 N_m(p_1x) + L^t_2 p_1 N'_m(p_1x)$$

$$S_3(p_2x) = \frac{jm}{x}\ell^t_1 J_m(p_2x) + L^t_1 p_2 J'_m(p_2x)$$

$$S_4(p_2x) = \frac{jm}{x} \ell_1^t N_m(p_2x) + L_1^t P_2 N_m'(p_2x)$$

$$T_1(p_1x) = \frac{jm}{x} y_2^t J_m(p_1x) + Y_2^t P_1 J_m'(p_1x)$$

$$T_2(p_1x) = \frac{jm}{x} y_2^t N_m(p_1x) + Y_2^t P_1 N_m'(p_1x)$$

$$T_3(p_2x) = \frac{jm}{x} y_1^t J_m(p_2x) + Y_1^t P_2 J_m'(p_2x)$$

$$T_4(p_2x) = \frac{jm}{x} y_1^t N_m(p_2x) + Y_1^t P_2 N_m'(p_2x)$$

# Chapter 1

## INTRODUCTION

The propagation of em waves in solid state plasma made anisotropic by a magnetic field becomes of interest in the construction of non-reciprocal microwave devices. For example, this non-reciprocity may be expected in a system in which circularly polarized em fields propagate along the dc magnetic field. When the direction of propagation is reversed, it is necessary to reverse the dc magnetic field in order to achieve a situation geometrically equivalent to the original. Since the procession of the electrons about the dc magnetic field has a definite sense, the electric current associated with this procession is also reversed with the dc magnetic field. Thus, the properties of the plasma are altered, and different propagation characteristics for the opposing directions may be expected.

Of course, an anisotropy can be introduced by the complexity due to the symmetry and band structure of crystals, but we will assume that in the absence of a magnetic field, the unbounded solid state plasma is isotropic for electromagnetic wave propagation. When the plasma is placed in a dc magnetic field, the field causes the electrons to orbit perpendicular to the

field, and the solid state plasma is no longer isotropic. In this case the propagation characteristics of the medium are no longer described by the plasma and collision frequencies, but the cyclotron frequency also is a controlling parameter. One of the great advantages of utilization of semiconductors in the development of non-reciprocal devices lies in the flexibility of these parameters.

Many investigations dealing with anisotropic materials, particularly ferrites, have been carried out since D. Polder [1949] and C.L. Hogan [1953] showed possibilities of practical non-reciprocal microwave devices using the tensor properties of the permeability. Recently the solid state magnetoplasma has been used as a basis of non-reciprocal microwave devices using the tensor properties of the dielectric constant. These non-reciprocal devices can be classified into Faraday rotation, field displacement, plasma resonance and reflection beam devices. In the next few paragraphs various types of microwave isolators using ferrites or semiconductors are reviewed.

A microwave ferrite isolator that uses Faraday rotation was developed by B. Lax and K.J. Button [1955]. Similar devices using solid state plasmas have also been built [Libchaber and Veilex, 1962; Kuno and Hershberger, 1967]. The basis of operation of these

devices is that right and left circularly polarized (henceforth abbreviated cp) waves travel with different phase velocities through the plasma along the longitudinal dc magnetic field. A plane wave, which can be regarded as the sum of right and left cp waves, will therefore undergo Faraday rotation.

The field displacement isolator using a ferrite was first discussed by A.G. Fox, S.E. Miller and M.T. Weiss [1955]. A solid state plasma in the presence of a transverse dc magnetic field was used for a field displacement waveguide isolator by M. Toda [1964], and R. Hirota and K. Suzuki [1966]. When a transverse magnetic field is applied to a plasma in a waveguide, a Hall current is produced by the dc magnetic field and microwave electric fields. The surface charge on the plasma and the rf magnetic field resulting from the Hall current couple with em waves. This coupling makes em waves excited strongly on one side of the waveguide and weakly on the other side. Therefore reversing the direction of propagation interchanges the waveguide side on which the microwave power flow occurs. A resistance strip attached to the side of the plasma attenuates the reverse wave, and hardly affects the forward wave.

B.J. Duncan and L. Swern [1957] developed a plasma resonance isolator using a ferrite in a coaxial

waveguide. A similar isolator in which a solid state plasma partially fills a circular waveguide was developed by B.R. McLeod and W.G. May [1968,1971] in this laboratory. The plasma can be made to exhibit a nearly zero permittivity to the left cp wave and non-zero permittivity to the right cp wave. The operation of the isolator is due to the exclusion or absorption of the microwave signal, depending on the direction of rotation of cp waves with respect to the longitudinal magnetic field. It was also found that mode coupling improved the performance of this isolator [McLeod, 1968; McLeod and May, 1971].

Reflection devices in which the desired em waves do not propagate through or along the solid state magnetoplasma but are reflected off its surface have been developed in this laboratory [Seaman, 1969; Kanda, et al., 1970]. Non-reciprocal phenomena are observed when the incident electric field vector is polarized in the plane of incidence and its propagation is perpendicular to a dc magnetic field which is parallel to the surface of the plasma. The useful frequency range of this reflection device is in the far infrared.

Theoretical and experimental investigations of non-reciprocal effects in solid state magnetoplasmas for the development of isolators for use at millimeter and sub-millimeter wavelengths are presented in this thesis.

The purpose of Part I is to present a study of semiconductor waveguide isolators at 94 GHz. These millimeter waveguide isolators consist of circular waveguide with an annular column of a semiconductor plasma in a longitudinal dc magnetic field. The basic operation of the isolator is due to exclusion or absorption of em waves in the semiconductor. The purpose of Part II is to discuss some anisotropic effects which may be used for reflection beam isolators at millimeter and submillimeter wavelengths. Non-reciprocal reflection from solid state magnetoplasmas can be observed when the incident electric field is polarized in the plane of incidence and propagates transversely to a dc magnetic field.

## Chapter 2

## PROPAGATION OF EM WAVES IN A MAGNETOPLASMA

In terms of the electronic energy bands of semiconductors, the effect of the carriers may be intraband or interband in nature. The intraband effects will be simply referred to as free carrier effects. On the other hand, the interband effects involve two energy bands. Since the photon energies at millimeter and submillimeter wavelengths are significantly smaller than the energy of the nearest neighboring band (typically 0.1~2 eV or more), the interband effects in semiconductors can usually be neglected. Moreover with sufficiently small dc magnetic fields (~5 kG) used for 94 GHz waveguide isolator experiments at 75°K, the difference of the energies between successive Landau levels in semiconductors, $\hbar\omega_c$, is about 46°K in temperature units and also that between Zeeman splittings, $g\beta B$, is about 23°K in temperature units. Similarly IR reflection beam isolator experiments at room temperature (~300°K) require the dc magnetic field of 15 kG, and $\hbar\omega_c$ is about 138°K and $g\beta B$ is about 69°K in temperature units. Therefore in our experiments throughout the thesis where $kT \gg \hbar\omega_c$ and $g\beta B$, the quantum effects due to Landau levels and Zeeman splittings can be neglected.

The non-reciprocal devices presented in this thesis depend in principle on the numerical details of the boundary conditions or more generally, of the geometrical configuration. In fact guided microwave propagation through a plasma waveguide is quite different from the plane wave propagation in unbounded plasmas. Here wave propagation depends strongly upon the waveguide geometries, i.e., the guide wavelength, the waveguide cutoff condition and the waveguide modes. Therefore the actual performance of the non-reciprocal devices could be predicted only as the result of lengthy computation. However, since the basic properties of solid state plasmas with a dc magnetic field in the waveguide remain largely unaffected, it appears advisable to review in broad terms the characteristics of the wave propagation which lead to the discovery of the conditions of non-reciprocity for em wave propagation in a magnetoplasma.

## 2-1 Wave Propagation in Infinite Solid State Magnetoplasma

A convenient and useful stratagem for dealing with electromagnetic waves in a solid state plasma in a magnetic field is to characterize the medium as a complex tensor dielectric constant. This is calculated for the simplest case where a mass is isotropic, and a

collision time is isotropic and independent of energy. The case of energy dependent collision time is discussed in Appendix A. Anisotropy of the conductivity is expected from the fact that the charged particles are forced to rotate about the magnetic field lines with the cyclotron frequency, $\omega_c$, and the electric field of the wave develops a component perpendicular to the motion.

In the case of a single type of charge carrier and intraband effects only, the equation of motion is written in the form:

$$m^* \frac{d\vec{v}}{dt} = e(\vec{E}+\vec{v}\times\vec{B}) - \frac{m^*\vec{v}}{\tau} , \qquad (2\text{-}1)$$

including the Lorentz and Langevin forces. Maxwell's equations are given by

$$\nabla\times\vec{H} = \frac{\partial\vec{D}}{\partial t} + \vec{J} \qquad (2\text{-}2)$$

$$\nabla\times\vec{E} = - \frac{\partial\vec{B}}{\partial t} \qquad (2\text{-}3)$$

It is assumed that the wave varies sinusoidally in time and has propagation constant $\vec{\Gamma}$, i.e., $\exp(j\omega t-\vec{\Gamma}\cdot\vec{r})$. Then making use of the relation, $\vec{J} = ne\vec{v} = \bar{\bar{\sigma}}\vec{E}$,

$$\nabla\times\vec{H} = j\omega\varepsilon_L\vec{E} + \bar{\bar{\sigma}}\vec{E} = j\omega\varepsilon_o(K_L\bar{\bar{I}} + \frac{\bar{\bar{\sigma}}}{j\omega\varepsilon_o})\vec{E} = j\omega\varepsilon_o\bar{\bar{K}}\vec{E} . \qquad (2\text{-}4)$$

We linearize by including in $\vec{B}$ only the applied dc magnetic field $\vec{B}_o$ and neglecting the rf magnetic field.

Without loss of generality we adopt the Cartesian coordinate system where the applied dc magnetic field is along the positive z-axis. The tensor dielectric constant $\bar{\bar{K}}$ then becomes

$$\bar{\bar{K}} = \begin{vmatrix} K_{\perp} & -K_{\times} & 0 \\ K_{\times} & K_{\perp} & 0 \\ 0 & 0 & K_{\parallel} \end{vmatrix} \tag{2-5}$$

where

$$K_{\perp} = K_L + \frac{\sigma_{\parallel}}{j\omega\varepsilon_o} = K_L - \frac{j\omega_p^2}{\omega}\left[\frac{(j\omega\tau+1)\tau}{(j\omega\tau+1)^2+(\omega_c\tau)^2}\right] \tag{2-6}$$

$$K_{\times} = \frac{\sigma_{\times}}{j\omega\varepsilon_o} = -\frac{j\omega_p^2}{\omega}\left[\frac{\omega_c\tau^2}{(j\omega\tau+1)^2+(\omega_c\tau)^2}\right] , \tag{2-7}$$

$$K_{\parallel} = K_L + \frac{\sigma_{\parallel}}{j\omega\varepsilon_o} = K_L - \frac{j\omega_p^2}{\omega}\left[\frac{\tau}{j\omega\tau+1}\right] . \tag{2-8}$$

Definitions of all symbols, $\omega_p$, $\omega_c$, $\tau$ and etc. are given in the List of Symbols. The relation between the propagation constant $\vec{\Gamma}$ and the tensor dielectric constant $\bar{\bar{K}}$ is obtained from Eq.(2-3) and (2-4). The result is given in the standard textbook (Allis, et al., 1963):

$$\vec{\Gamma}\times(\vec{\Gamma}\times\vec{E}) - k_o^2\bar{\bar{K}}\cdot\vec{E} = 0 \tag{2-9}$$

In the Cartesian coordinate system where the dc magnetic field $\vec{B}_o$ lies in the z-direction, and the propagation constant $\vec{\Gamma}$ is in the x-z plane with the angle $\theta$ from z-axis as shown in Fig. 2-1, one can obtain three homogeneous linear equations in $E_x$, $E_y$ and $E_z$:

$$\begin{vmatrix} k_o^2 K_\perp + \Gamma^2 \cos^2\theta & -k_o^2 K_x & -\Gamma^2 \sin\theta\cos\theta \\ k_o^2 K_x & k_o^2 K_\perp + \Gamma^2 & 0 \\ -\Gamma^2 \sin\theta\cos\theta & 0 & k_o^2 K_{||} + \Gamma^2 \sin\theta \end{vmatrix} \begin{vmatrix} E_x \\ E_y \\ E_z \end{vmatrix} = 0 \tag{2-10}$$

A non-zero solution exists only when the determinant of the coefficients vanishes. Then the dispersion relation becomes a biquadratic equation, which is known as the Appleton-Hartree formula:

$$A\Gamma^4 + B\Gamma^2 + C = 0 \quad , \tag{2-11}$$

where

$$A = K_\perp \sin^2\theta + K_{||} \cos^2\theta \quad , \tag{2-12}$$

$$B = k_o^2 K_+ K_- \sin^2\theta + k_o^2 K_{||} K_\perp (1+\cos^2\theta) \quad , \tag{2-13}$$

$$C = k_o^4 K_+ K_- K_{||} \quad , \tag{2-14}$$

and

$$K_\pm = K_\perp \pm j K_x \quad . \tag{2-15}$$

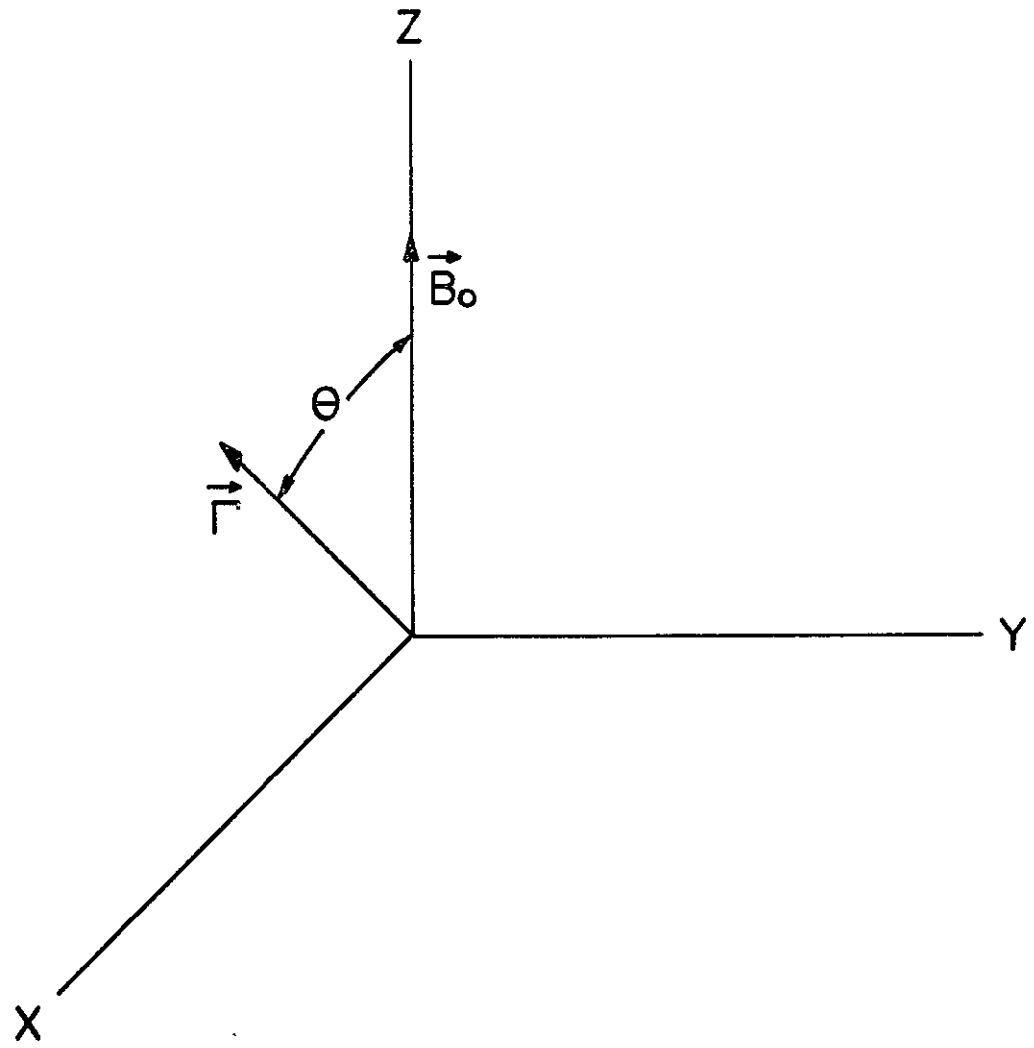


Fig. 2-1. Orientation of Coordinate Axes with Respect to Propagation Constant $\Gamma$ and dc Magnetic Field $B_o$.

Since most experiments are performed with the propagation vector either parallel or perpendicular to the dc magnetic field, it is most instructive to consider these two cases individually and to solve the dispersion equation.

## 2-2 Longitudinal Propagation ($\theta=0$)

For the longitudinal case, the propagation constant $\vec{\Gamma}$ is parallel to the dc magnetic field $\vec{B}_o$ along the z direction. By setting $\theta=0$ in Eq.(2-10) the secular equation becomes

$$\begin{vmatrix} k_o^2K_\perp+\Gamma^2 & -k_o^2K_x & 0 \\ k_o^2K_x & k_o^2K_\perp+\Gamma^2 & 0 \\ 0 & 0 & k_o^2K_\parallel \end{vmatrix} \begin{Vmatrix} E_x \\ E_y \\ E_z \end{Vmatrix} = 0 \qquad (2\text{-}16).$$

Then one finds that $E_z=0$, i.e., the propagating wave is TEM. By defining the right (+) and left (-) cp waves,

$$E_\pm = E_x \pm jE_y \qquad (2\text{-}17)$$

it is possible to decouple the above equations, and the propagation constants for the right and left cp waves are given by

$$\Gamma_{\pm}^2 = -k_o^2[K_{\perp} \pm jK_x] = -k_o^2 \left[K_L - \frac{j\omega_p^2}{\omega} \cdot \left\{\frac{\tau}{1+j\tau(\omega\pm\omega_c)}\right\}\right] . \qquad (2\text{-}18)$$

A relatively simple situation occurs when the plasma is lossless, i.e., $\tau \to \infty$ and the wave frequency $\omega$ is much smaller than the cyclotron frequency $\omega_c$. Then Eq.(2-18) becomes

$$\Gamma_{\pm}^2 = -k_o^2 \left[K_L \pm \frac{\omega_p^2}{\omega\omega_c} + \frac{\omega_p^2}{\omega_c^2}\right] . \qquad (2\text{-}19)$$

In this case the cyclotron orbits are almost closed ($\omega_c\tau >> 1$), and the carriers are essentially tied to magnetic lines of force and must move with them. The amplitude of oscillation induced by the electric field $\vec{E}$ of the wave in a direction at right angles to $\vec{B}_o$ and $\vec{E}$, the Hall direction, is the same for all carriers and is independent of mass in a first order approximation. When the plasma is not compensated, the nature of the wave is dominated by the Hall currents. This is called a Helicon wave. When the plasma is compensated, the electric current in the Hall direction (the Hall current) is very small because equal densities of positive and negative charge oscillate in phase with equal amplitudes. Assuming that electron-hole interaction is unimportant, one can add their contributions independently term by term in the dielectric tensor in

the calculation of the propagation constant. This is called an Alfvén wave.

The semiconductor materials used typically as the solid state plasmas are InSb, GaAs, Si and Ge. The electron mobility of these materials is typically between one and two orders of magnitude greater than that of holes. Thus usually only contributions due to electrons need be considered in order to investigate the propagation characteristics in solid state plasmas.

## 2-3 Transverse Propagation ($\theta=90°$)

In the case of the transverse propagation, the propagation constant $\vec{\Gamma}$ is along the x direction, perpendicular to the dc magnetic field $\vec{B}_o$ along the z-axis as before Fig. [2-1]. Then three homogeneous linear equations in $E_x$, $E_y$, and $E_z$ are obtained by setting $\theta=90°$ in Eq.(2-10).

$$\begin{vmatrix} k_o^2 K_\perp & -k_o^2 K_x & 0 \\ k_o^2 K_x & k_o^2 K_\perp + \Gamma^2 & 0 \\ 0 & 0 & k_o^2 K_{||} + \Gamma^2 \end{vmatrix} \begin{vmatrix} E_x \\ E_y \\ E_z \end{vmatrix} = 0 \qquad (2\text{-}20)$$

It is noted that, for the case of the transverse

propagation, there is a component of the electric field $E_x$ along the direction of the propagation by virtue of the Hall current. Because of this longitudinal component of the electric field, the existence of space charge may be expected. The dielectric relaxation time $\varepsilon/\sigma$, with which any space charge disappears, is order of $10^{-13}$ to $10^{-14}$sec for the semiconductor materials used in the experiments described herein. Since we are dealing with phenomena of period $10^{-11}$ to $10^{-12}$sec, we can neglect the space charge. This is also confirmed from the fact that the space charge calculated from the longitudinal component of electric field through the Poisson's equation is indeed negligible, and hence the charge neutrality condition is valid.

The propagation constant for the case of the transverse propagation with the incident em electric field parallel to the dc magnetic field is given by

$$\Gamma_{||}^2 = -k_o^2 K_{||} = -k_o^2 \left[K_L - j \frac{\omega_p^2}{\omega} \frac{\tau}{j\omega\tau+1}\right] \qquad (2\text{-}21)$$

This mode propagates independently of the dc magnetic field. For transverse propagation with the electric field perpendicular to the dc magnetic field ($E_z$=0), one obtains

$$\Gamma_{\perp}^2 = -k_o^2 \frac{K_{\perp}^2+k_x^2}{K_{\perp}} = -k_o^2 \frac{K_+K_-}{K_{\perp}} \qquad (2\text{-}22)$$

This mode is generally elliptically polarized in a plane perpendicular to the dc magnetic field. It should be noted that the propagation constant for the transverse direction is reciprocal, that is, reversal of the direction of the propagation (or alternatively, the direction of the dc magnetic field) does not change the propagation constant. However, the reflection coefficient for a wave incident on the magnetoplasma where the electric field is in the plane of incidence is non-reciprocal, and this is considered for the development of non-reciprocal devices for use at millimeter and submillimeter wavelengths in Part II.

# PART I

## NON-RECIPROCAL WAVEGUIDE ISOLATORS FOR USE AT MILLIMETER WAVELENGTHS

The purpose of Part I is to present a theoretical and experimental study of the design of a new semiconductor waveguide isolator at 94 GHz where the atmosphere has a window and attenuations are frequently as low as 1 or 2 db. In Chapter 3 a theoretical analysis of propagation of em waves in a circular waveguide containing an annular column of a solid state magnetoplasma is given. First a heuristic argument based on the exclusion or absorption of the em waves due to the magnetoplasma is presented. Second a mode matching analysis (henceforth abbreviated MMA) is employed in the theoretical analysis. Chapter 4 presents the experimental apparatus and procedures used to measure the characteristics of propagation in the circular waveguide containing the annular column of the solid state magnetoplasma. The properties of the material used in the experiments are also given. In Chapter 5 the experimental results are given along with the theoretical results from the approximate theory and from MMA. The correlation between the experimental and theoretical results and the validity of the assumptions made in the approximate theory are

discussed. Chapter 6 presents the summary of the work of Part I and conclusions.

## Chapter 3

# PROPAGATION CHARACTERISTICS OF CIRCULAR WAVEGUIDE CONTAINING AN ANNULAR MAGNETOPLASMA COLUMN

The propagation characteristics of em waves in a circular waveguide partially filled with a plasma have been investigated extensively examining the effect of a plasma upon waveguide modes. For example, R.N. Carlile [1966] measured the propagation constants of the $TE_{11}$ modes in a cylindrical waveguide partially filled with a gaseous plasma in a longitudinal dc magnetic field and observed that right and left cp waves travel with different propagation constants. The theoretical and experimental study of a circular 35 GHz waveguide containing a coaxial InSb rod was done extensively by B.R. McLeod and W.G. May [1968, 1971].

The purpose of this chapter is to present a general theoretical analysis of the characteristics of microwave propagation in a circular waveguide containing a finite length of an annular plasma column with a longitudinal dc magnetic field, and a more specialized theoretical study of a 94 GHz waveguide isolator employing this geometry. The basic operation of the isolator depends on the exclusion or absorption of cp waves by the plasma. The extent of the exclusion

or absorption depends on the sense of the circular polarization of the em wave with respect to the vector direction of the longitudinal dc magnetic field.

## 3-1 Effect of Nearly Zero Permittivity on Circularly Polarized Waves

With a longitudinal dc magnetic field on the plasma column, the total dielectric constant of the material due to both lattice and free carriers seen by the em waves depends on the direction of the circular polarization with respect to the longitudinal magnetic field. The total relative dielectric constant derived in Section 2-2 has the form:

$$K_{\pm} = K_{\perp} \pm jK_{\times} = K'_{\pm} + jK''_{\pm} \tag{3-1}$$

where

$$K'_{\pm} = K_L - \frac{\omega_p^2 \tau^2 (\omega \pm \omega_c)}{\omega[1+\tau^2(\omega\pm\omega_c)^2]} \tag{3-2}$$

$$K''_{\pm} = -\frac{\omega_p^2 \tau}{\omega[1+\tau^2(\omega\pm\omega_c)^2]} \quad . \tag{3-3}$$

The subscript ± refers to the right and left cp components in the direction of the dc magnetic field. It is readily seen that the real part of the dielectric constant could be relatively large for a microwave signal circularly polarized one way but very low or even negative for the opposite cp wave and the imaginary

part small in both cases. This characteristic was utilized for the development of the non-reciprocal devices at millimeter wavelengths by exciting a right or left cp em wave in the circular waveguide containing the annular plasma column as discussed in the next section.

### 3-1-1 Approximate Theory for Attenuation Coefficient

Consider the configuration shown in Fig. [3-1]. Using a heuristic argument let us estimate the ratio of the electric field strength in the annular plasma column to the field in the center section of air-filled region. It is assumed that the fields both in the center section of the air-filled region and in the annular plasma column are of $TE_{11}$ mode pattern. The amplitude of field in each region can be, however, drastically different and depends on the dielectric constant of each region. Of course, the above assumption is not truly valid and will not be used in MMA in the next section.

Using a simple static analysis the ratio of the field concentrations is

$$\frac{E_i}{E_o} = \frac{2}{1+\frac{1}{K}} \tag{3-4}$$

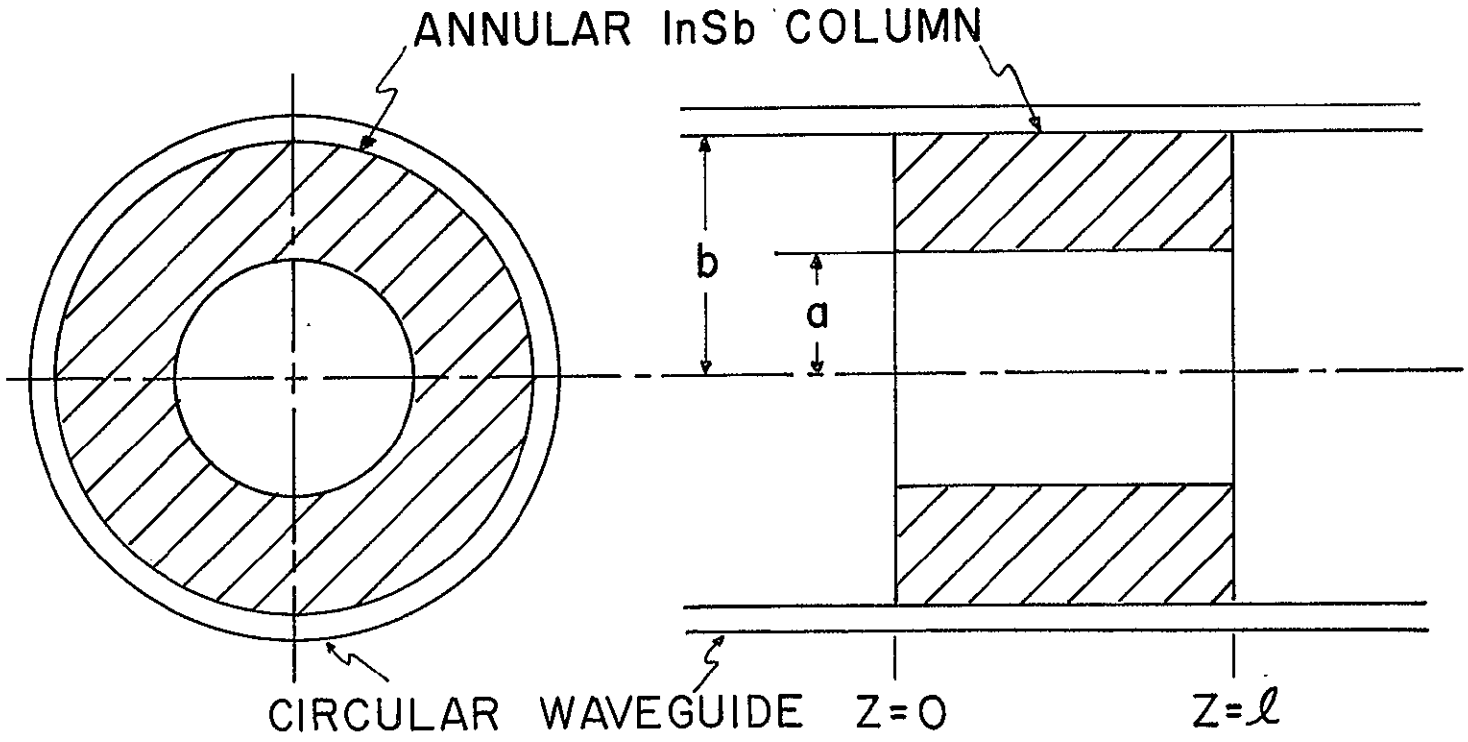


Fig. 3-1. Circular Waveguide Containing an Annular InSb Column

where K is the relative dielectric constant of the solid state magnetoplasma, and $E_i$ and $E_o$ are the uniform fields in the air-filled center section and in the annular column, respectively.

If the dc magnetic field is adjusted so that $K_-'$ as in Eq.(3-1) is close to zero, it appears reasonable from Eq.(3-4) that the left cp waves are strongly excited in the annular plasma column. Thus, the wave propagates almost exclusively inside the annular plasma column, and because of the lossy part of the dielectric constant of the plasma, much of the left cp wave will be absorbed by the plasma and dissipated as heat. On the other hand, the same em wave traveling from the opposite direction with respect to a longitudinal dc magnetic field is right circularly polarized. It is predicted from Eq.(3-4) that the right cp wave is largely excluded from the annular plasma column because of large $K_+'$ (~32) and is only slightly absorbed by the plasma.

Let us examine the attenuation coefficient using the approximate model discussed above. Consider the infinitely long annular plasma column placed in a uniform em field with the propagation direction parallel to the axis of the column. Assuming that the transverse fields in the annular plasma column are approximately uniform for both polarizations of the em

waves, the power dissipation per unit length in the plasma annulus is

$$P_{diss} = \frac{1}{2}\sigma_{\pm}|E_o|^2 A_o = \frac{1}{2}\omega\varepsilon_o K''_{\pm}|E_o|^2 A_o \quad , \qquad (3\text{-}5)$$

where $E_o$ is the field inside the annular plasma column and $A_o$ is the area of its cross section. From the foregoing discussion, the field inside the annular plasma column is also assumed to be a uniform TE mode and the power flow inside the annular plasma column $P_o$ is then approximately given by

$$P_o = \frac{1}{2}\frac{|E_o|^2}{\eta_o} A_o = \frac{1}{2}\frac{R_e\sqrt{K_{\pm}}}{Z_o}|E_o|^2 A_o\left[1-\left(\frac{\lambda}{\lambda_c}\right)^2\right]^{\frac{1}{2}} , \qquad (3\text{-}6)$$

where $\eta_o$ is the impedance of the TE mode in the annular plasma column. Similarly the power flow in the center section of the air-filled region $P_i$ is given by

$$P_i = \frac{1}{2}\frac{|E_i|^2}{Z_o} A_i \quad , \qquad (3\text{-}7)$$

where $E_i$ is the field in the air-filled center section and $A_i$ is the area of its cross section. By neglecting the reflections at the plasma boundary, the approximate attenuation coefficient $\alpha$ for both senses of the circular polarization of the em waves due to absorption in the plasma is found (by dividing the dissipated power by the total power flow) to be

$$2\alpha_{\pm} = \frac{\frac{1}{2}\omega\varepsilon_o K''_{\pm}|E_o|^2 A_o}{\frac{1}{2}\frac{R_e\sqrt{K_{\pm}}}{Z_o}|E_o|^2 A_o\left[1-\left(\frac{\lambda}{\lambda_c}\right)^2\right]^{\frac{1}{2}} + \frac{1}{2}\frac{|E_i|^2}{Z_o} A_i} \quad . \qquad (3\text{-}8)$$

Using Eq.(3-4) to eliminate the $E_i$ and $E_o$, one obtains for the approximate attenuation coefficient:

$$\alpha_{\pm} = \frac{1}{2} \frac{\omega\varepsilon_o Z_o K''_{\pm} |1+K_{\pm}|^2 A_o}{R_e\sqrt{K_{\pm}}|1+K_{\pm}|^2[1-(\frac{\lambda}{\lambda_c})^2]^{\frac{1}{2}} A_o + 4|K_{\pm}|^2 A_i} \quad . \quad (3\text{-}9)$$

This expression is used to estimate the attenuation coefficient in the annular plasma column and is compared with that from MMA discussed in the next section.

## 3-2 Mode Matching Analysis to Boundary Value Problem

In the previous section, it is assumed that the field configuration is of $TE_{11}$ mode pattern even in the presence of the plasma. However, such a simplification is not truly applicable and will not be used in the present analysis, because a single incident mode can excite infinite number of gyromagnetic modes at the ends of plasma column. These modes in turn excite an infinite number of TE and TM modes in the empty circular waveguide. Most of these modes are evanescent but even so must be included along with the propagating modes in the rigorous treatment of the boundary conditions.

The general calculations of the reflection and transmission coefficients of a finite-length section of the annular magnetoplasma column consist of the following two steps:

1) Determination of the propagation constants of the gyromagnetic modes in the section of the annular magnetoplasma column, $0 \leq z \leq \ell$.
2) Use of these propagation constants to match the boundary conditions at the ends of plasma column, $z=0,\ell$. Since the gyromagnetic modes in the section of the annular magnetoplasma column do not form orthogonal sets, the point-matching method is employed to determine the reflection and transmission coefficients at each boundary, $z=0,\ell$.

These steps will be performed in Section (3-2-1) and (3-2-2).

### 3-2-1 Characteristic Equation for Waveguide with Annular Homogeneous Magnetoplasma Column

The waveguide system considered here is illustrated in Fig. [3-1]. It consists of an annular homogeneous plasma column with axis parallel to a dc magnetic field in the z-direction.

In terms of the complex tensor dielectric constant $\bar{\bar{K}}$ given in Eq.(2-5) and for the fields that vary as $\exp(j\omega t)$, Maxwell's equations inside the annular plasma column are given by

$$\nabla \times \vec{E} = -j\omega\mu_o \vec{H} \tag{3-10}$$

$$\nabla\times\vec{H} = j\omega\varepsilon_o\bar{\bar{K}}\cdot\vec{E} \quad , \tag{3-11}$$

and

$$\nabla\cdot(\varepsilon_o\bar{\bar{K}}\cdot\vec{E}) = 0 \quad , \tag{3-12}$$

$$\nabla\cdot(\mu_o\vec{H}) = 0 \quad . \tag{3-13}$$

Since the solutions of the em fields satisfying the Maxwell's equations have a z-dependence of the form $\exp(-\Gamma z)$, where the propagation constant $\Gamma$ is independent of z, it is convenient to make following separations:

$$\vec{E} = \vec{E}_T + \vec{a}_z E_z \quad , \tag{3-14}$$

$$\vec{H} = \vec{H}_T + \vec{a}_z H_z \quad , \tag{3-15}$$

$$\nabla = \nabla_T + \vec{a}_z \frac{\partial}{\partial z} = \nabla_T + \vec{a}_z(-\Gamma) \quad . \tag{3-16}$$

The coupled wave equations describing the longitudinal components of the em waves in the region of the annular homogeneous plasma column $a\leq r\leq b$ are given by A. Bers [1963]:

$$\nabla_T^2 E_z + aE_z = bH_z \quad , \tag{3-17}$$

$$\nabla_T^2 H_z + cH_z = dE_z \quad , \tag{3-18}$$

where

$$a = (\Gamma^2+k_o^2K_\perp)\frac{K_{\parallel\perp}}{K_\perp} \quad , \quad b = j\omega\mu_o\Gamma\frac{K_x}{K_\perp}$$

$$c = \Gamma^2 + k_o^2 \frac{K_+ K_-}{K_\perp} \quad , \quad d = -j\omega\varepsilon_o \Gamma \frac{K_x K_{\parallel}}{K_\perp} \quad .$$

This coupled set of second-order equations can be transformed into an uncoupled set of fourth-order equations:

$$[\nabla_T^4 + (a+c)\nabla_T^2 + (ac-bd)]E_z = 0 \quad , \qquad (3\text{-}19)$$

and

$$[\nabla_T^4 + (a+c)\nabla_T^2 + (ac-bd)]H_z = 0 \quad . \qquad (3\text{-}20)$$

By admitting solutions of the form $\exp(-j\vec{p}\cdot\vec{r}_T)$ for the transverse components of the em waves in the region of the annular plasma column $a \leq r \leq b$, the dispersion relation is given by

$$p^4 - (a+c)p^2 + (ac-bd) = 0 \quad . \qquad (3\text{-}21)$$

The longitudinal components of the electric field can be obtained from the following differential equation:

$$(\nabla_T^2 + p_i^2)E_{zi} = 0 \quad . \qquad (3\text{-}22)$$

The acceptable solution which describes the longitudinal component of the electric field inside the plasma ($a \leq r \leq b$) is expressed by the linear combination of ordinary Bessel functions and Neumann functions:

$$E_z = [AJ_m(p_1 r) + BN_m(p_1 r) + CJ_m(p_2 r) + DN_m(p_2 r)]e^{jm\phi - \Gamma z} \quad . \qquad (3\text{-}23)$$

The longitudinal component of magnetic field is given by

$$H_z = [h_1\{AJ_m(p_1r)+BN_m(p_1r)\}$$

$$+h_2\{CJ_m(p_2r)+DN_m(p_2r)\}]e^{jm\phi-\Gamma z} \qquad (3\text{-}24)$$

where

$$h_{1,2} = \frac{a-p_{1,2}^2}{b} = \frac{d}{c-p_{1,2}^2}$$

The transverse components of the electric and magnetic fields can be derived after lengthy tedious computations and are given in Appendix B.

The wave equations in the center section of the air-filled region (r<a) are

$$\nabla_T^2 E_z^o + q^2 E_z^o = 0 \qquad (3\text{-}25)$$

and

$$\nabla_T^2 H_z^o + q^2 H_z^o = 0 \qquad (3\text{-}26)$$

where

$$q^2 = \Gamma^2 + k_o^2 .$$

Two independent solutions which describe the longitudinal components of the electric and magnetic fields in the center section of the air-filled region are

$$E_z^o = UJ_m(qr)e^{jm\phi-\Gamma z} \qquad (3\text{-}27)$$

and

$$H_z^o = VJ_m(qr)e^{jm\phi-\Gamma z} \qquad (3\text{-}28)$$

Using

$$\vec{E}_T^o = -\frac{\Gamma}{q^2}\nabla_T E_z^o + \frac{j\omega\mu_o}{q^2}\vec{a}_z \times \nabla_T H_z^o \qquad (3\text{-}29)$$

$$\vec{H}_T^o = -\frac{\Gamma}{q^2}\nabla_T H_z^o - \frac{j\omega\varepsilon_o}{q^2}\vec{a}_z \times \nabla_T E_z^o \ , \qquad (3\text{-}30)$$

all transverse components of the electric and magnetic fields in the center section of the air-filled region are listed in Appendix B.

The boundary conditions along a radius are that the tangential components of the electric fields are zero at r=b and that the tangential components of the electric and magnetic fields are continuous at r=a. The characteristic equation turns out to be a 6×6 determinant and is given in Appendix B.

### 3-2-2 Matching Fields at the Ends of the Magnetoplasma Column

For a plasma section of finite length, one is confronted with the problem of matching fields at the ends of the plasma column. This step must be taken in order to derive matrix reflection and transmission coefficients at the ends of plasma column. The over-all attenuation due to the finite section of the annular plasma column is then calculated from the transmission coefficient of the dominant mode at the end of the plasma column as given later in Eq.(3-43).

The problem of matching fields at the ends of the plasma column is quite complicated for the following two reasons. First, since a single incident mode can excite a number of gyromagnetic modes in the plasma section and these, in turn, excite a number of TE and TM modes in the empty waveguide, these higher modes must be included in applying the boundary conditions. Second, since the gyromagnetic modes of the plasma section do not form orthogonal sets due to the existence of loss in the plasma [Clarricoats, 1970], the point matching method is introduced to compute the reflection and transmission coefficients at the ends of the plasma column.

Considering the configuration shown in Fig. [3-2], the continuity of the tangential electric and magnetic fields at z=0 gives

$$[A_o^{(0)}][E_t^{T(0)}] + [B_o^{(0)}][E_t^{R(0)}] = [A_o^{(1)}][E_t^{T(1)}] + [B_o^{(1)}][E_t^{R(1)}] \quad , \tag{3-31}$$

and

$$[A_o^{(0)}][H_t^{T(0)}] + [B_o^{(0)}][H_t^{R(0)}] = [A_o^{(1)}][H_t^{T(1)}] + [B_o^{(1)}][H_t^{R(1)}] \quad . \tag{3-32}$$

Similarly the continuity of tangential electric and magnetic fields at z=ℓ leads to

$$[A_\ell^{(0)}][E_t^{T(0)}] + [B_\ell^{(0)}][E_t^{R(0)}] = [A_\ell^{(1)}][E_t^{T(1)}] + [B_\ell^{(1)}][E_t^{R(1)}] \quad , \tag{3-33}$$

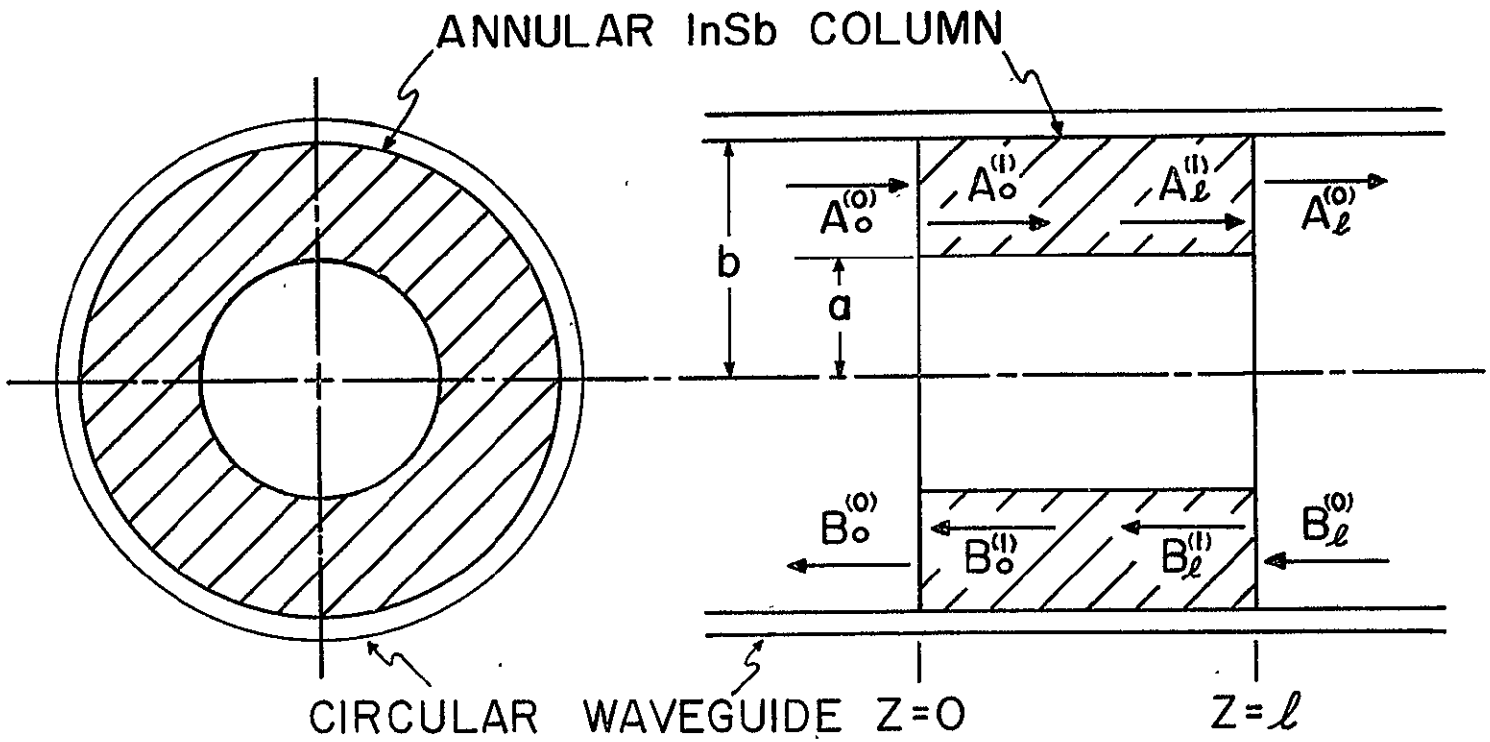


Fig. 3-2. Inside Profile of Hollow InSb Waveguide Isolator.

and

$$[A_{\ell}^{(0)}][H_t^{T(0)}] + [B_{\ell}^{(0)}][H_t^{R(0)}] = [A_{\ell}^{(1)}][H_t^{T(1)}]$$

$$+ [B_{\ell}^{(1)}][H_t^{R(1)}] \ . \qquad (3\text{-}34)$$

Here [E] and [H] are column matrices of electric and magnetic fields, and the superscripts T and R indicate transmitted and reflected em waves, respectively. The index of superscript (0) indicates the field in the empty waveguide and (1) indicates the field in the plasma section. The subscript t of E and H stands for the transverse component of em waves. [A] and [B] are the row matrices of the amplitude coefficients of the transmitted and reflected em fields, respectively. The subscript 0 of A and B indicates the transmission and reflection coefficients at z=0 and the subscript $\ell$ indicates the transmission and reflection coefficients at z=$\ell$. The explicit forms of the transverse components of the em fields in the magnetoplasma section and in the empty waveguides are given in Appendix C.

For the case when a single dominant mode is incident at z=0 and no reflections take place at z=$\infty$,

$$[A_o^{(0)}] = (1,0,\ldots,0) \ , \qquad (3\text{-}35)$$

and

$$[B_{\ell}^{(0)}] = (0,0,\ldots,0) \ . \qquad (3\text{-}36)$$

The row matrices of other reflection and transmission coefficients are given by

$$[A_{\ell}^{(0)}] = (T_{1t}^{(h,0)} \ldots T_{nt}^{(h,0)}, T_{1t}^{(e,0)} \ldots T_{mt}^{(e,0)}) , \qquad (3\text{-}37)$$

$$[B_{o}^{(0)}] = (R_{1t}^{(h,0)} \ldots R_{nt}^{(h,0)}, R_{1t}^{(e,0)} \ldots R_{mt}^{(e,0)}) , \qquad (3\text{-}38)$$

$$[A_{o}^{(1)}] = (T_{1t}^{(1)} \ldots\ldots\ldots\ldots\ldots\ldots T_{n+m,t}^{(1)}) , \qquad (3\text{-}39)$$

$$[A_{\ell}^{(1)}] = (T_{1t}^{(1)} e^{-\Gamma_1 \ell} \ldots\ldots\ldots T_{n+m,t}^{(1)} e^{-\Gamma_{n+m} \ell}) , \qquad (3\text{-}40)$$

$$[B_{o}^{(1)}] = (R_{1t}^{(1)} \ldots\ldots\ldots\ldots\ldots\ldots R_{n+m,t}^{(1)}) , \qquad (3\text{-}41)$$

$$[B_{\ell}^{(1)}] = (R_{1t}^{(1)} e^{+\Gamma_1 \ell} \ldots\ldots\ldots R_{n+m,t}^{(1)} e^{+\Gamma_{n+m} \ell}) . \qquad (3\text{-}42)$$

Here T and R indicate the transmission and the reflection coefficients. The superscripts (h,0) and (e,0) indicate the TE mode and the TM mode in the empty waveguide, respectively, and (1) indicates the gyromagnetic mode in the magnetoplasma section. The subscripts 1....m,n indicate mode numbers, and t stands for the transverse component of em waves. $\Gamma_m$ is the propagation constant of the $m^{th}$ mode in the magnetoplasma section.

These reflection and transmission coefficients are evaluated by numerical techniques using the point matching method. The boundary conditions are imposed at only a finite number of points along the contour of the cross section. This formulation becomes increasingly exact by increasing the number of modes considered and

the number of points chosen.

The over-all attenuation due to the finite section of the annular plasma column is finally given by

$$\text{Loss} = -20 \log T_{lt}^{(h,0)} \text{ db} \tag{3-43}$$

# Chapter 4

## EXPERIMENTAL PROCEDURE

This chapter presents the experimental apparatus and procedures in the experimental investigations for the circular waveguide containing the annular plasma column in a longitudinal dc magnetic field. The characteristics of the semiconductor used as a plasma medium will be established. Discussions are extended to the sample preparations and the experimental procedure in observing the non-reciprocal phenomena in the plasma waveguide.

### 4-1 Properties of Solid State Plasma

The material chosen for the solid state plasma is n-type InSb, which has a high mobility of free carriers and a relatively low carrier concentration. The average value of the effective mass for n-type InSb at 77°K from infrared Faraday effect measurements was $m^*=0.0143m_o$ [Hogarth, 1965]. From the Faraday rotation experiments on n-type InSb at 77°K performed in this laboratory by B.R. McLeod [1968], the static relative dielectric constant was found to be 16.0. The mobility of the free carriers and the carrier concentration are determined by performing either Hall measurements or van der Pauw measurements [van der Pauw, 1958]. For

nondegenerate semiconductors and small magnetic fields the Hall coefficient is given by

$$R_H = \frac{r_R}{e} \frac{P-b^2n}{(P+bn)^2} \quad , \tag{4-1}$$

where

$$b = \frac{\mu_n}{\mu_p} \quad .$$

For n>>p, the Hall coefficient reduces to

$$R_H = -\frac{r_R}{ne} \quad . \tag{4-2}$$

The factor $r_R$ is determined by the scattering mechanism [Smith, 1964]. When acoustic scattering is dominant, $r_R$=1.18. If ionized impurity scattering dominates, $r_R$=1.93. However, the scattering of conduction electrons by both impurity ions and the lattice are dominant at 77°K in n-type InSb. V.A. Johnson and W.J. Whitesell [1953], and R.T. Bate, R.K. Willardson and A.C. Beer [1959] have made an extensive theoretical and experimental study of magnetoresistance effects in n-type InSb between 50°K and 200°K, and the value $r_R$ was found to be 1.09. After making this correction, the parameters of n-type InSb used in the experiment were found as listed in Table [4-1].

## 4-2 Experimental Set-up

The devices designed for non-reciprocal phenomena consist of two transitions, two polarizers and the test section shown in Fig. [4-1]. $TE_{10}$ mode propagating in the rectangular waveguide excites a linearly polarized $TE_{11}$ mode in the circular waveguide due to the transition. The polarizers which consist of quarter-wave teflon slabs in the circular waveguide set at 45° with respect to the electric field in the rectangular waveguide convert the linearly polarized $TE_{11}$ mode into the cp $TE_{11}$ mode. The test section contains the annular magnetoplasma column of n-type InSb. These columns of InSb were cut by using an ultra-sonic drill and polished chemically in a cromine and methanol etch. They were supported by styrofoam in the test section. The small opening between the column and the circular waveguide wall was filled with the silver paint.

The devices were placed in a longitudinal dc magnetic field using a 6-inch Varian magnet with a 2-inch gap. A styrofoam Dewar surrounding the semiconductor was filled with the liquid nitrogen. The microwave system was composed of a klystron, an isolator, a variable attenuator and a crystal detector. The klystron provided a 94 GHz signal modulated at 1 kc/s. A lock-in amplifier was used to take the data.

A block diagram of the experimental set-up is shown in Fig. [4-2].

TABLE 4-1

Electrical Properties of n-type InSb Crystal

| | 75°K |
|---|---|
| Electron Effective Mass | $0.0143m_o$ |
| Dielectric Constant | 16.0 |
| Electron Mobility | $5.2\times10^5 cm^2/v\cdot sec$ |
| Carrier Density | $2.8\times10^{14}/cm^3$ |

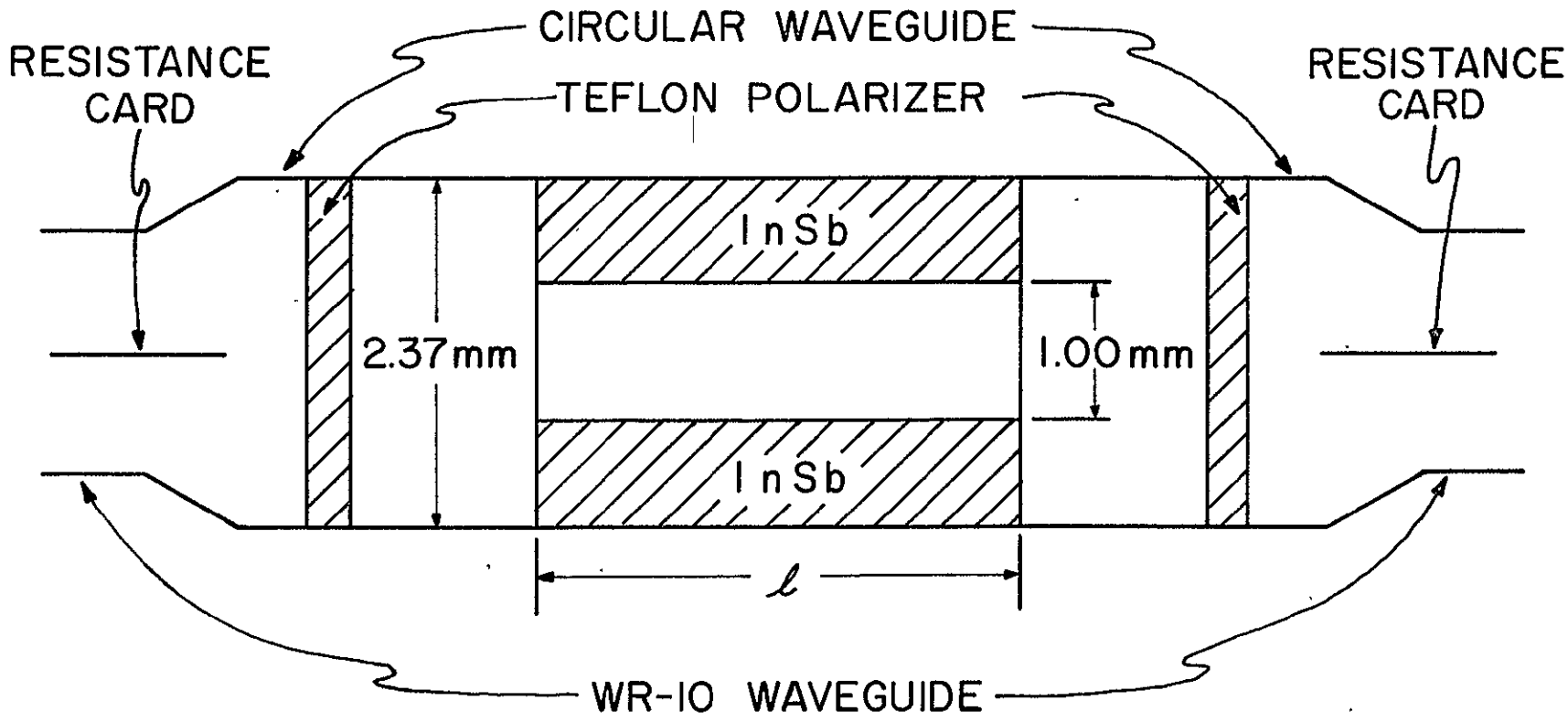


Fig. 4-1. Waveguide Isolator containing Annular Plasma Column.

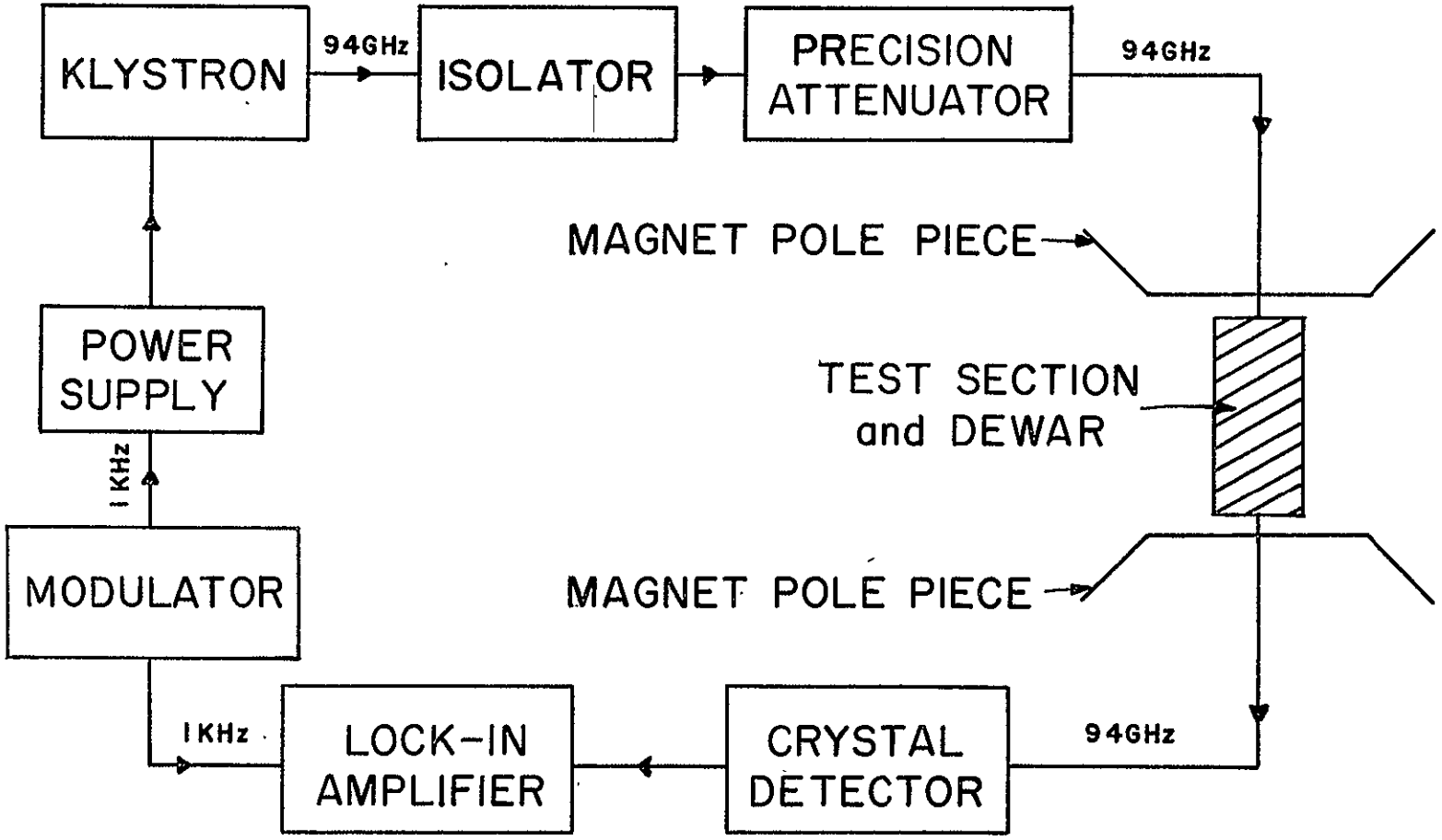


Fig. 4-2. Block Diagram of Experiment Set-up.

# Chapter 5

## DISCUSSION OF EXPERIMENTAL AND THEORETICAL RESULTS

This chapter presents the experimental and theoretical results of propagation characteristics for a circular waveguide containing an annular InSb column in a longitudinal dc magnetic field. The results calculated from the approximate theory of Section 3-1 and from the MMA of Section 3-2 are given. The validity of the assumptions made and the correlation between the experimental and theoretical results are discussed.

### 5-1 Experimental Results

Fig. [5-1], [5-2] and [5-3] show the experimentally determined attenuation for the circular waveguides containing the various lengths $\ell$ of InSb. Only losses within the test section are included. Attenuation could be measured to within ±0.5db and the magnetic field was measured with a gaussmeter to an accuracy of ±100 gauss.

### 5-2 Comparison with the Approximate Theory

The calculated attenuation curves derived from the approximate theory of Section 3-1 are shown in Fig. [5-4]. This figure shows that approximate theory gives a fairly good agreement with the corresponding

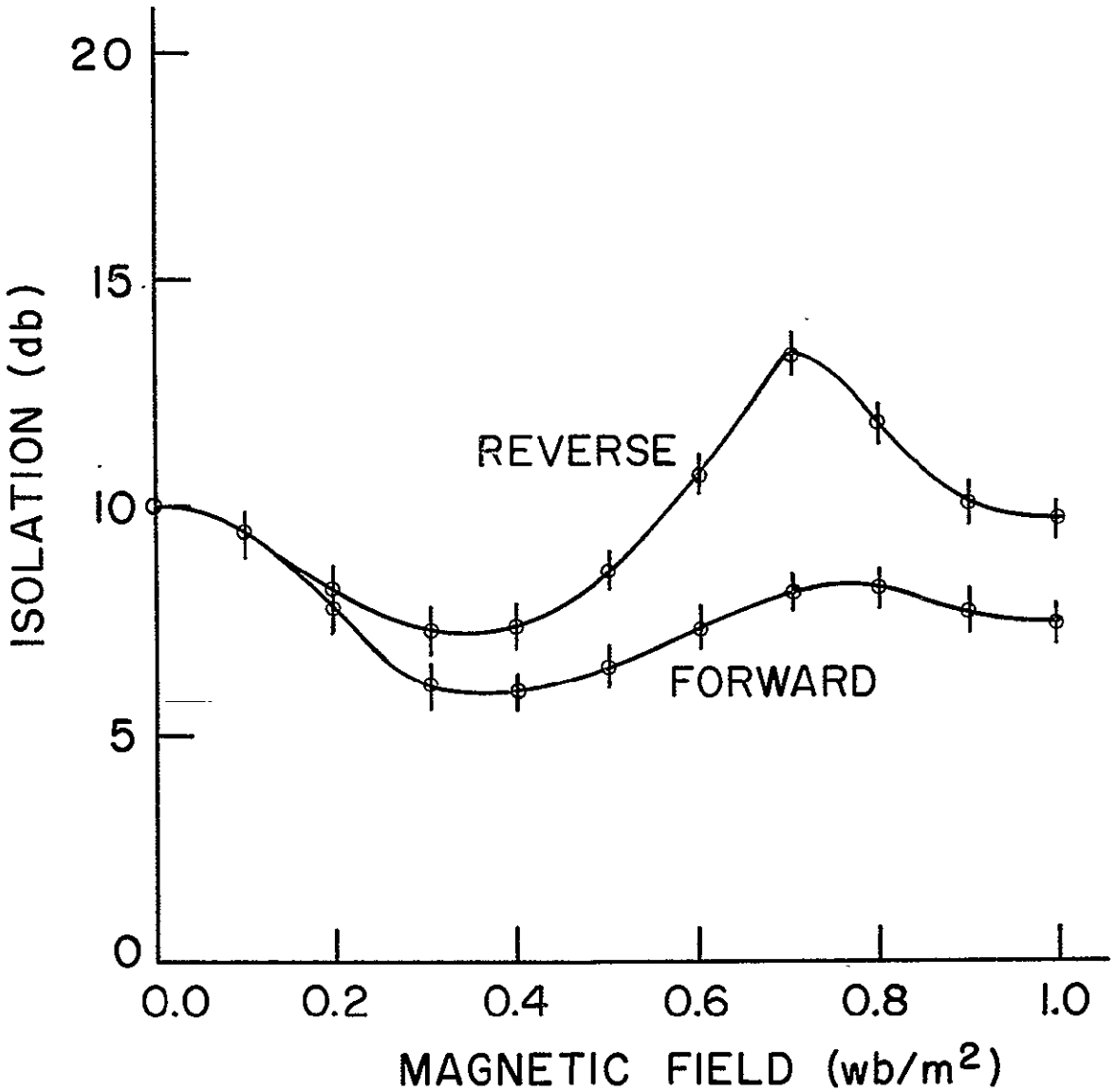


Fig. 5-1. Experimental Results for Hollow InSb Waveguide Isolator [Parameters of InSb are given in Table 4-1. Geometry of 94 GHz Waveguide Isolator is shown in Fig. 4-1 with $\ell$=0.127mm].

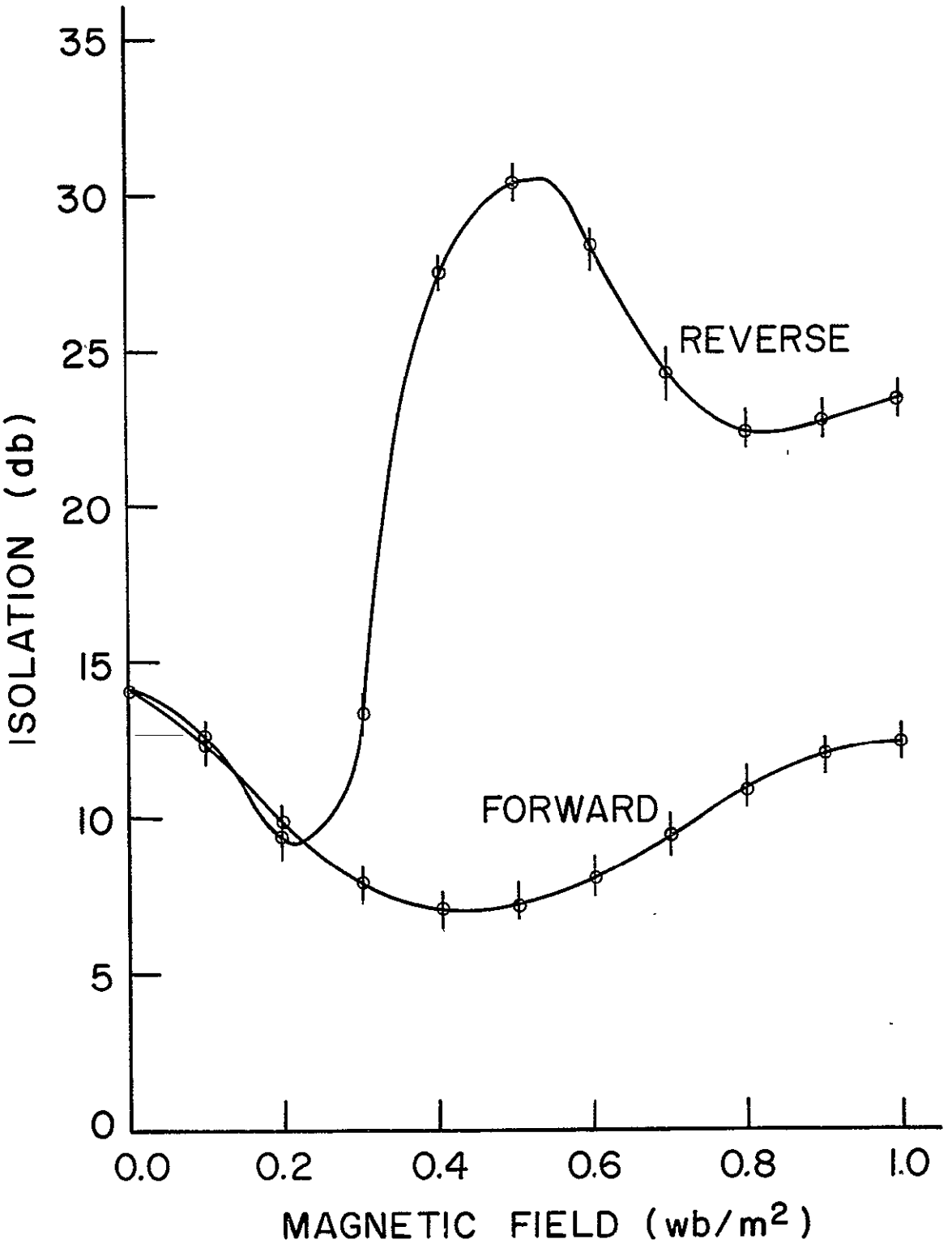


Fig. 5-2. Experimental Results for Hollow InSb Waveguide Isolator [Parameters of InSb are given in Table 4-1. Geometry of 94 GHz Waveguide Isolator is shown in Fig. 4-1 with $\ell$=0.762mm].

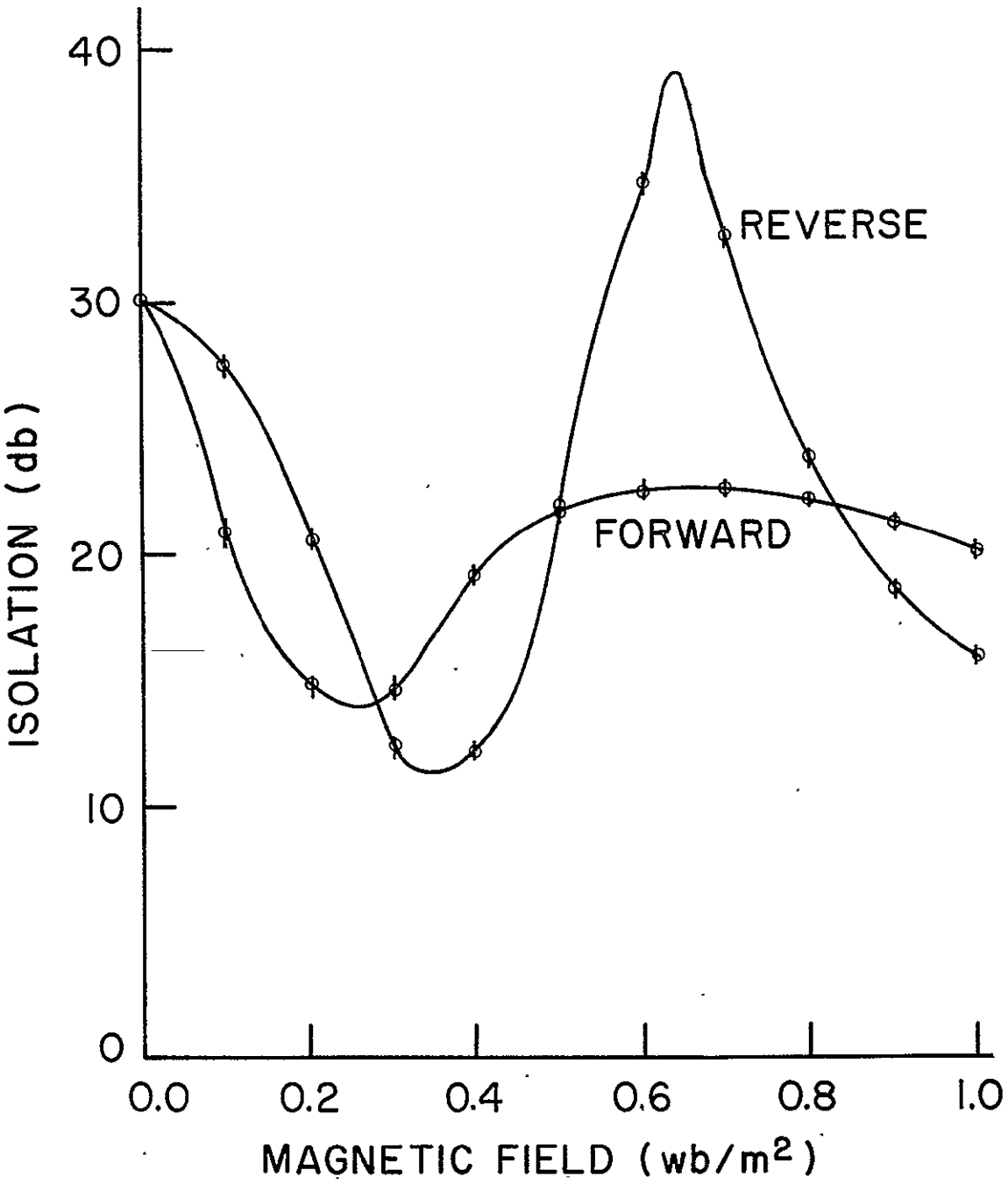


Fig. 5-3. Experimental Results for Hollow InSb Waveguide Isolator [Parameters of InSb are given in Table 4-1. Geometry of 94 GHz Waveguide Isolator is shown in Fig. 4-1 with $\ell$=1.524mm].

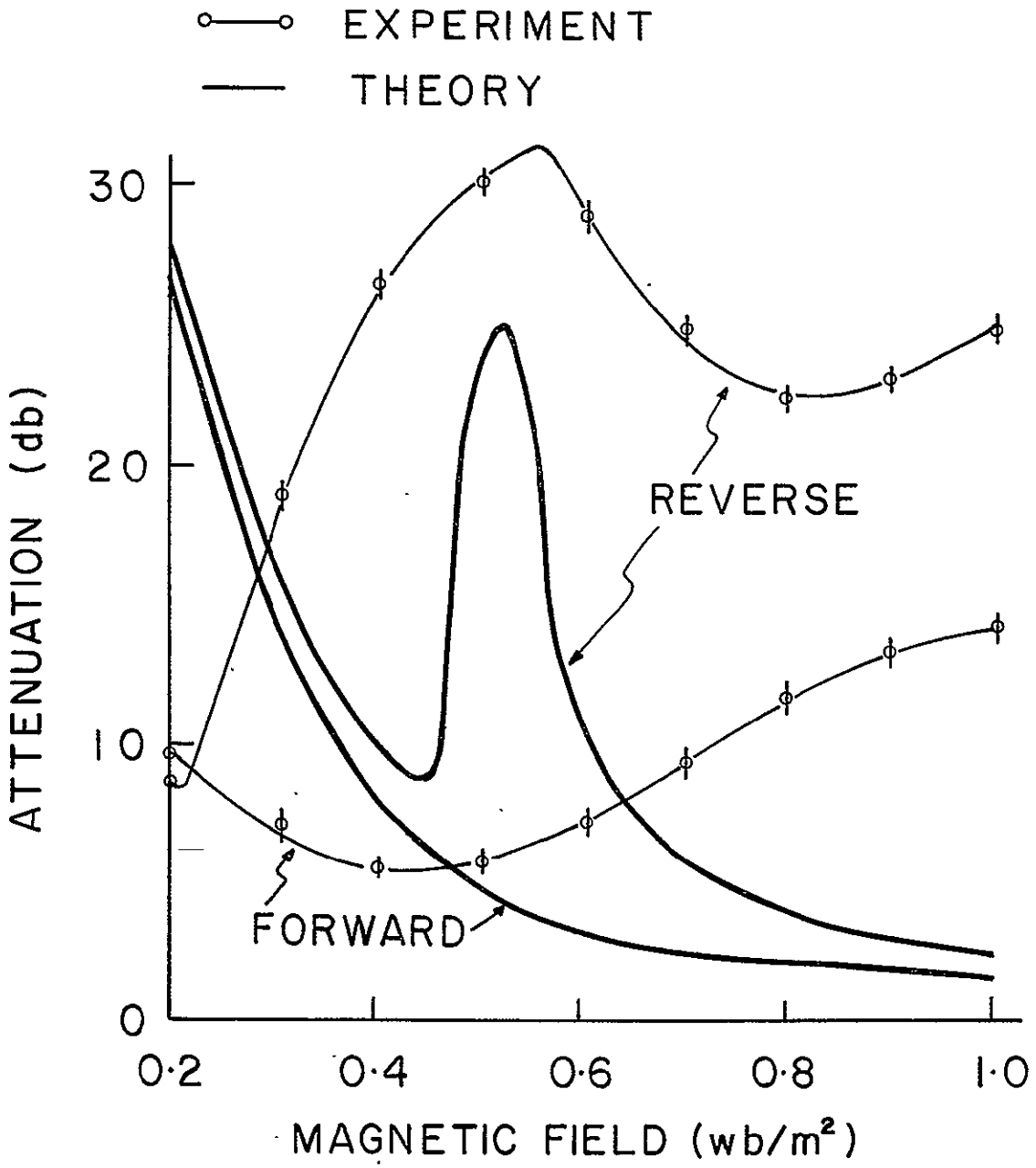


Fig. 5-4. Theoretical Results for Hollow InSb Waveguide Isolator ($\ell$ = 0.762mm) Based on Approximate Theory [Parameters of InSb are given in Table 4-1. Geometry of 94 GHz Waveguide Isolator is shown in Fig. 4-1 with $\ell$=0.762mm].

experimental results for a low longitudinal dc magnetic field up to approximately 6 kG. The assumption of a uniform plane wave propagating in the section of the annular InSb column appears to be quite reasonable and the exclusion or the absorption of em waves is the physical explanation summarized as follows: Since the power density of the right cp wave is very small in the InSb and is heavily concentrated in the air-filled center section, its propagation is virtually independent of the longitudinal dc magnetic field. On the other hand, since the left cp wave is excited strongly within the lossy InSb, the em waves are absorbed and dissipated as heat. For the case of higher longitudinal dc magnetic fields, MMA of the boundary value problem shows that the excitation of higher gyromagnetic modes becomes significant, and some deviation of the electric field from the $TE_{11}$ mode pattern is expected. Thus this causes some trouble in the approximate theory. It is also found that the reflection coefficient for the dominant mode obtained from MMA is relatively small ($<0.5$) at the end of plasma column, and thus it is a reasonable first approximation to neglect the attenuation due to the reflection. But the approximate theory did not account for the transition between the empty waveguide and the guide in which the annular InSb column was mounted, nor did it account for my reflections,

and thus extremely good agreement between theoretical and experimental results was not expected.

## 5-3 Comparison with Mode Matching Analysis

The first step of MMA was to determine the propagation constants of the gyromagnetic modes. Since the characteristic equation is quite complicated, an interative root-finding technique was employed to find the propagation constants. The real and imaginary parts of the propagation constants for both right and left polarizations were obtained by computer and are shown in Fig. [5-5], [5-6]. Three place accuracy was used throughout the calculations.

The resulting propagation constants are utilized to match the boundary conditions at the ends of the plasma column. This second step determines the amplitudes of the reflection and transmission coefficients of the gyromagnetic modes and of the empty waveguide modes. In the present case, four gyromagnetic modes in the section of the annular InSb column and two TE and two TM modes in the empty waveguide are taken into account. Point matching was employed to solve the inhomogeneous linear equations of order 16. The overall attenuation due to the various lengths of the InSb columns was evaluated from the transmission coefficients of $TE_{11}$ circular mode at the end of the column and is

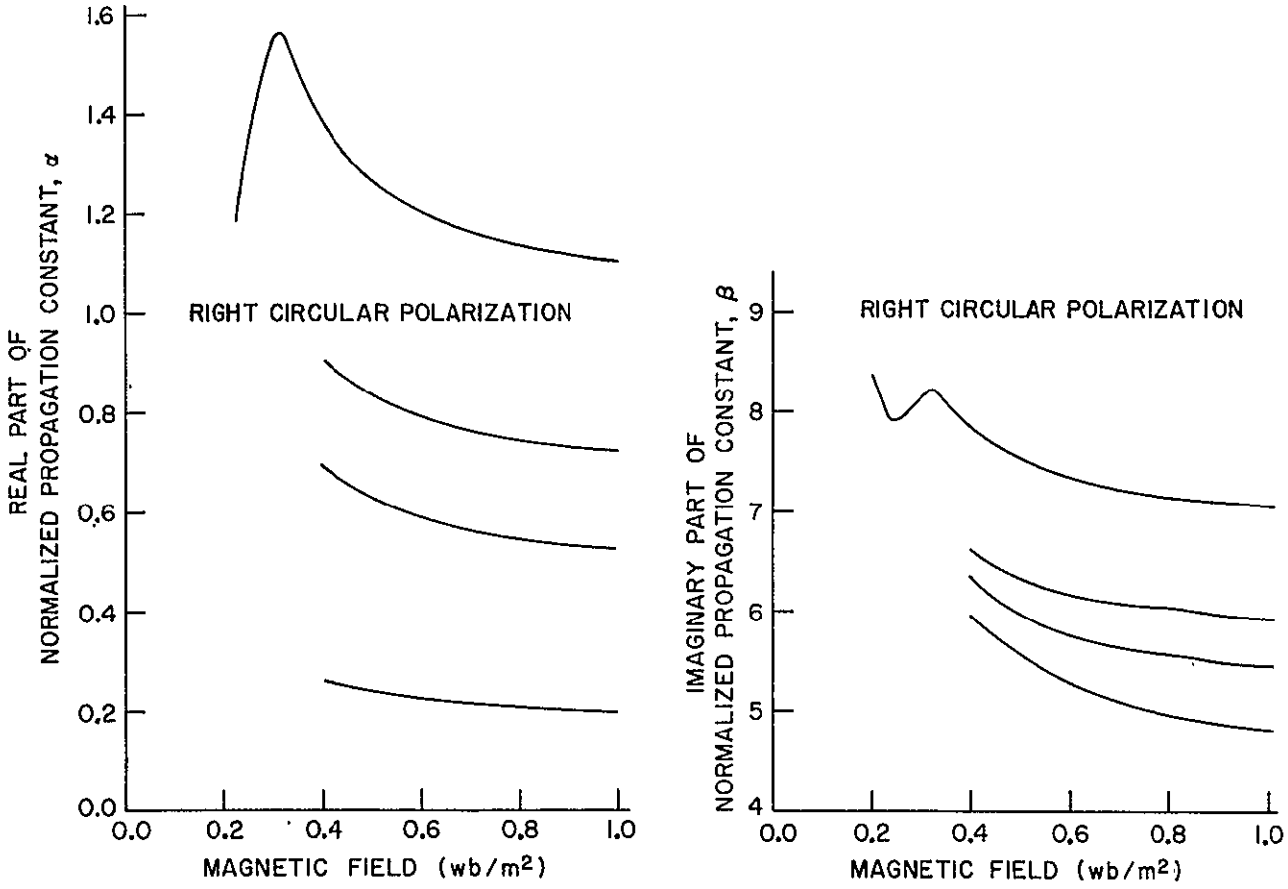


Fig. 5-5. Normalized Propagation Constant for Right Circularly Polarized Wave as a Function of Magnetic Field [Parameters of InSb are given in Table 4-1. Geometry of 94 GHz Waveguide Isolator is shown in Fig. 4-1].

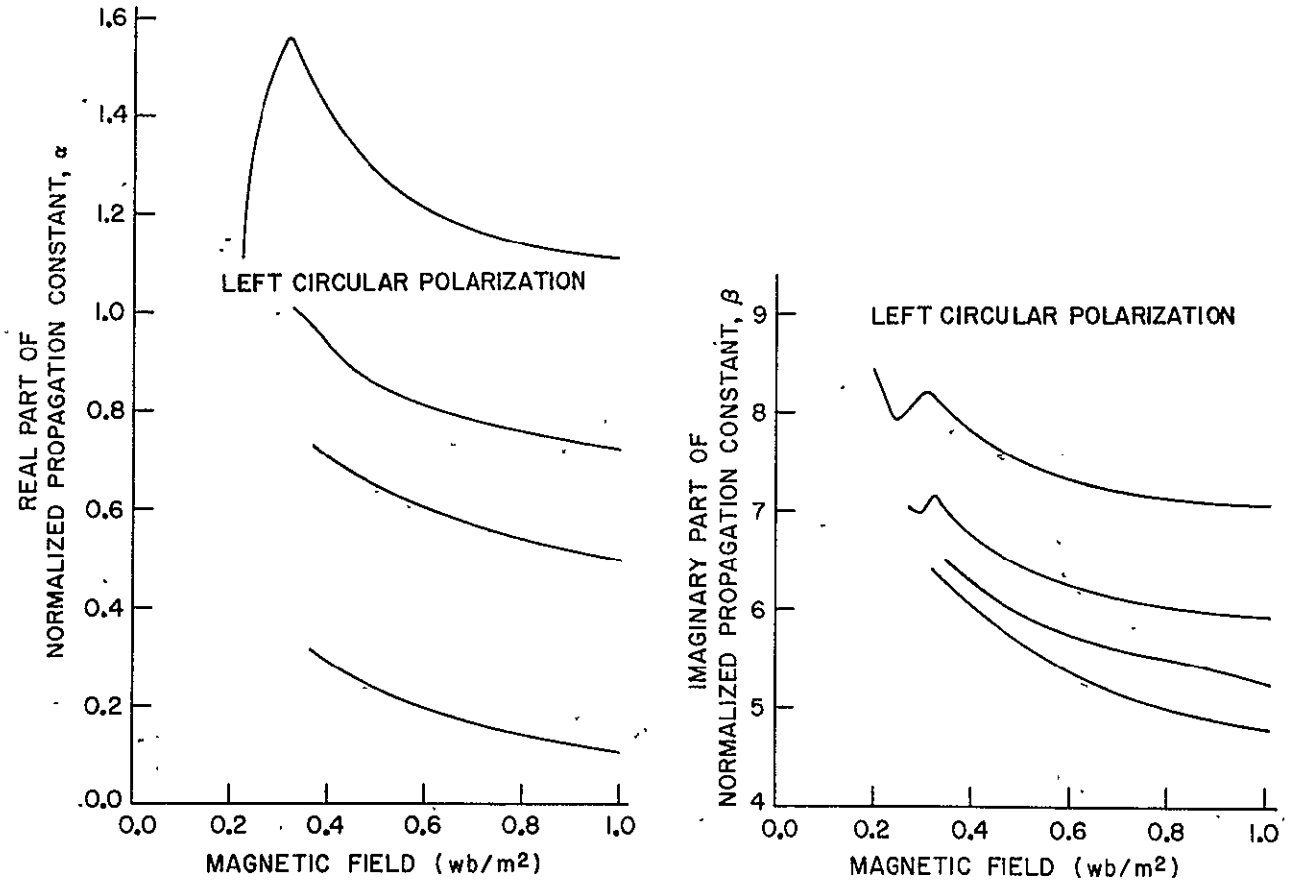


Fig. 5-6. Normalized Propagation Constant for Left Circularly Polarized Wave as a Function of Magnetic Field [Parameters of InSb are given in Table 4-1. Geometry of 94 GHz Waveguide Isolator is shown in Fig. 4-1].

shown in Fig. [5-7], [5-8] and [5-9]. The general agreements between the experimental and the theoretical results are quite good. The boundary conditions are imposed at only four points at the ends of the plasma column by taking into account only four gyromagnetic modes in the magnetoplasma section and four higher excited modes in the empty waveguide section. It is, however, expected that, although the inclusion of higher excited modes as well as the dominant modes is essential in a rigorous treatment of the boundary conditions at the ends of the plasma column, the convergence is fairly rapid [Champlin, et al., 1969]. Thus small discrepancy between theoretical and experimental results appears to be mainly due to experimental error as discussed as follows. The annular InSb column was cut by using an ultra-sonic drill. Although the resulting InSb column was close to an annular cross section, there was some departure from the circular symmetry required for a circularly polarized wave, and this caused some trouble in the experiments. The results of the van der Pauw measurements showed variations by as much as 10% existed in the crystal properties. This inhomogeneity would also explain some of the discrepancy between theoretical and experimental results.

The reflection coefficients of the incident $TE_{11}$ mode at the ends of the plasma column show that the

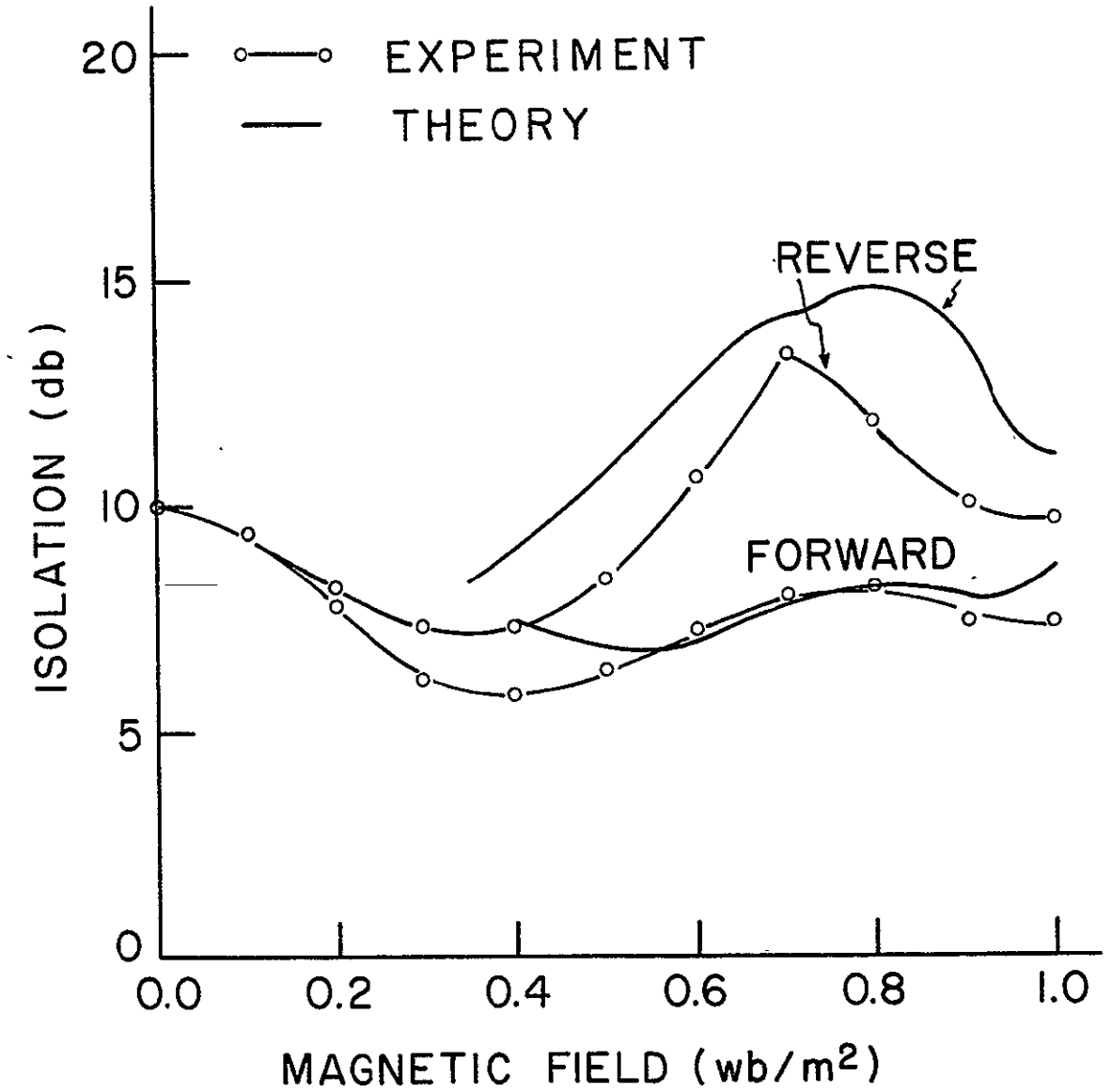


Fig. 5-7. Theoretical Results for Hollow InSb Waveguide Isolator [Parameters of InSb are given in Table 4-1. Geometry of 94 GHz InSb Waveguide Isolator is shown in Fig. 4-1 with $\ell$=0.127mm].

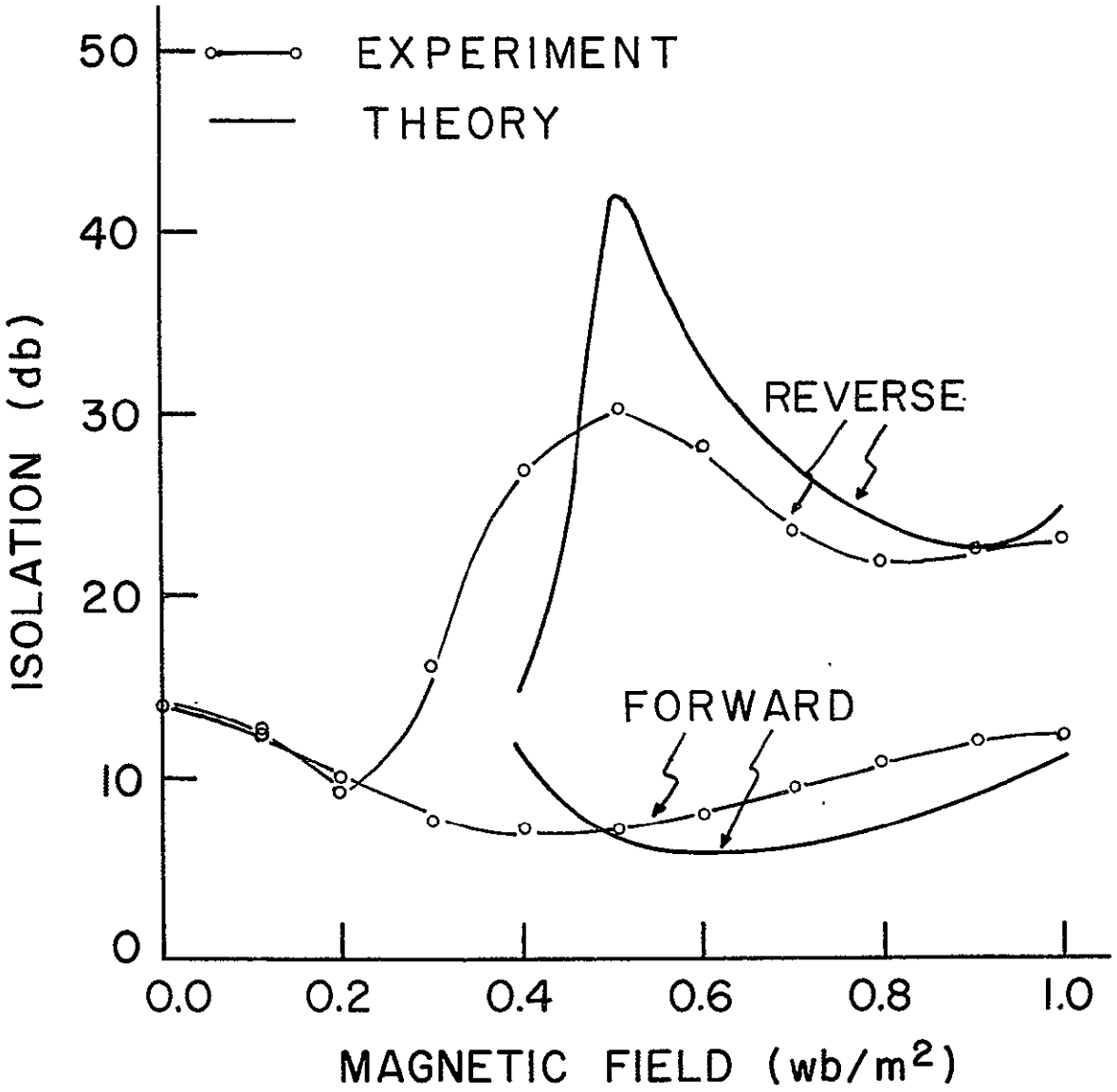


Fig. 5-8. Theoretical Results for Hollow InSb Waveguide Isolator [parameters of InSb are given in Table 4-1. Geometry of 94 GHz InSb Waveguide Isolator is shown in Fig. 4-1 with $\ell$=0.762mm].

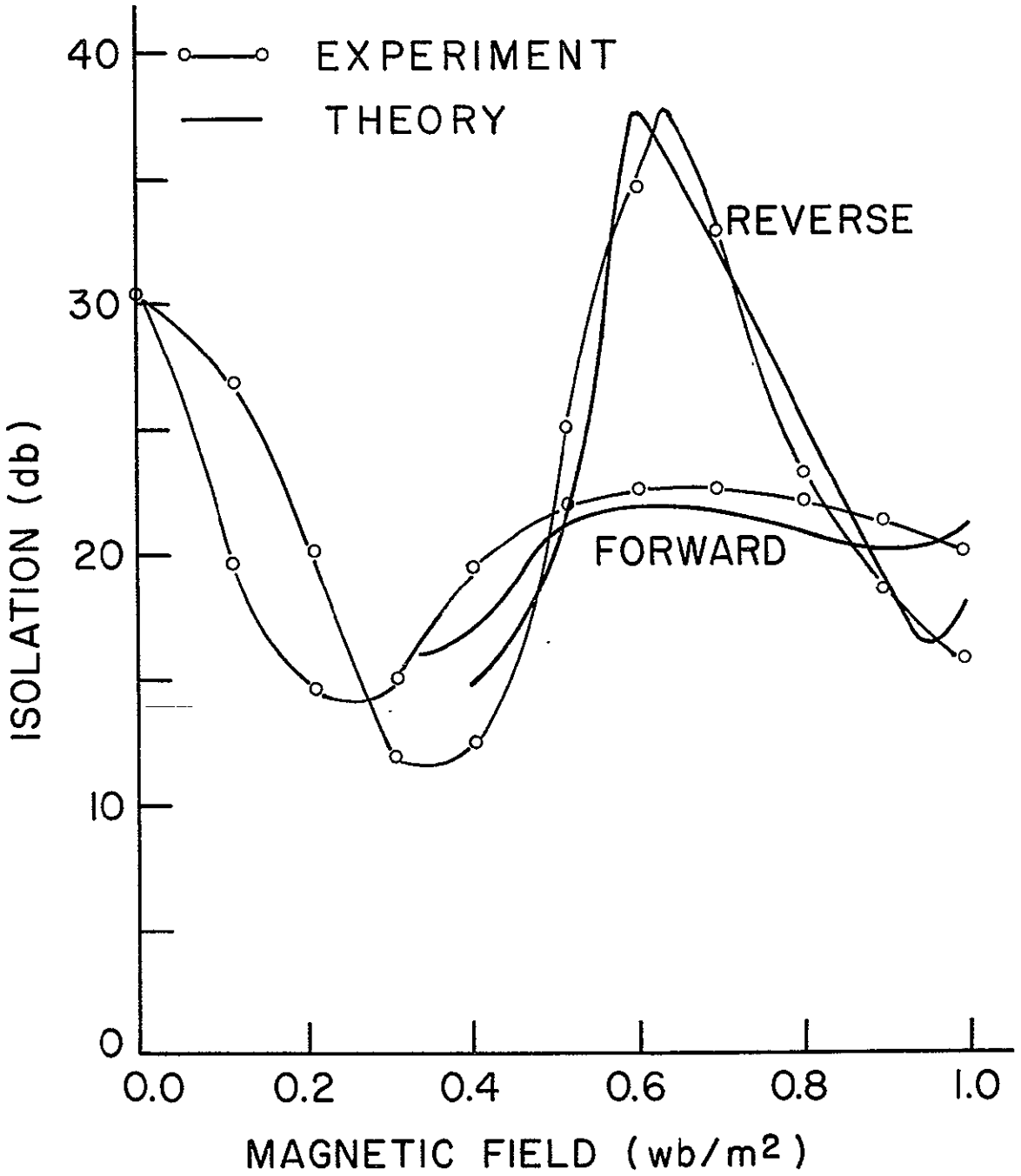


Fig. 5-9. Theoretical Results for Hollow InSb Waveguide Isolator [Parameters of InSb are given in Table 4-1. Geometry of 94 GHz InSb Waveguide Isolator is shown in Fig. 4-1 with $\ell$=1.524mm].

devices are absorbing the microwave power to achieve the attenuation obtained experimentally. A small amount of the reflected wave is linearly polarized in a horizontal plane, and thus is absorbed by the resistance card placed behind the polarizer. Of course, it could be possible to prevent this reflection by a careful design of customary matching transformers such as a conical taper or an end cap of dielectric material whose dielectric constant is chosen so as to provide an impedance match at the ends of plasma column.

## Chapter 6

## SUMMARY AND CONCLUSIONS OF PART I

Theoretical and experimental investigations were performed for the purpose of the utilization of nonreciprocal behavior in the solid state magnetoplasma for the development of millimeter waveguide isolators. The geometry employed consists of a circular waveguide with a coaxial annular column of a semiconductor plasma in a longitudinal dc magnetic field.

The basic operation of this type of isolators is due to exclusion or absorption of em waves in a magnetoplasma. The microwave signal for the right cp wave is excluded from the magnetoplasma, and thus the signal can be only slightly absorbed. The microwave signal for the left cp wave, however, penetrates into the lossy magnetoplasma and is strongly absorbed. The approximate theory is based on this physical reasoning. A mode matching analysis is based on the solutions of the boundary value problem. The propagation constants of the gyromagnetic modes were determined in the section of a circular waveguide with an annular column of magnetoplasma. For the case of a waveguide with finite length of an annular plasma column, the boundary conditions were satisfied at the ends of plasma column by taking into account the higher excited modes as well as the

dominant mode. The reflection and transmission coefficients were determined at the ends of the plasma column by using the point-matching method.

The experiments were performed at 94 GHz. In order to obtain characteristics useful for an isolator, i.e. low forward loss and high reverse loss, the InSb isolator was operated at 75°K. In those systems in which cooling is already present such as in maser systems, this is not a serious problem. The experiments demonstrated 23 db isolation with 7 db forward loss for one waveguide isolator and corresponding theoretical data calculated from a mode matching analysis were 36 db isolation with 5 db forward loss. This discrepancy between theoretical and experimental results mainly results from the incomplete theoretical analysis. It is assumed in the approximate theory that the field both in the center section of air-filled region and in the annular column are of $TE_{11}$ mode pattern, and the amplitudes of the electric fields are determined by the dielectric constant of each section. However, it is found from a mode matching analysis that some deviation of electric field from the $TE_{11}$ mode pattern in these regions takes place, and this causes some trouble in the approximate theory. In the mode matching analysis the point matching method was adopted to solve the boundary problem. The boundary conditions are imposed

at only four points at the ends of plasma column by taking into account four gyromagnetic modes in the magnetoplasma section as well as four excited higher modes in the empty waveguide region. It is possible, of course, to correct these by increasing the number of modes considered and the number of points chosen.

The hollow InSb waveguide isolator can be operated with a wider band width, since the maximum attenuation was insensitive to the dc magnetic fields (see Fig. [5-1], [5-2] and [5-3]) and hence to the operating frequencies. It is speculated that the lower forward loss could be obtained in an annular InSb column with a larger diameter hole but with expense of isolation.

Although the requirement of cooling may limit the applications for millimeter wavelength devices, the solid state magnetoplasma finds important applications for the development of the non-reciprocal devices in the submillimeter wave region.

# PART II

# NON-RECIPROCAL REFLECTION BEAM ISOLATOR FOR USE AT MILLIMETER AND SUBMILLIMETER WAVELENGTHS

The purpose of Part II is to discuss the non-reciprocal reflection from solid state magnetoplasmas for the development of the reflection beam isolator for use at millimeter and submillimeter wavelengths. Chapter 7 presents the theoretical deviation of reflection coefficients from a plasma medium. In Chapter 8 the experimental apparatus and procedures used to measure the reflection coefficients from the plasma interfaces are given. The properties of the semiconductors used as plasma media are also given. The brief discussion on the design and construction of HCN laser used as a far-infrared source for the experiments and on the IR detectors are also given. Chapter 9 presents the theoretical and experimental results. The results for the reflection from the interface between a dielectric medium and GaAs at 94 GHz, and from the interface between free space and dielectric coated InSb at the wavelength of 337 μm are presented. In Chapter 10 physical explanation of the non-reciprocal reflections is presented. Possible refinements for the applications

of the devices and comparison with other devices are also brought out.

# Chapter 7

## THEORETICAL DERIVATION OF REFLECTION COEFFICIENTS

Many studies have been made on the nature of the reflection from the ionosphere. N.F. Barber and D.D. Crombie [1959] have calculated the reflection coefficient from a sharply bounded ionosphere in the presence of a horizontal magnetic field perpendicular to the plane of incidence and found that the reflection coefficient for em waves in the ionosphere incident from the west is numerically greater than that for the wave incident from the east. Non-reciprocal reflection of em waves incident on a solid state magnetoplasma at 94 GHz was studied by J.M. Seaman [1968].

This chapter outlines the theoretical analysis of the reflection coefficient of a wave incident on a magnetoplasma, which depends on the orientation of the dc magnetic field and the direction of propagation. We consider only the case in which the plane of polarization of em waves is in the plane of incidence, and the direction of propagation is perpendicular to a dc magnetic field which is parallel to the surface of the magnetoplasma (Kerr transverse magneto-optical effect).

Three configurations are considered with the goal of achieving best isolation with low insertion loss. These are the reflections of a plane wave from the

interfaces between free space and a magnetoplasma, between a dielectric medium and a magnetoplasma, and between free space and a dielectric coated magnetoplasma, as shown in Fig. [7-1].

Define Cartesian coordinates where a dc magnetic field is applied in the z-direction. For a plane wave with harmonic time dependence, $\exp(j\omega t)$, Maxwell's equations are given by

$$-j\omega\mu_o\vec{H} = \nabla\times\vec{E} \quad , \tag{7-1}$$

$$j\omega\varepsilon_o\vec{E} = \bar{\bar{K}}^{-1}\nabla\times\vec{H} \quad . \tag{7-2}$$

$\bar{\bar{K}}^{-1}$ is the inverse of the relative dielectric tensor of a plasma and is given in the following form:

$$\bar{\bar{K}}^{-1} = \begin{vmatrix} A & -D & 0 \\ D & A & 0 \\ 0 & 0 & B \end{vmatrix} \tag{7-3}$$

where

$$A = \frac{K_\perp}{K_\perp^2 + K_x^2} \tag{7-4}$$

$$B = \frac{1}{K_{||}}$$

and

$$D = -\frac{K_x}{K_\perp^2 + K_x^2}$$

The definitions of symbols $K_\perp$, $K_x$ and $K_{||}$ are given in Section 2-1.

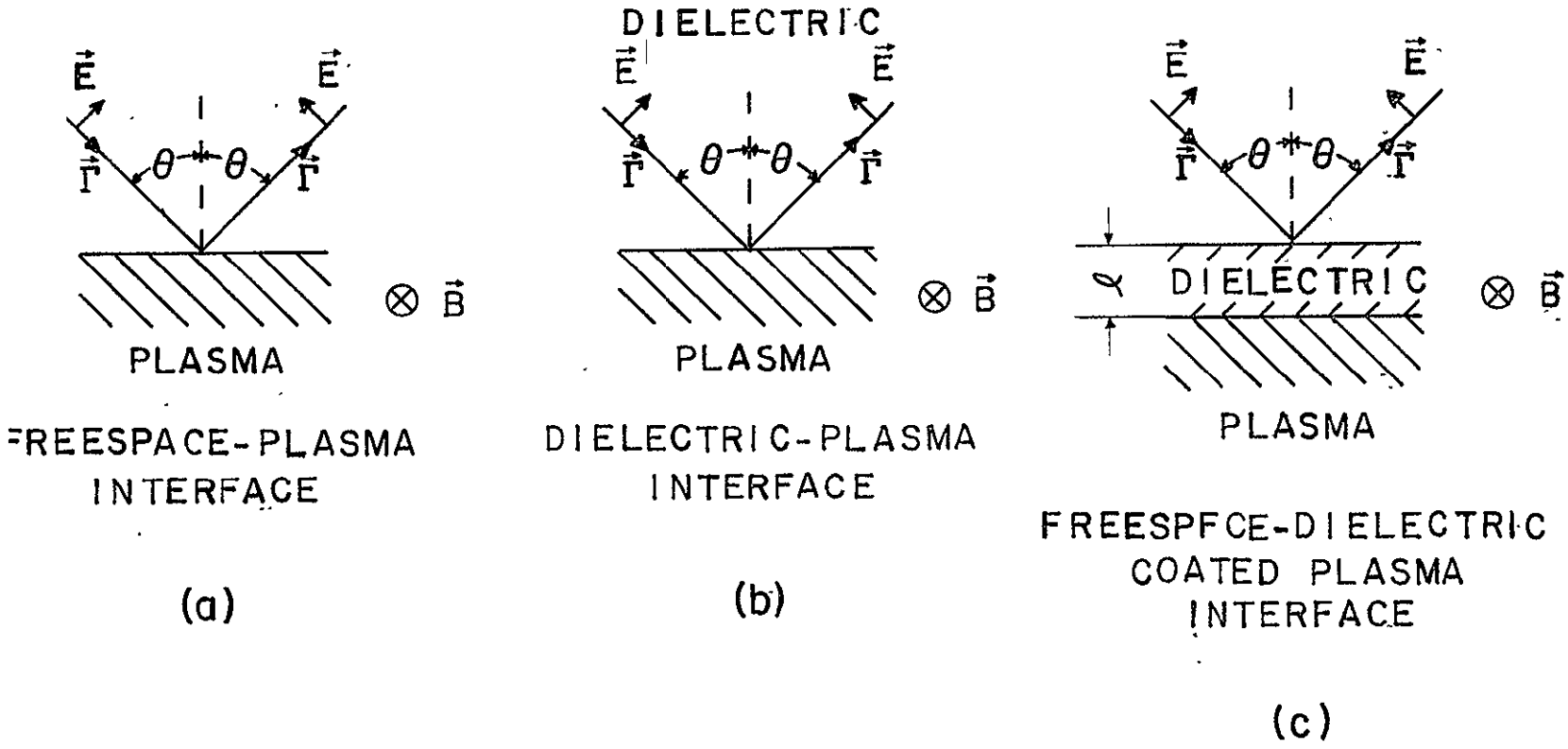


Fig. 7-1. Reflections from Interfaces

## 7-1 Reflection from Air-Plasma Interface

The reflection coefficient R for a plane boundary between free space and a plasma medium (see Fig. [7-1a]) has been calculated [Wait, 1962] and is given by

$$R = \frac{\cos\theta - \Delta}{\cos\theta + \Delta} \quad , \tag{7-5}$$

where

$$\Delta = A\cdot\left(\frac{1}{A} - \sin^2\theta\right)^{\frac{1}{2}} + D\cdot\sin\theta \tag{7-6}$$

## 7-2 Reflection from Dielectric-Plasma Interface

The calculation is extended below to include the effects of a dielectric medium placed on the plasma as shown in Fig.[7-1b], and the reflection coefficient $R_M$ from the interface between a dielectric medium and a plasma medium is given by

$$R_M = \frac{\cos\theta - \Delta_M}{\cos\theta + \Delta_M} \quad , \tag{7-7}$$

where

$$\Delta_M = K_M\left[A\cdot\left(\frac{1}{K_M A} - \sin^2\theta\right)^{\frac{1}{2}} + D\cdot\sin\theta\right] \quad , \tag{7-8}$$

and $K_M$ is a relative dielectric constant of a dielectric medium.

## 7-3 Reflection from Air-Dielectric Coated Plasma Interface

In this section the reflection coefficients from the interface between free space and a dielectric coated magnetoplasma are derived by both the field matching method and the impedance method.

### 7-3-1 Field Matching Method

Generally the magnitude of all field components of em waves reflected from a multiple layer interface can be evaluated by matching the tangential components of the field at each plane interface.

Considering the configuration as shown in Fig. [7-2], where the electric field is polarized in the plane of incidence and the fields do not vary in the z direction, we are required to solve a $4^{th}$ order inhomogeneous linear equation in order to satisfy the boundary conditions. Although it is quite tedious to solve the inhomogeneous linear equation, the method is especially useful to evaluate magnitudes of all components of em waves inside a plasma medium. These components are used in Chapter 10 to calculate the ellipticity of the electric field and the orbit of electrons in the magnetoplasma in order to study the physics behind the non-reciprocal reflection.

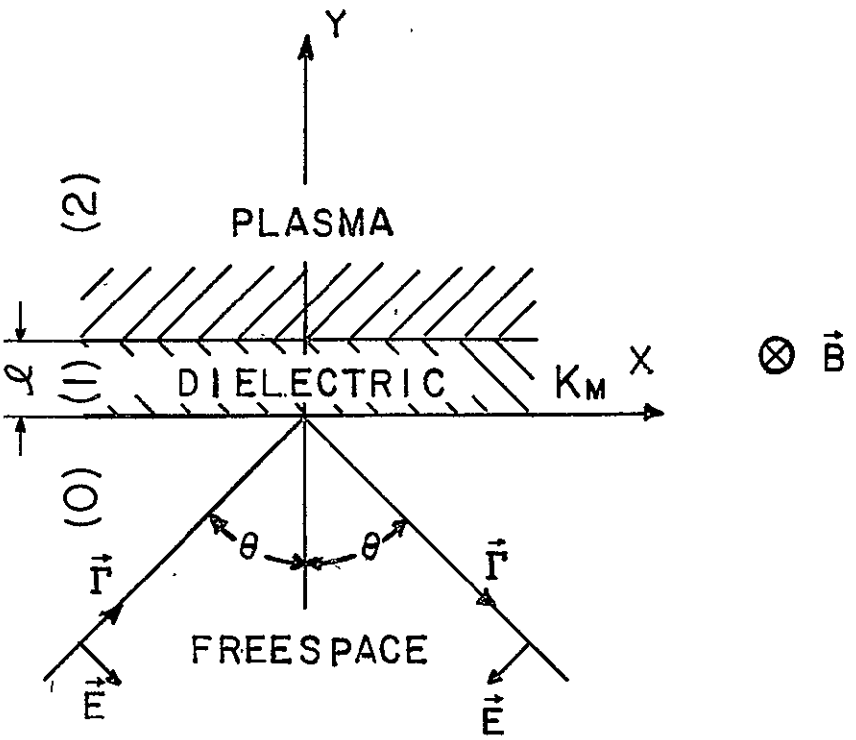


Fig. 7-2. Orientations of Field Vector $\vec{E}$, Propagation Vector $\vec{\Gamma}$ and dc Magnetic Field $\vec{B}$.

The boundary conditions are that the tangential components of the fields are to be continuous at y=0, ℓ in Fig. [7-2].

At y=0,

$$1\cdot {}_oH_z{}^t(x,0) + R_o\cdot {}_oH_z^r(x,0) = T_1\cdot {}_1H_z^t(x,0) + R_1\cdot {}_1H_z^r(x,0) \tag{7-9}$$

$$1\cdot {}_oE_x{}^t(x,0) + R_o\cdot {}_oE_x^r(x,0) = T_1\cdot {}_1E_x{}^t(x,0) + R_1\cdot {}_1E_x{}^r(x,0). \tag{7-10}$$

At y=ℓ,

$$T_1\cdot {}_1H_z{}^t(x,\ell) + R_1\cdot {}_1H_z{}^r(x,\ell) = T_2\cdot {}_2H_z{}^t(x,\ell)\ , \tag{7-11}$$

$$T_1\cdot {}_1E_x{}^t(x,\ell) + R_1\cdot {}_1E_x{}^r(x,\ell) = T_2\cdot {}_2E_x{}^t(x,\ell)\ . \tag{7-12}$$

Here E and H indicate the electric and magnetic fields, and the corresponding superscripts t and r stand for transmitted and reflected em waves. The right subscripts x and z indicate the x and z components of fields, and the left subscripts 0, 1 and 2 indicate the fields in free space, in the dielectric and in the magnetoplasma. T and R indicate the transmission and reflection coefficients, and the corresponding subscripts 0, 1 and 2 indicate amplitude coefficients in free space, in the dielectric and in the plasma. The detailed calculations of all field components in free space, in a dielectric, and in a magnetoplasma are given in the

standard textbooks [Collins, 1960; Stratton, 1941].

The reflection coefficient $R_o$ from the interface between free space and a dielectric coated magnetoplasma, and the amplitude of the field components in the magnetoplasma, ${}_2H_z^t$, ${}_2E_x^t$ and ${}_2E_y^t$, are obtained by solving the $4^{th}$ order inhomogeneous linear equation as given in Eq.(7-9) to (7-12).

### 7.3.2 Impedance Method

The wave impedance G for the transmitted wave is defined by

$$G^t = -\frac{E_x^t}{H_z^t} \tag{7-13}$$

and for the reflected wave,

$$G^r = \frac{E_x^r}{H_z^r} \quad , \tag{7-14}$$

where superscripts t and r indicate the wave impedances for transmitted and reflected waves, respectively. The wave impedances G's for each layer shown in Fig. [7-2] are as follows: In free space (0):

$$G_o^t = G_o^r = Z_o \cos\theta \quad . \tag{7-15}$$

In a dielectric medium (1):

$$G_1^t = G_1^r = \frac{Z_o}{K_M}\left(K_M - \sin^2\theta\right)^{\frac{1}{2}} \quad , \tag{7-16}$$

where $K_M$ is the relative dielectric constant of the

dielectric medium. In a magnetoplasma (2):

$$G_2^t = Z_o[A\cdot(\frac{1}{A} - \sin^2\theta)^{\frac{1}{2}} + D\cdot\sin\theta] \qquad (7\text{-}17)$$

$$G_2^r = Z_o[A\cdot(\frac{1}{A} - \sin^2\theta)^{\frac{1}{2}} - D\cdot\sin\theta] \qquad (7\text{-}18)$$

Here $\theta$ is the angle of incidence (measured to the negative y axis in free space as shown in Fig. [7-2]). Note that because of the quantity D due to an anisotropic medium, $G_2^t$ and $G_2^r$ are not equal as they would be in the isotropic medium. This non-reciprocal wave impedance is explained physically by the excitation of em waves at the dielectric-magnetoplasma interface due to the oblique incident em waves, which is given in Section 10-1 in detail. This is the one of the key factors for the explanation of the non-reciprocal reflection.

The reflection coefficients at the interface between a dielectric medium and a plasma medium (y=ℓ in Fig. [7-2]) is, therefore, given by

$$R_1 = \frac{|{}_1H_z^r|}{|{}_1H_z^t|} = \frac{G_1^t - G_2^t}{G_1^r + G_2^t} \qquad (7\text{-}19)$$

and

$$r_1 = \frac{|{}_1E_x^r|}{|{}_1E_x^t|} = \frac{\frac{1}{G_1^t} - \frac{1}{G_2^t}}{\frac{1}{G_1^r} + \frac{1}{G_2^t}} \qquad (7\text{-}20)$$

From analogy with transmission line theory, the impedance $Z_1$ seen at the interface between free space and a dielectric medium (y=0 in Fig. [7-2]) is given by

$$Z_1 = G_1^t \frac{1 + r_1 \exp(-j2k_1 \ell_1)}{1 + R_1 \exp(-j2k_1 \ell_1)} , \qquad (7\text{-}21)$$

where $k_1 = k_o(K_M - \sin^2\theta)^{\frac{1}{2}}$ is a wave number in a dielectric medium and $\ell_1$ is the thickness of the dielectric layer on the plasma medium.

Finally the reflection coefficient at the interface between free space and a dielectric coated magnetoplasma (y=0 in Fig. [7-2]) is given by

$$R_o = \frac{|{}_oH_z^r|}{|{}_oH_z^t|} = \frac{G_o^t - Z_1}{G_o^r + Z_1} . \qquad (7\text{-}22)$$

If D given in Eq.(7-17) and (7-18) is complex due to the presence of collisions in a magnetoplasma, it will be found that the reflection coefficient $R_o$ is nonreciprocal when a dc magnetic field is reversed. That is, reversal of the direction of propagation, or alternatively the sense of the dc magnetic field, changes the magnitude of the reflection coefficient. The physical explanation for the necessity of collisions in the nonreciprocal reflection is given in Section 10-1 in detail. This phenomenon is exploited to develop nonreciprocal devices such as isolators for use at millimeter and submillimeter wavelengths.

# Chapter 8

## EXPERIMENTAL PROCEDURE

This chapter is concerned with establishing the electric properties of the semiconductors used as the plasma medium. The experimental apparatus and the procedure for the measurement of the reflection from the magnetoplasma are presented. Brief discussions on the design, construction and operation of HCN laser and IR detector are also given in this chapter. Details are presented elsewhere [Kanda, 1971].

## 8-1 Properties of Solid State Plasma

At first the experiments were demonstrated at 94 GHz at room temperature using n-type GaAs (94 GHz reflection beam isolator). Then the final experiments were performed at the wave length of 337 μm using n-type InSb (IR reflection beam isolator).

### 8-1-1 GaAs

O. Madelung [1964] quoted the experimental results for the effective mass of electrons in n-type GaAs as $m^*=0.067m_o$ and the static dielectric constant as $K_L=12.53$. The mobility of the free carriers and the carrier concentration are estimated by either Hall

measurement or van der Pauw measurement [van der Pauw, 1958]. For nondegenerate n-type semiconductors the Hall coefficient is given by

$$R_H = - \frac{r_R}{ne} \qquad (8\text{-}1)$$

where the factor $r_R$ is determined by the scattering mechanism. For n-type GaAs it is reasonable to assume that the polar optical scattering is dominant at room temperature. Since the relaxation time approximation fails for polar scattering, the calculation of $r_R$ for the case of polar scattering is not simple. B.F. Lewis and E.H. Sondheimer [1955] have calculated $r_R$ for this case using a variational method, and the factor $r_R$ for polar optical scattering is around 1.01 at room temperature. Geometric effects due to the shape of the Hall sample and variation of Hall mobility with magnetic field are also discussed elsewhere [Madelung, 1964]. The van der Pauw measurement, on the other hand, does not depend on the geometry of a planar sample or the position of the contacts. Hence the whole sample used in the experiment was used in the van der Pauw measurement. The parameters of n-type GaAs used in the experiment are summarized in Table [8-1].

### 8-1-2 InSb

The effective mass measured from the Faraday effects at the room temperature in n-type InSb was $m^*=0.021m_o$, and the value taken for static dielectric constant for n-type InSb is $K_L = 17.88$ at room temperature [Hogarth, 1965]. The mobility and carrier density of n-type InSb were measured by performing either Hall measurement or van der Pauw measurement [van der Pauw, 1958]. It is known that in intrinsic InSb above 200°K both acoustic and polar optical mode scatterings are significant. The ratio of Hall mobility to the conduction mobility $r_R$ has been evaluated from a variational transport calculation by H. Ehrenreich [1959], and $r_R$ is found to be 1.01 at room temperature. After taking into account this correction, the parameters of n-type InSb at the temperature of 284°K and 270.6°K are listed in Table [8-1].

## 8-2 Experimental Set-up and Procedure

The experimental apparatus is designed to measure the non-reciprocal reflection from the surface of a semiconductor (GaAs or InSb) covered by a dielectric medium. In the millimeter wavelength region, the experiments were performed at 94 GHz, and n-type GaAs was used as a plasma medium. In the submillimeter wavelength region, the experiments were performed at

TABLE 8-1. Electric Properties of n-type GaAs and InSb

| | GaAs | InSb | |
|---|---|---|---|
| Temperature | 300°K | 284°K | 270.6°K |
| Electron Effective Mass | $0.067m_o$ | $0.021m_o$ | $0.021m_o$ |
| Dielectric Constant | 12.53 | 17.88 | 17.88 |
| Electron Mobility | $6.1\times10^3 cm^2/V\text{-}sec$ | $7.4\times10^4 cm^2/V\text{-}sec$ | $7.9\times10^4 cm^2/V\text{-}sec$ |
| Carrier Density | $7.1\times10^{14}/cm^3$ | $1.25\times10^{16}/cm^3$ | $1.06\times10^{16}/cm^3$ |

337 μm from HCN lasers, and n-type InSb was used as a plasma medium.

### 8-2-1 94 GHz Reflection Beam Isolator

The experimental apparatus shown in Fig. [8-1] is designed to measure the reflection from the interface between a dielectric and solid state plasma. The semiconductor used for the experiment is n-type 1.44 Ω-cm GaAs which was mechanically polished and chemically etched [$H_2SO_4(4) + H_2O_2(1) + H_2O(1)$]. Pyramidially-cut dielectric (Stycast $\varepsilon=15\varepsilon_o$, Emerson and Cuming) was used as a "lossless" dielectric medium, and the mirror-polished GaAs was mounted on the bottom of the pyramid as shown in Fig. [8-2]. Quarter-wave matching plates (Stycast, Emerson and Cuming) were placed on the incident and transmitted sides. This device was placed at 300°K in the 1 inch air gap of a Varian 6-inch magnet which provides the magnetic field up to 15 kG.

The pyramidal horns, whose beam angle is around 7.6°, were used to provide the incident "plane" wave polarized in the plane of incidence, and as a detector pickup. These horns were set about 10 cm away from the sample in order to insure that the em wave incident on the surface of the dielectric was plane. A lock-in amplifier was used to amplify and read the signal from the crystal detector. In order to reduce the effects of

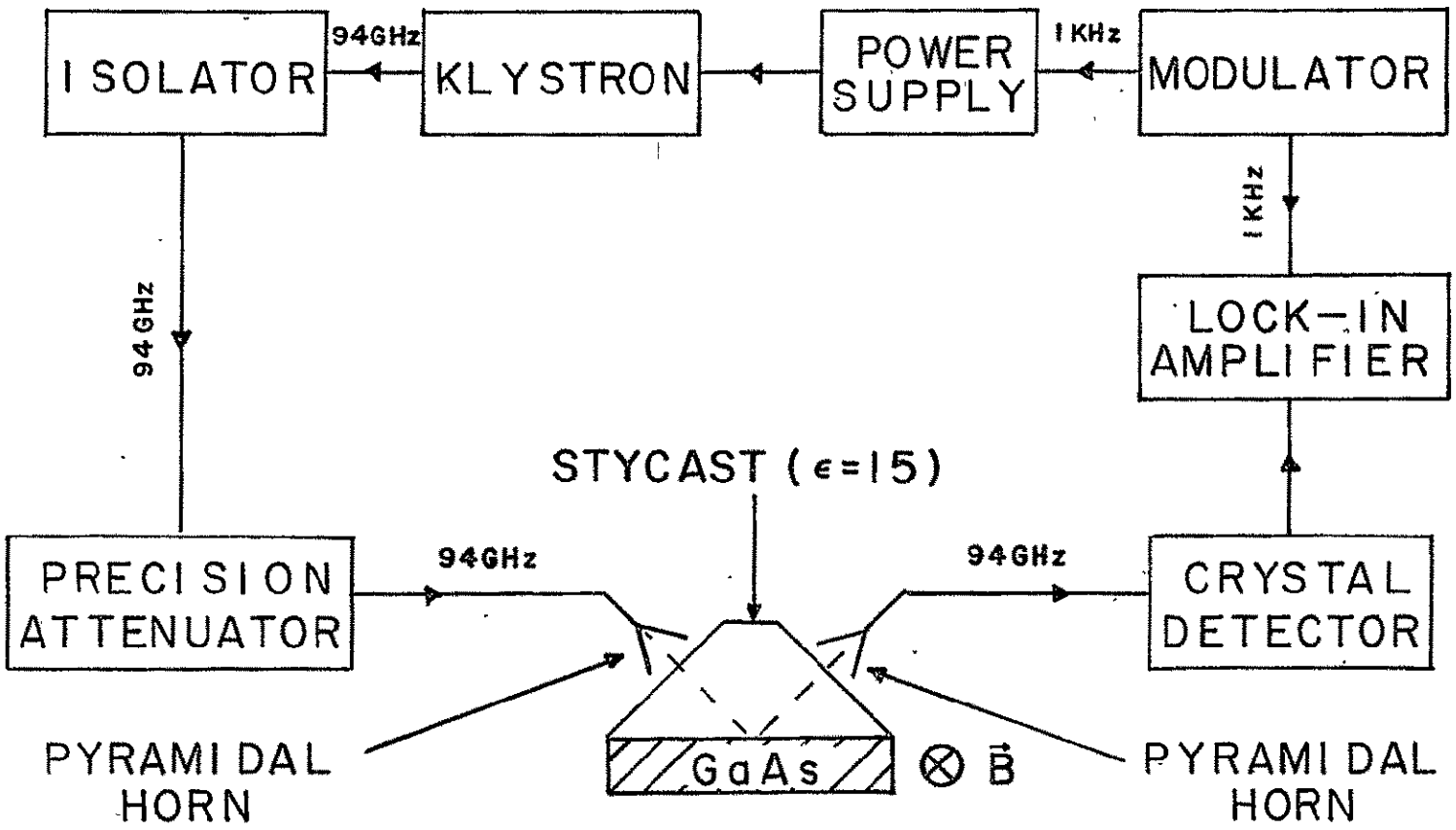


Fig. 8-1. Block Diagram for 94 GHz Experimental Set-up.

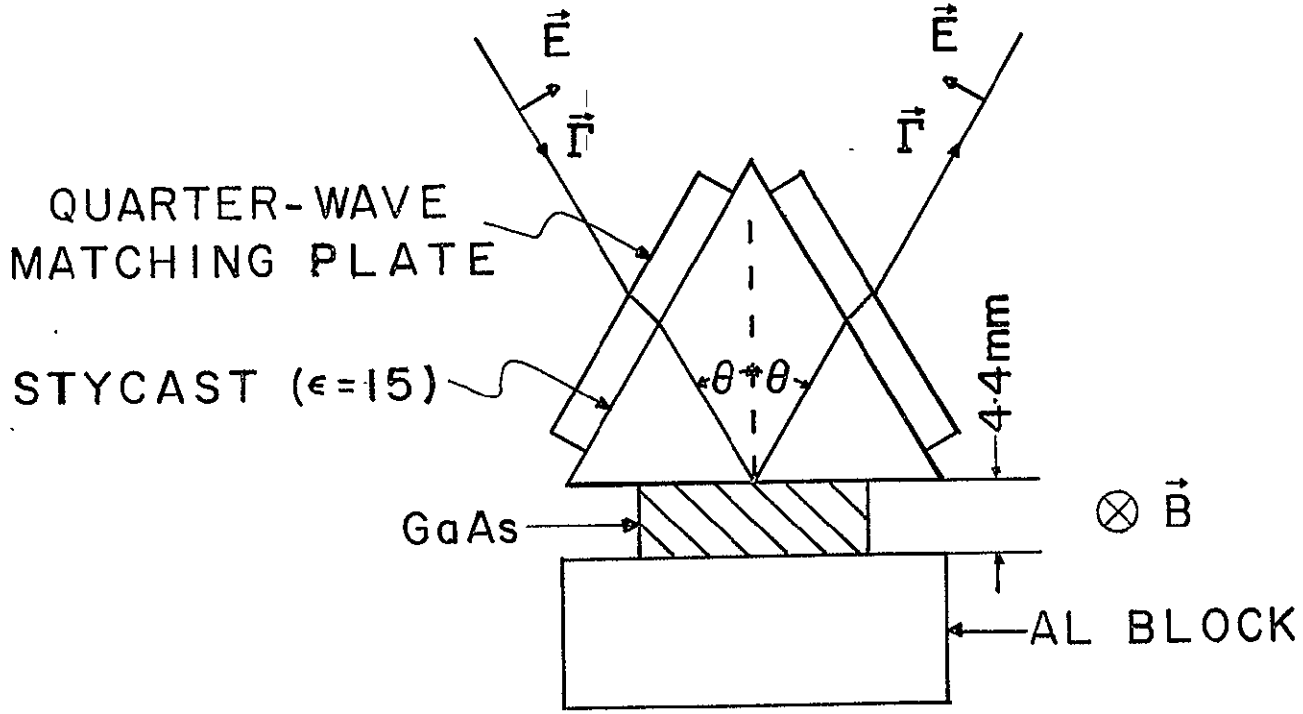


Fig. 8-2. 94 GHz Reflection Beam Isolator

stray signals, a window frame made out of Al foil was placed on the dielectric pyramid at the side of incidence.

The reflected power was measured as a function of magnetic field at a fixed angle. The measurements were repeated in 5 degree increments from 30° to 75°. Total insertion loss due to the isolator was somewhat difficult to measure because of use of pyramidal horns. The GaAs was replaced by a metallic conductor (polished brass), and the reflected power was measured again. The net insertion loss from absorption due to the GaAs was then determined by comparing the power reflected from GaAs and that reflected from the metallic conductor.

### 8-2-2 IR Reflection Beam Isolator

The block diagram of the experimental apparatus for the measurement of the far-infrared non-reciprocal reflection is shown in Fig. [8-3]. The InSb was mechanically polished and chemically etched. This semiconductor was covered with a high density polyethylene layer with a thickness of 0.1 to 0.3 mm as shown in Fig. [8-4]. The sample was cooled by the thermoelectric cooler in order to increase the mobility and to decrease the carrier concentration of intrinsic InSb. One side of thermoelectric cooler was water-jacketed, and the lowest temperature obtained on its surface was -2.4°C.

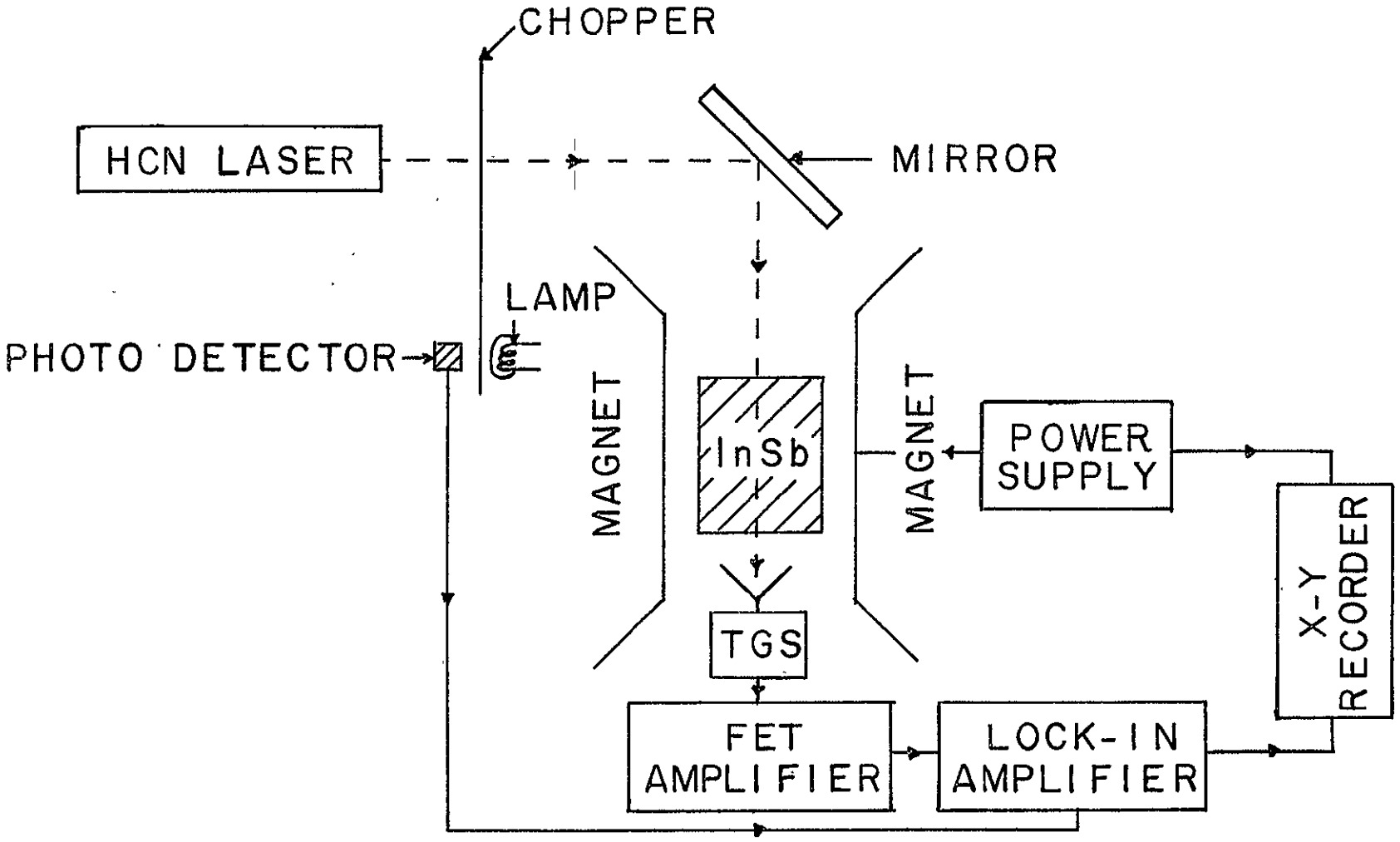


Fig. 8-3. Block Diagram for IR Experimental Set-up

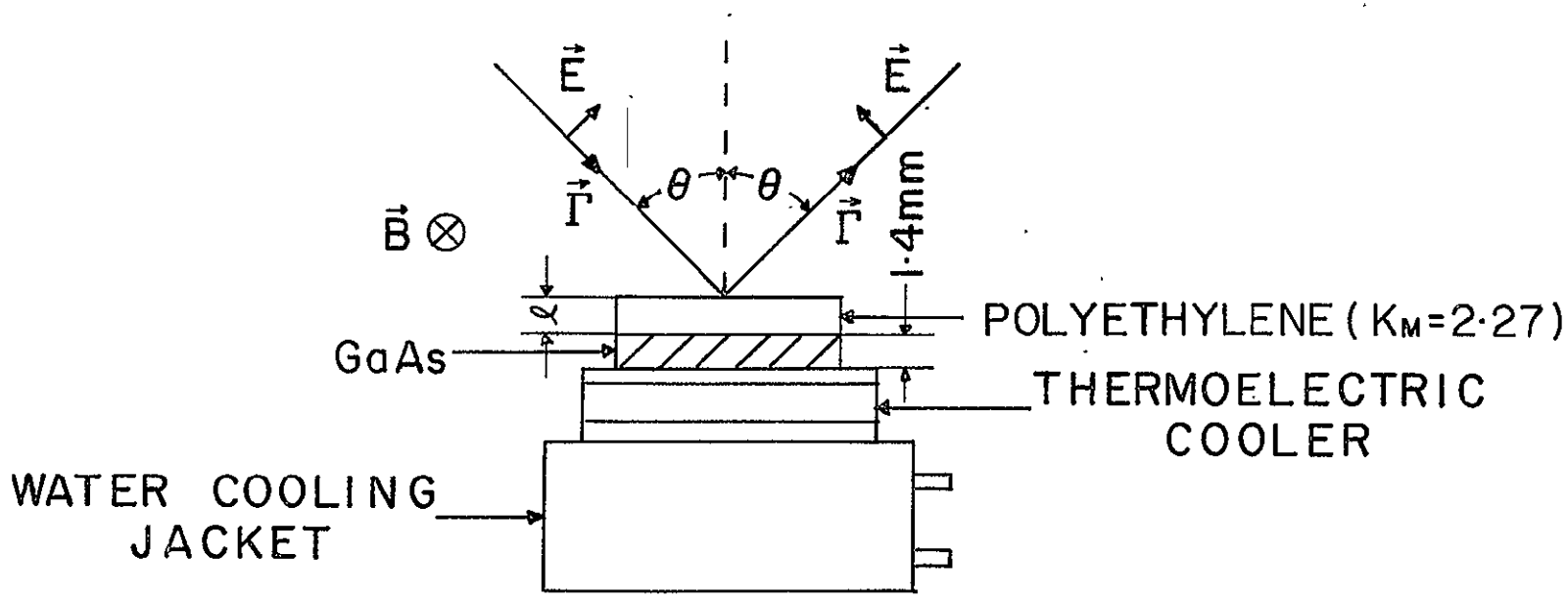


Fig. 8-4. IR Reflection Beam Isolator

This device was placed in the 1 inch airgap of a 6 inch Varian magnet which provided a maximum magnetic field of 15 kG.

An HCN laser of 337 μm was constructed as an infrared source. The laser was operated primarily at the wavelength of 337 μm, with typical stable output of approximately 10 mW CW. The linearly polarized output was extracted from a beam splitter. A lens was used as a window in order to focus the IR signal onto the sample, and the beam angle was approximately 3°. The reflected wave from the sample was received by a pyroelectric detector which was calibrated by a thermopile. The detected signal was amplified by a lock-in amplifier and then recorded on an x-y recorder as a function of applied magnetic field. A window frame made out of the lossy material (Eccosorb, Emerson and Cuming) was used in order to reduce stray IR signals. To reduce the effects of stray reflection, the area around the sample exposed to radiation was also covered with the lossy material (Eccosorb, Emerson and Cuming).

The reflection and insertion loss from the interface were measured in a similar manner as before. The accuracy of the measurements was limited mainly by the stability of the HCN laser output power. Invar mirror spacers and water-cooled cathode provided the stable operation. The laser tube was cooled by air, and entire HCN laser system was placed on a massive aluminum

optical table. The variation of the output power from the HCN laser was under 5% over long periods.

## 8-3 HCN Laser

Far-infrared laser action produced by discharges through various gases containing carbon, nitrogen and hydrogen in their elemental forms have been extensively studied [Gebbie, et al., 1964; Mathias, et al., 1965; Müller and Flesher, 1967]. This chapter presents briefly the design, construction and operation of a stable HCN laser, and the details are given elsewhere [Kanda, 1971].

### 8-3-1 Physical Mechanism of HCN Laser

Several explanations for the physical mechanisms of HCN laser have been proposed on the basis that the stimulated emissions at the wavelengths of 337 μm and 311 μm are attributed to the transitions within rotational and vibrational states of the HCN molecule. D.R. Lide and A.G. Maki [1967] have found a set of vibrational levels in HCN which provides a satisfactory explanation for the stimulated emission. The intense lines at 337 μm and 311 μm are explained as transitions involving the $11^{1}0$ and $04^{0}0$ vibrational states, which are mixed by a Coriolis perturbation.

8-3-2 Design of Resonator

A wide variety of combinations of mirror radii can be used with any gas laser discharge tube to provide modes having desired values of diameter and angular spread. Practical resonator configurations which are most commonly used are confocal, semiconfocal and long radius configurations. Obviously not all combinations of mirror radii and separations are useable. Many of them originate diverging wave fronts that effectively focus all energy away from the mirror at the opposite end and result in very high diffraction loss. It is also known that lasers tend to operate in one or more high order modes if the geometry permits them to do so. The only way to force a laser to operate in a uniphase wave front is to design a laser so that all modes except the lowest order mode have diffraction losses sufficiently high so that the operation is below threshold.

The resonator employed for our HCN laser is the semiconfocal configuration which consists of one spherical mirror and one flat mirror. The resultant mode has a relatively large diameter at the spherical mirror and a relatively small diameter at the flat mirror. The advantage of a semiconfocal configuration is relatively stable adjustment of the mirrors, and the disadvantage is the relatively inefficient pumping since

the cone-shaped mode intersects only one-third of the total volume of the laser resonator.

The mode dimensions, which are defined as the radii for which the electric field falls to $e^{-1}$ of its maximum value at the surface of mirrors, for the semiconfocal resonator employed for our HCN laser are

$$\omega_1 = 2.22 \text{ cm} \quad ,$$

$$\omega_2 = 1.5 \text{ cm} \quad .$$

When the Fresnel number $N = \frac{a^2}{\lambda d}$ is chosen to be 1.6, average power loss for $TEM_{00}$ mode is 0.4% and that for $TEM_{10}$ mode is 7%. Thus the ratio of the losses of the two lowest modes is 17.5, and the aperture radius a is 3.28 cm.

---

### 8-3-3 Design of Beam Splitter

Although there are several methods for extracting energy from far-infrared gas lasers, a hole-coupling scheme is most commonly used because of the simplicity of its construction. Usual hole-coupling schemes are, however, found to have the following disadvantages:

1) Diffraction losses are quite high;
2) Mode distortion (especially of the fundamental mode $TEM_{00}$) is large;
3) There are ambiguities in designing the size of the coupling hole.

In order to eliminate these disadvantages, the energy extraction method employed is a dielectric beam splitter with the Michelson interferometer configuration, which is a taut polyethylene membrane and is set at an angle of 45° to the laser axis. The thickness of the polyethylene is chosen in order to provide constructive interference of the beams reflected from each of its surfaces. This thickness is given by an odd multiple of

$$t = \frac{\lambda}{4} (n^2 - 1/2)^{-\frac{1}{2}} , \qquad (8\text{-}2)$$

where $\lambda$ is the vacuum wavelength of the laser radiation and n is the refractive index of the polyethylene. For our HCN laser ($\lambda$ = 337 μm, n = 1.5) the thickness of the polyethylene membrane is 64 μm.

Some of the advantages of this polyethylene beam splitter are:

1) Diffraction losses are kept at a minimum because the full internal beam diameter is utilized;
2) Mode distortion is minimized;
3) The output beam is linearly polarized, which is especially a useful feature for our experiments;
4) The output coupling is easily varied by adjusting the side mirror shown in Fig. [8-5].

A disadvantage of this scheme is a reduction of Q of the resonator because of a very slight loss of the polyethylene.

The power reflectivity of the polyethylene film at the wavelength of 337 μm is about 4% so that the maximum fraction of power coupled out of the HCN laser is about 16%. This can be increased even more, if the laser gain permits, by using a multiple parallel membrane with an appropriate spacing.

### 8-3-4 Final Laser System

Fig. [8-5] shows the schematic of an HCN laser system operating 337 μm and 311 μm. The main optical resonator is inside the evacuated tube and is fully adjustable from the outside through the vacuum seals. The alignment of the mirrors was accomplished by using a He-Ne gas laser. The water-cooled cathodes were constructed from the copper plumbing items and were hollow in order to increase the discharge area and thus to provide a uniform discharge. Strong lasing action has been observed at 337 μm and 311 μm with several chemical compounds [Gebbie, et al., 1964; Mathias, et al., 1965; Müller and Flesher, 1967]. A mixture of methane and ammonia was used for our HCN laser. The HCN laser requires a gas flow and exhaust system since the electric discharge dissociates the gas molecules,

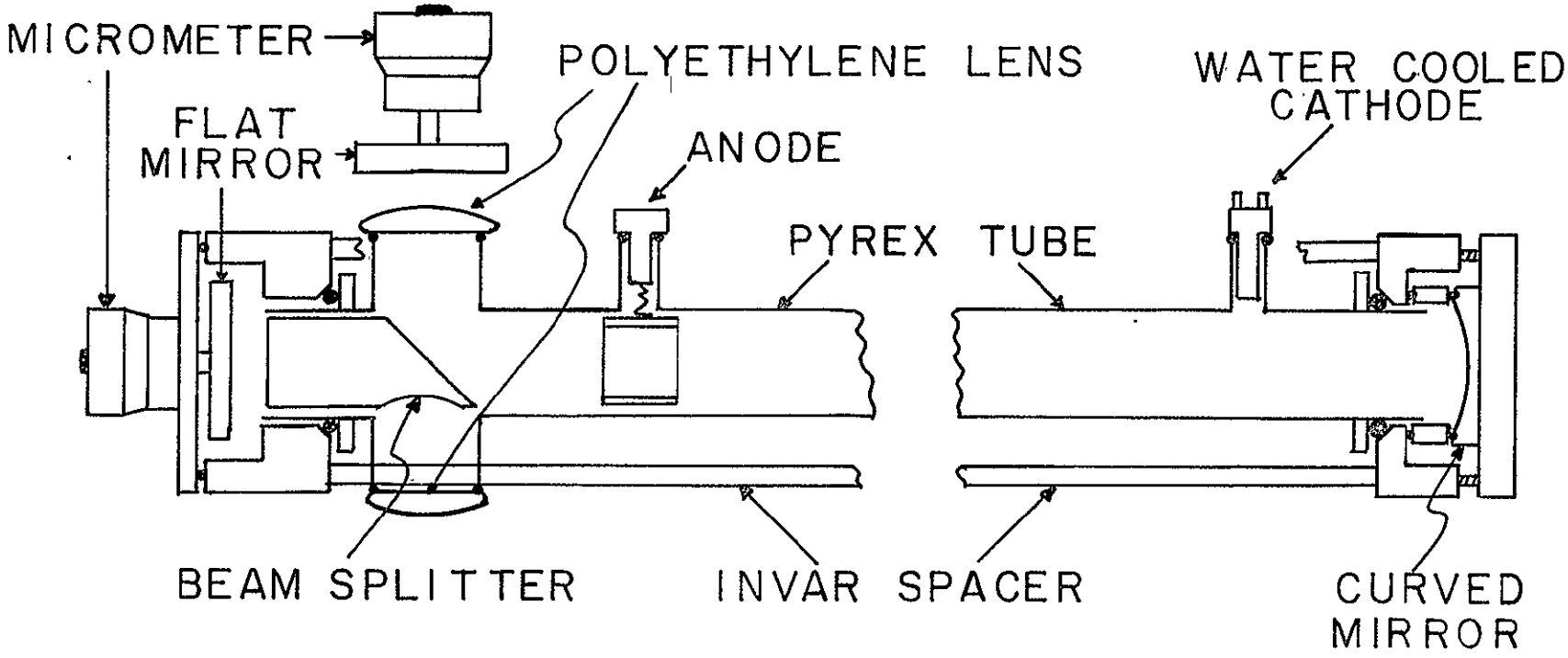


Fig. 8-5. HCN Laser

and the resulting constituents are not reusable. The gas discharge operates at about 1.4 kV while the firing voltage is about 2.5 kV, but these voltages depend upon the pressure and flow of the methane ammonia mixture. Final specifications for our HCN laser system are as follows:

| | |
|---|---|
| Length of laser tube | 2.1 m , |
| Length of usable discharge | 1.7 m , |
| Inside diameter of laser tube | 7.5 cm , |
| Curvature of mirror | 4 m , |
| Pressure of methane ammonia mixture | 0.8~5 mmHg , |
| Current limiting resistor | 1.8 kΩ , |
| Firing voltage | 2~3 kV , |
| Operating voltage | 1.2~1.6 kV , |
| Operating current | 0.3~0.8 A , |
| Power output | 16 mW at 337 μm , |
| | 5 mW at 311 μm . |

## 8-4 Infrared Radiation Detector

The detectors used for infrared radiation may be divided into two distinct groups, thermal detectors and photodetectors. The thermal detectors use the heating effect of the radiation and depend on the number of the effective quanta of the radiation absorbed. The characteristics of the thermal detectors are that their

performance is independent of wavelength, and that the time constant is relatively long. The photodetectors, on the other hand, make use of the quantum photoelectric effects and depend on the total energy absorbed. One of the great advantages of the photodetectors over thermal detectors is that much shorter time constants are obtainable.

The infrared radiation detector employed in our experiments is the pyroelectric detector [Beerman, 1967]. The actual sensor is a pyroelectric crystal exhibiting spontaneous polarization which is temperature dependent. Although such materials as triglycine sulfate (TGS), triglycine fluoberyllate (TGFB), lithium sulfate, Rochelle salt, barium titanate and lead zirconate titanates (PZT) are all pyroelectric, TGS has given better performance than these other crystals.

The pyroelectric detector used was a piece of TGS 4 $mm^2$ in area and 0.5 mm thick. The two opposite sides of the rectangular shaped sample were silver coated to create a capacitance with a thermal sensitive dielectric constant. Electrodes are attached to the silver coating and connected to the high input impedance 2 stage FET amplifier.

The pyroelectric detector is less sensitive than photodetectors and has a long time constant. However, it can detect long wavelength radiation without

cryogenic cooling. Also the pyroelectric detector, which is in principle a pure capacitor, does not show Johnson noise and is generally limited by the amplifier noise.

# Chapter 9

## THEORETICAL AND EXPERIMENTAL RESULTS

This chapter presents the theoretical and experimental results. Two geometries were considered: GaAs-dielectric interface at 94 GHz; free space-dielectric coated InSb interface at 337 μm. In all cases the polarization of the incident electric field is in the plane of incidence, and the direction of propagation is transverse to the magnetic field. A discussion of the theoretical and experimental results and sources of experimental error are also given.

### 9-1 94 GHz Reflection Beam Isolator

Theoretical reflection loss from the interface between free space and GaAs as shown in Fig. [9-1] indicates that there is very small isolation with high insertion loss, and even for other reasonable choices of parameters n, μ, B and θ [Seaman, 1969]. Therefore this device does not look promising for device application. It was thought that the high lattice dielectric constant ($K_L$=12.53 for GaAs and $K_L$=17.88 for InSb) might have washed out a large non-reciprocal behavior observed in the ionosphere by N.F. Barber and D.D. Crombie [1959]. Thus, the reflection from the interface between a dielectric medium and GaAs was studied

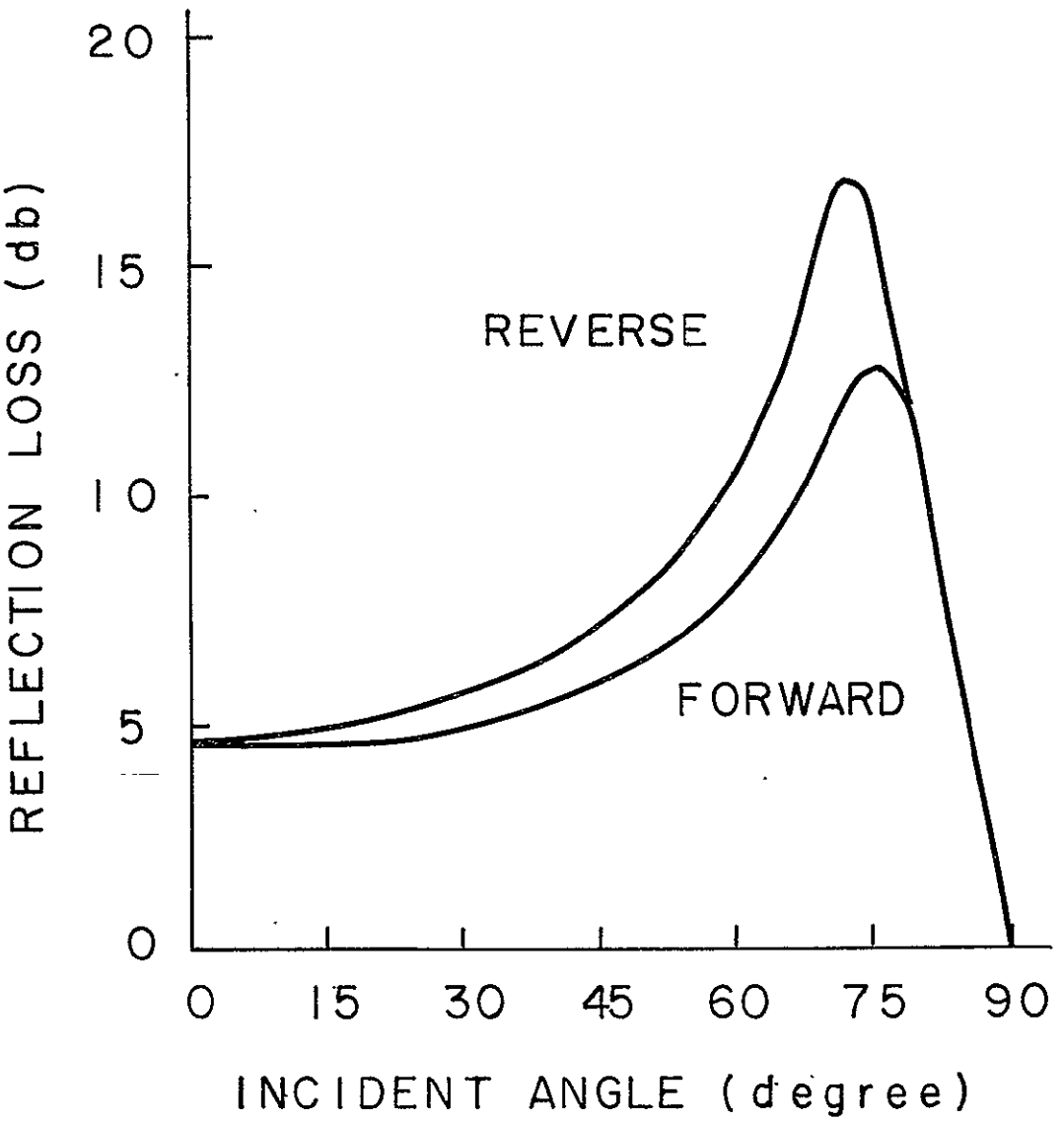


Fig. 9-1. Theoretical Reflection Loss of GaAs at 94 GHz as a Function of Incident Angle [Parameters of GaAs are listed in Table 8-1. Geometry of 94 GHz Reflection Isolator is shown in Fig. 7-1a with B=13.2 kG].

to achieve better isolation with smaller insertion loss.

Theoretical and experimental reflection loss from GaAs with a semi-infinite dielectric ($K_M$=15) for the electric field polarized in the plane of incidence at 94 GHz and at 300°K are shown in Fig. [9-2] for a dc magnetic field of 13.2 kG as a function of incident angle, and in Fig. [9-3] at a fixed incident angle of 57.5° as a function of a dc magnetic field.

Isolation of 12 db with 11 db insertion loss was observed for the signal at an incident angle of 57.5° whereas the theory predicts 44 db isolation with 5 db insertion loss at an incident angle of 65°. The deviation between theoretical and experimental results were great. In the next several paragraphs, possible sources of experimental error are discussed.

The surface of GaAs was mechanically polished and was flat and smooth to within a small fraction of the wavelength at 94 GHz. The thickness of GaAs was 4.4 mm which was more than 9 skin depths, where the skin depth is defined as the depth at which the magnitude of a field quantity decreases to $e^{-1}$ (about 36.9%) of its value at the surface. Therefore the reflection from the back side of the GaAs was negligible.

The parameters of GaAs were determined by the van der Pauw measurement which should give an overall

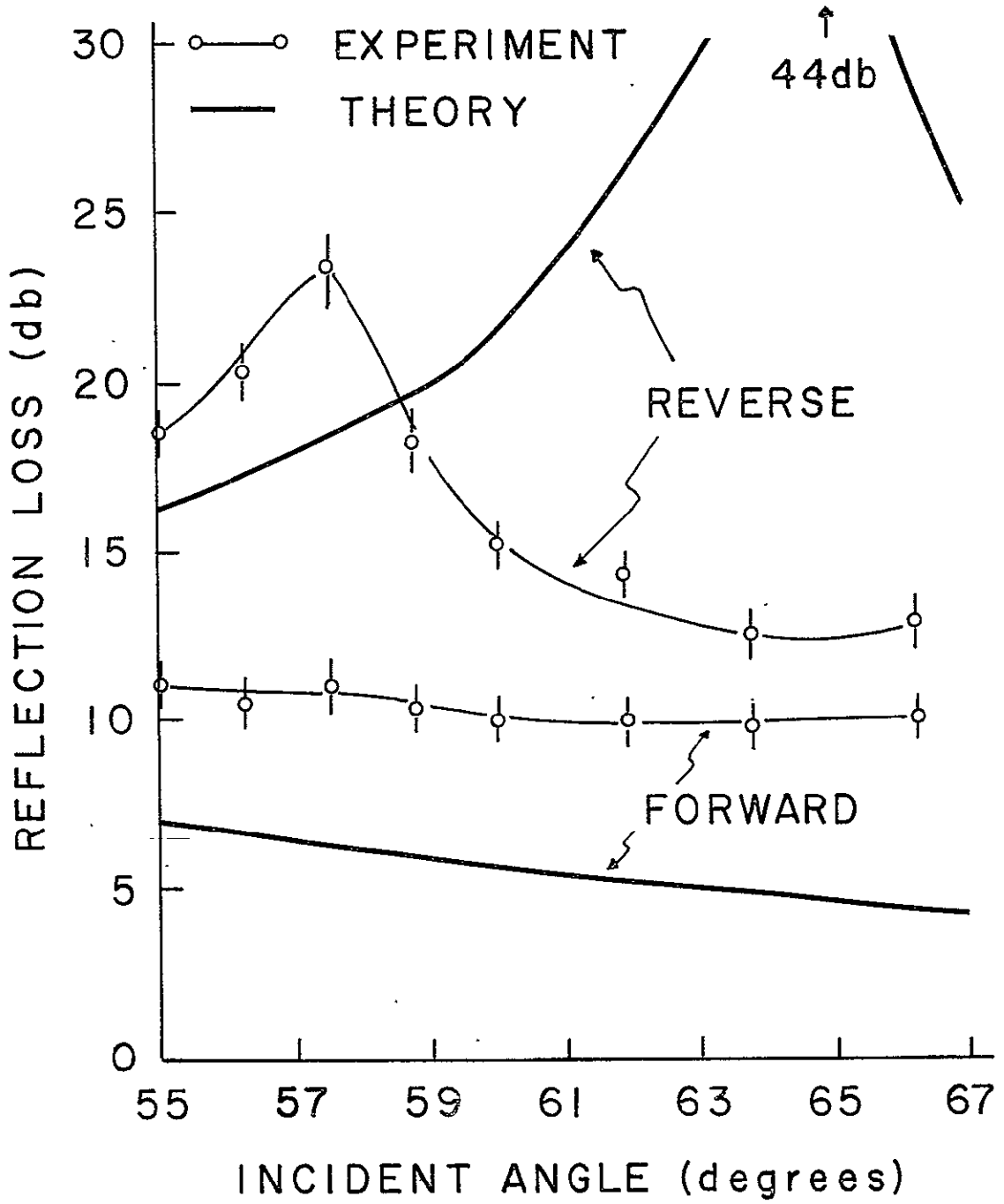


Fig. 9-2. Theoretical and Experimental Reflection Loss of GaAs at 94 GHz as a Function of Incident Angle [Parameters of GaAs are listed in Table 8-1. Geometry of 94 GHz Reflection Isolator is shown in Fig. 8-2 with B=13.2kG].

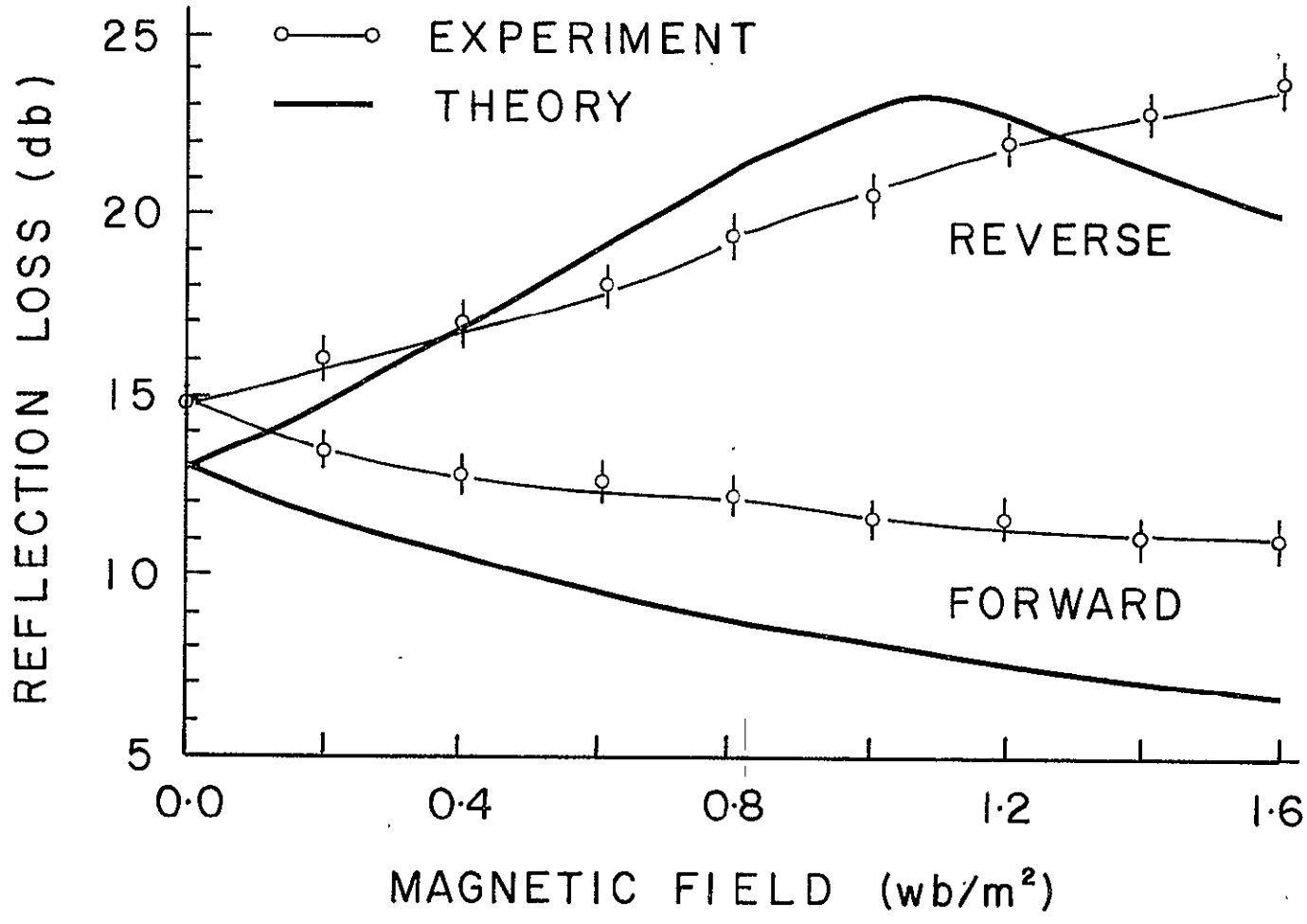


Fig. 9-3. Theoretical and Experimental Reflection Loss of GaAs at 94 GHz as a Function of Magnetic Field [Parameters of GaAs are listed in Table 8-1. Geometry of 94 GHz Reflection Isolator is shown in Fig. 8-2 with $\theta=57.5°$].

average value of the mobility and the carrier concentration of free carriers for the whole sample of GaAs. However, the measurements made on the various pieces indicated that the GaAs used in our experiment was not uniform and variations of 10% in these parameters were found to exist. This caused some trouble in the experiments.

The 94 GHz single from the pyramidal horns used for transmitting and receiving has a substantial angular spread between 2° to 5° depending on the tilt of the sample to the horn, and therefore the reflection obtained from the experiments was an "average" value of reflection for an angular spread. The spread in incident angles not only smeared out the sharpness of the reflection curve, but also reduced its peak as predicted from the theory (see Fig. [9-2]).

The effects of stray reflections and transmissions were minimized by the Al window frame placed on the pyramidally-cut dielectric at the side of incidence. The size of the window was, however, only about 5×7 wavelengths, and the non-plane wave behavior due to diffraction caused by this "small" window have washed out the sharpness of the reflection loss. This was also confirmed from the fact that a much smaller window, 3 wavelength square, completely destroyed the non-reciprocal phenomena.

In order to estimate the net insertion loss from absorption due to GaAs, the difference of reflected power from GaAs and from a metallic conductor was measured. Although the sample holder was made in such a way that it was possible to replace the GaAs by a metallic conductor without moving the sample holder itself, it was still difficult to position a metallic conductor exactly in the same position as was GaAs. This caused some error in estimating the incident power on the GaAs and thus the insertion loss.

The largest reflection loss was observed at the incident angle of 57.5° whereas the theory predicted a peak at 65°. Since the pyramidal horn has a beam angle of 7.6°, it is quite difficult to determine a definite angle of incidence, and thus the measurement of the incident angle of the wave from the normal was not accurate.

## 9-2 IR Reflection Beam Isolator

The primary experiment was conducted on the reflection from the interface between free space and the InSb, and then the further experiments were carried on the reflection from the interface between free space and a dielectric coated InSb. All theoretical calculations and experiments were performed at a wavelength of 337 μm from HCN laser. The theoretical and experimental

reflection loss from the interface between free space and InSb at 284°K are shown in Fig. [9-4] for a dc magnetic field of 15 kG as a function of incident angle, and in Fig. [9-5] at a fixed incident angle of 64° as a function of the dc magnetic field. General agreement between theoretical and experimental results is quite good although, as expected, these results indicate that this device does not look promising for the device application. It was thought that the high lattice constant in InSb ($K_L$=17.88) have washed out the large non-reciprocal reflection, and therefore the reflection from the interface between a semi-infinite dielectric medium and a solid state plasma was considered just as for the 94 GHz reflection beam isolator. The theoretical reflection loss from the interface between a dielectric layer ($K_M$=30) and InSb at a wavelength of 337 μm and at 300°K with a dc magnetic field of 13.2 kG was calculated using the theory given in Section 7-2 and is shown as a function of incident angle in Fig. [9-6]. The isolation of 34 db with 0.5 db insertion loss is predicted at an incident angle of 85.5°. The necessity of the dielectric medium whose dielectric constant is 30, however, makes this experiment difficult. Rutile, [$TiO_2$], barium titanate [$BaTiO_3$], barium-strontium titanate [(Ba-Sr)$TiO_3$] and a large number of bismuth compounds are known to have a high dielectric

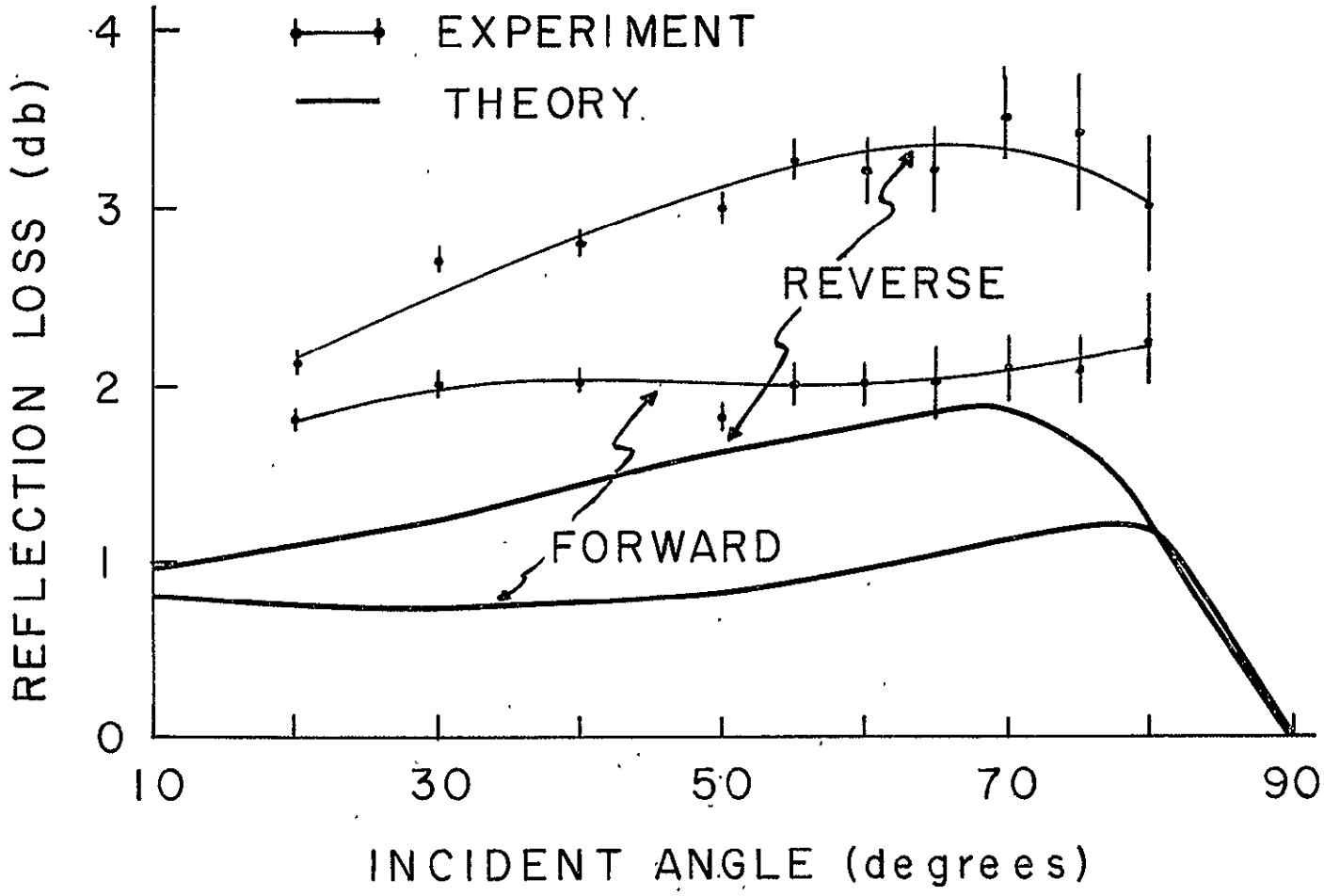


Fig. 9-4. Theoretical and Experimental Reflection Loss of InSb at 337 μm as a Function of Incident Angle [Parameters of InSb (T=284°K) are listed in Table 8-1. Geometry of IR Reflection Isolator is shown in Fig. 7-1a, with B=15kG].

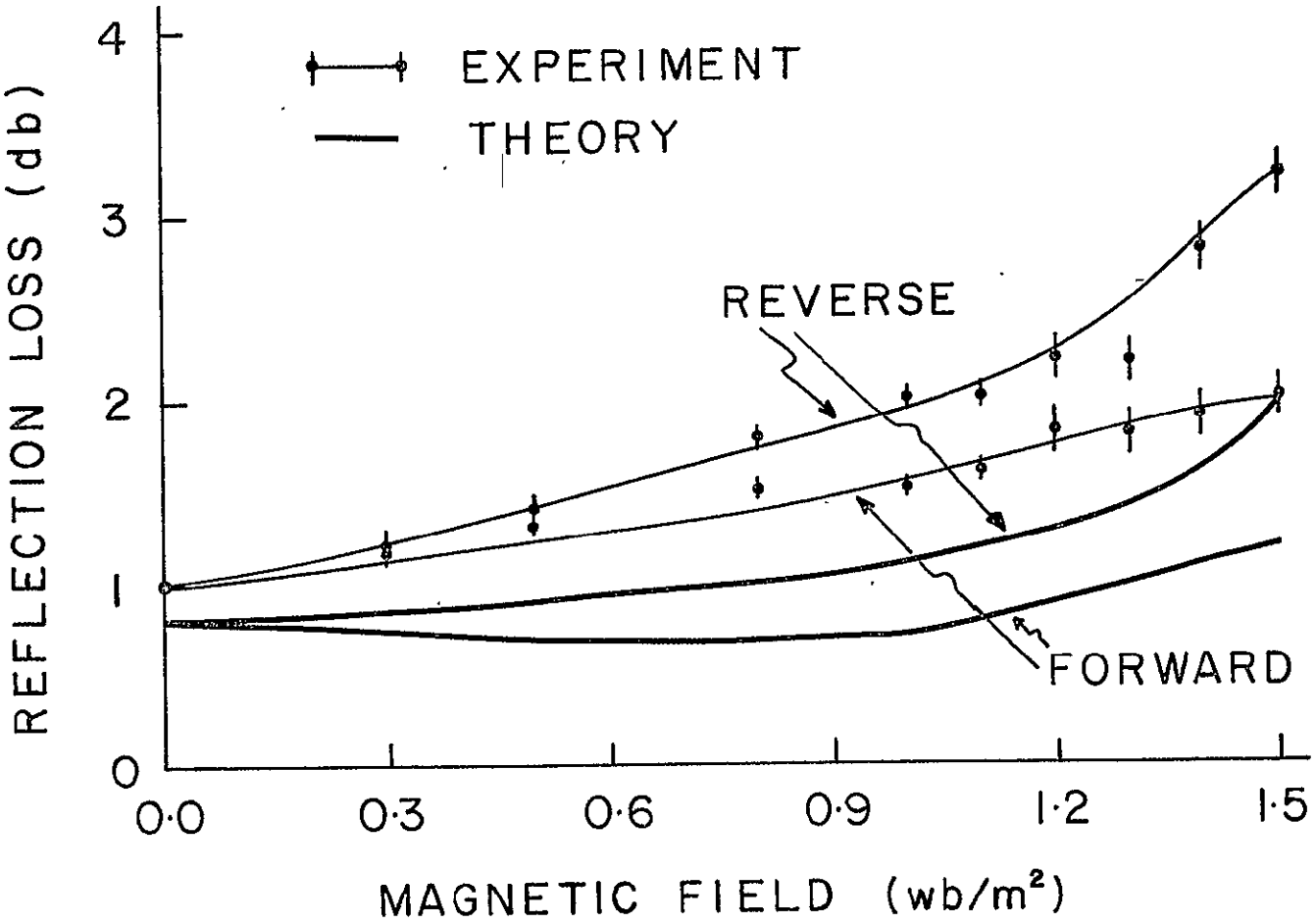


Fig. 9-5. Theoretical and Experimental Reflection Loss of InSb at 337 μm as a Function of Magnetic Field [Parameters of InSb (T=284°K) are listed in Table 8-1. Geometry of IR Reflection Isolator is shown in Fig. 7-1a with θ=64°].

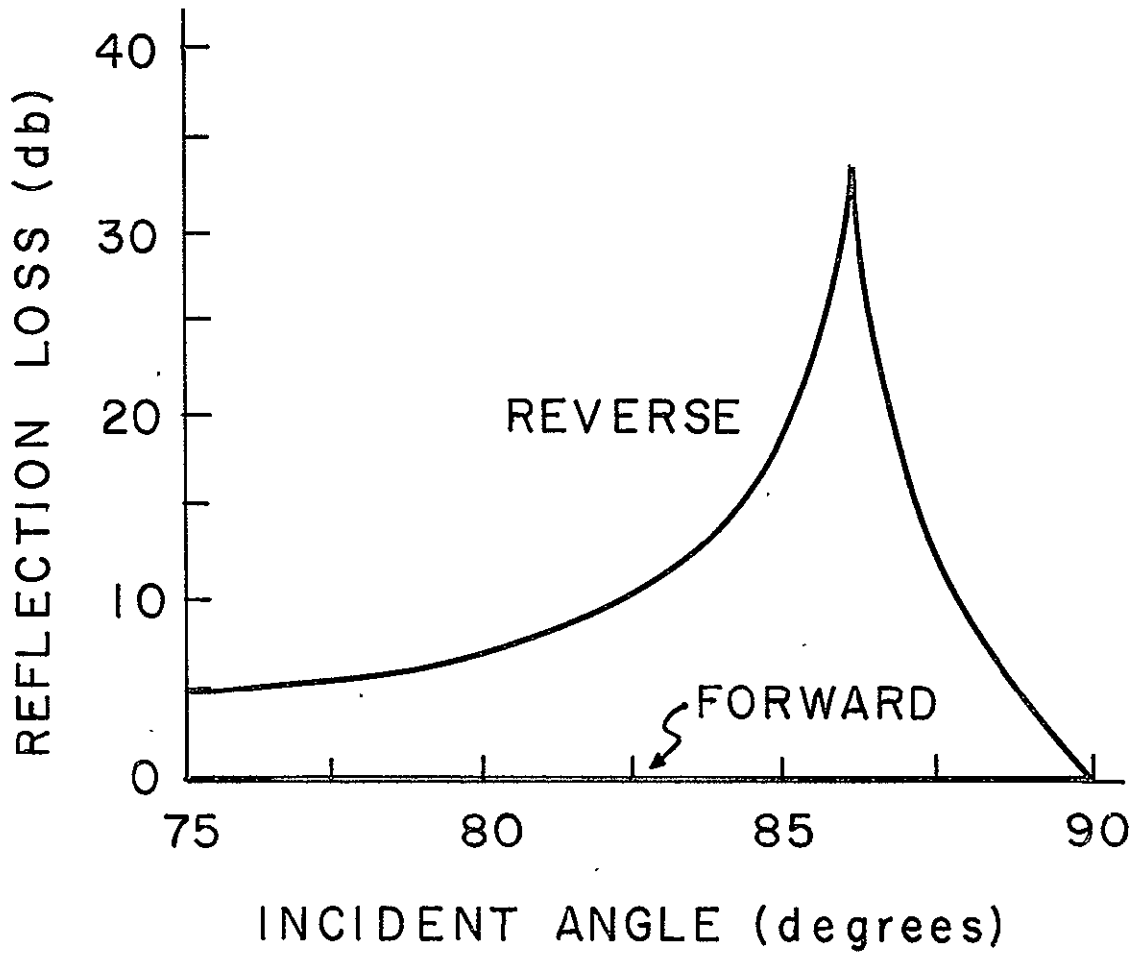


Fig. 9-6. Theoretical Reflection Loss of InSb at 337 μm as a Function of Incident Angles [Parameters of InSb (T=284°K] are listed in Table 8-1. Geometry of IR Reflection Isolator is shown in Fig. 7-1b with $K_M$=30 and B=13.2kG].

constant. But none of these high dielectric materials are transparent at the wavelength of 337 μm. The few materials, known to be transparent at this wavelength, (some semiconductors and some dielectric materials such as polyethylene, teflon and quartz) have a typical dielectric constant of around 10 or less, and none of these is even close to what is required for this experiment ($K_M$=30).

In order to overcome this difficulty, a thin dielectric layer placed on top of InSb was introduced as a matching transformer. Thus the reflection from the interface between free space and dielectric coated InSb was studied. The idea of this configuration was to create the same effect on the reflection from the interface between a high dielectric medium ($K_M$=30) and InSb by adjusting the thickness of a dielectric layer, whose dielectric constant is around 2, placed on top of InSb. The dielectric material chosen for this layer was high density polyethylene whose dielectric constant is 2.27, and its loss tangent (tan δ) is as low as $1.3\times10^{-3}$ at the wavelength of 337 μm [Breeden, 1968]. The possibilities of using a thin layer with a different dielectric constant for the purpose of matching have been considered and are given in Section 10-2.

The theoretical and experimental reflection loss from the interface between free space and dielectric coated InSb at 284°K are shown in Fig. [9-7] for the dc

magnetic field of 15 kG as a function of incident angle, and in Fig. [9-8] at a fixed angle of 65° as a function of dc magnetic field. The thickness of the high density polyethylene assumed in the theoretical calculations and used in the experiments was 250 μm. The general shapes of the curves for the theoretical and experimental results agree fairly well except at large incident angles. Since at large incident angles only a small IR signal was incident on InSb and consequently only a small IR signal was reflected off from InSb, the experimental data at incident angles over 75° were questionable. Therefore effort was made to shift the isolation peak to a lower angle, as discussed in the next paragraph.

From the heuristic argument the isolation peak takes place when the impedance of the dielectric medium is matched with that of the InSb. The impedance of the dielectric medium is given by $\eta\cos\theta$ where $\eta$ is the intrinsic impedance of the dielectric medium and $\theta$ is the incident angle. Similarly the impedance of the InSb is given by $\eta_1 \cos\theta_1$ where $\eta_1$ is its intrinsic impedance and $\theta_1$ is the angle of refraction in the InSb. When the intrinsic impedance $\eta$ of the dielectric medium and the angle of refraction $\theta_1$ in the InSb are given, the incident angle $\theta$ can be shifted to a lower angle by increasing the intrinsic impedance $\eta_1$ of the InSb.

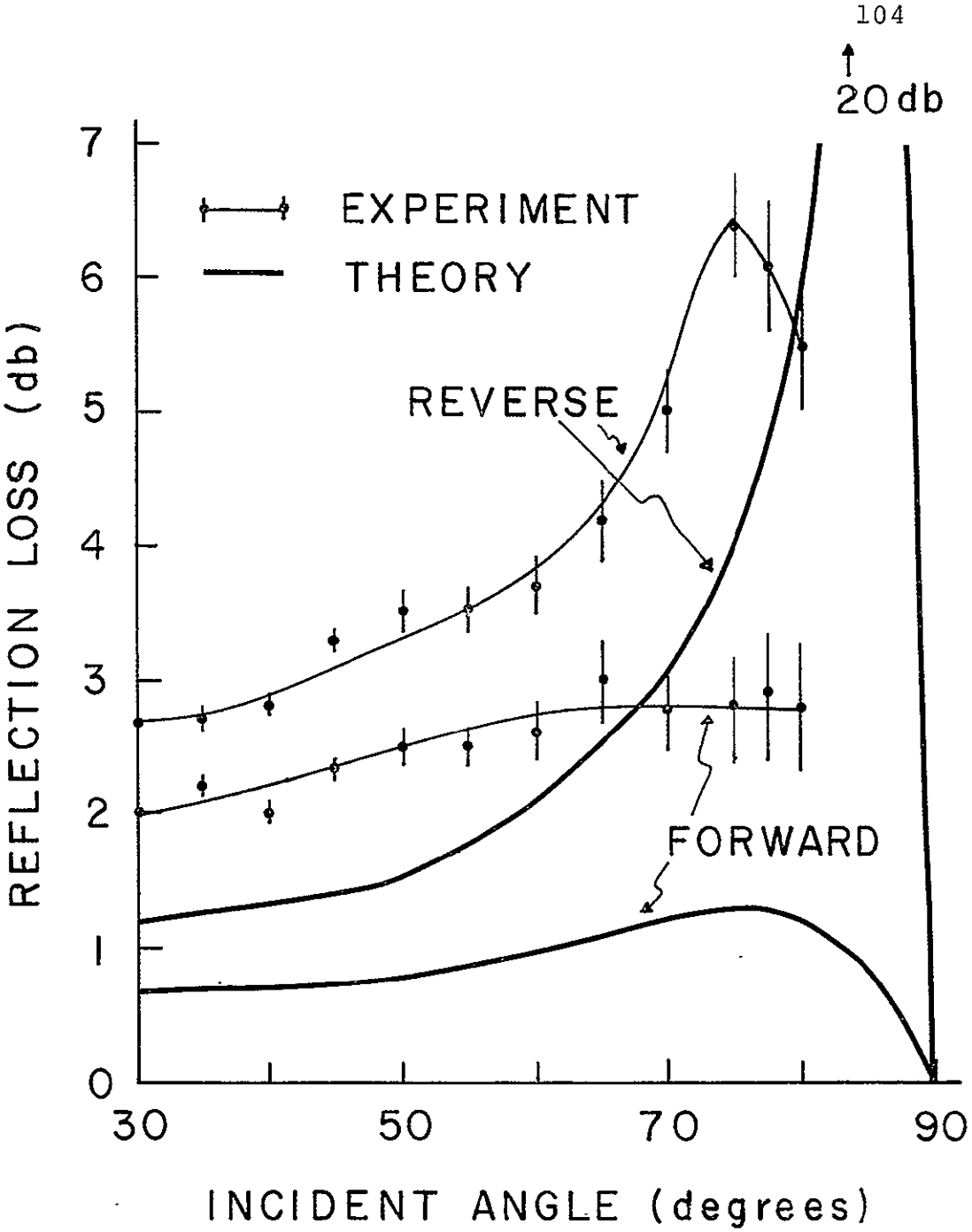


Fig. 9-7. Theoretical and Experimental Reflection Loss of InSb at 337 μm as a Function of Incident Angle [Parameters of InSb (T=284°K) are listed in Table 8-1. Geometry of IR Reflection Isolator is shown in Fig. 8-4 with ℓ=250μm and B=15kG].

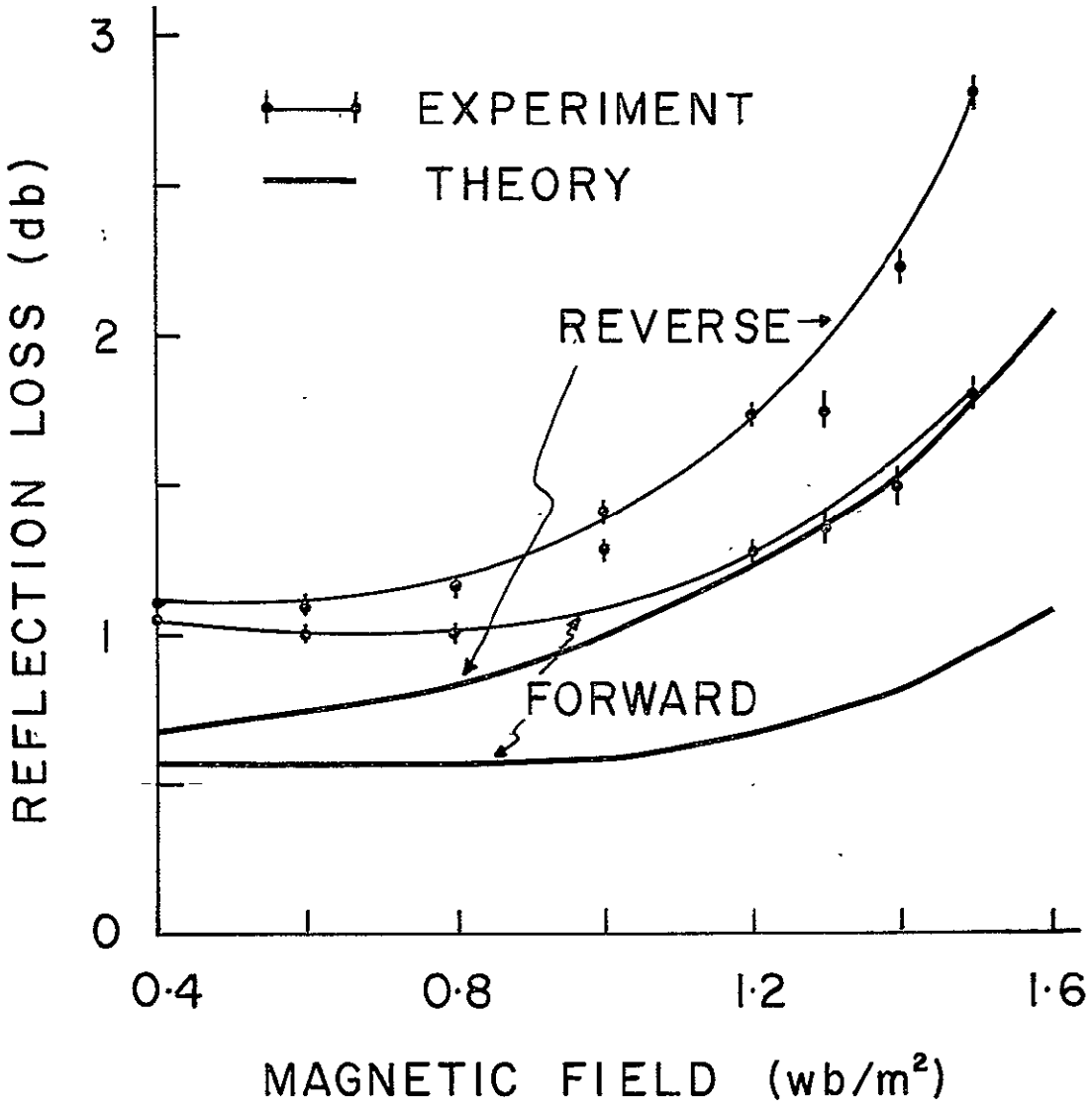


Fig. 9-8. Theoretical and Experimental Reflection Loss for InSb at 337 μm as a Function of Magnetic Field [Parameters of InSb (T=284°K) are listed in Table 8-1. Geometry of IR Reflection Isolator is shown in Fig. 8-4 with $\ell$=250μm and $\theta$=65°].

It is found theoretically that the intrinsic impedance of the InSb with a dc magnetic field can be increased with an increase of its mobility and a decrease of its carrier concentration. It is, therefore, expected that the peak of the isolation curve can be shifted to a lower incident angle by few degrees by increasing the mobility and decreasing the carrier concentration. One way to achieve this is to cool the InSb with a thermoelectric cooler. By cooling the InSb from 284°K to 270.6°K, the mobility increases by 7% and the carrier concentration decreases by 15%. This, in turn, shifts the peak of the isolation curve by 2°, which turns out to be a too small amount to ease experimental difficulties. In fact, a drastic shift of the isolation curve to a lower incident angle cannot be achieved only by increasing the mobility and decreasing the carrier concentration so long as polyethylene ($K_M$=2.27) is used as a matching transformer; further considerations are made in Section 10-2.

The theoretical and experimental reflection loss from the interface between free space and a dielectric coated InSb at 270.6°K is shown in Fig. [9-9] for a dc magnetic field of 12 kG as a function of incident angle, and in Fig. [9-10] for a fixed incident angle of 60° as a function of dc magnetic field. The thickness of the high density polyethylene assigned in the

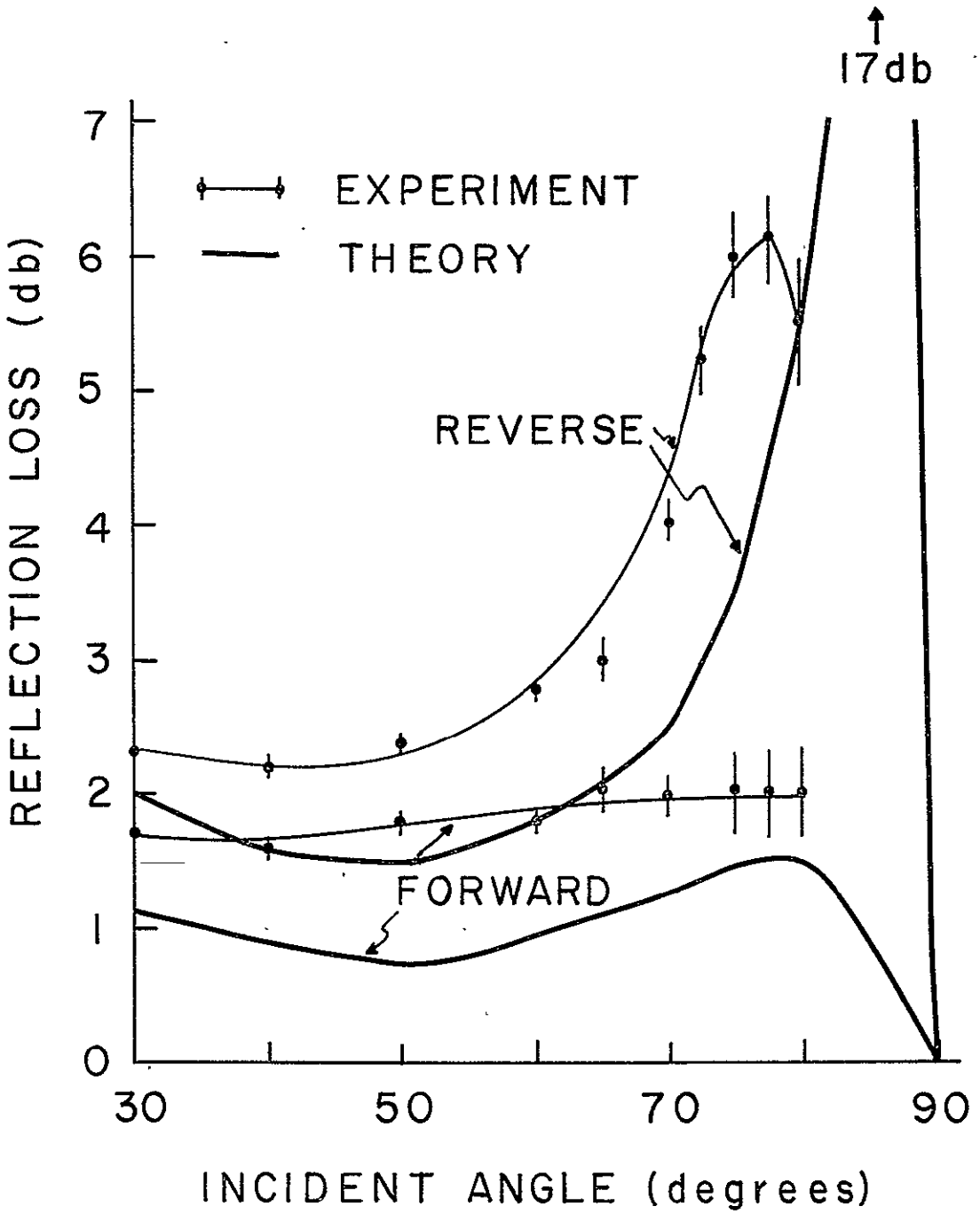


Fig. 9-9. Theoretical and Experimental Reflection Loss for InSb at 337 μm as a Function of Incident Angle [Parameters of InSb (T=270.6°K) are listed in Table 8-1. Geometry of IR Reflection Isolator is shown in Fig. 8-4 with ℓ=125μm and B=12kG].

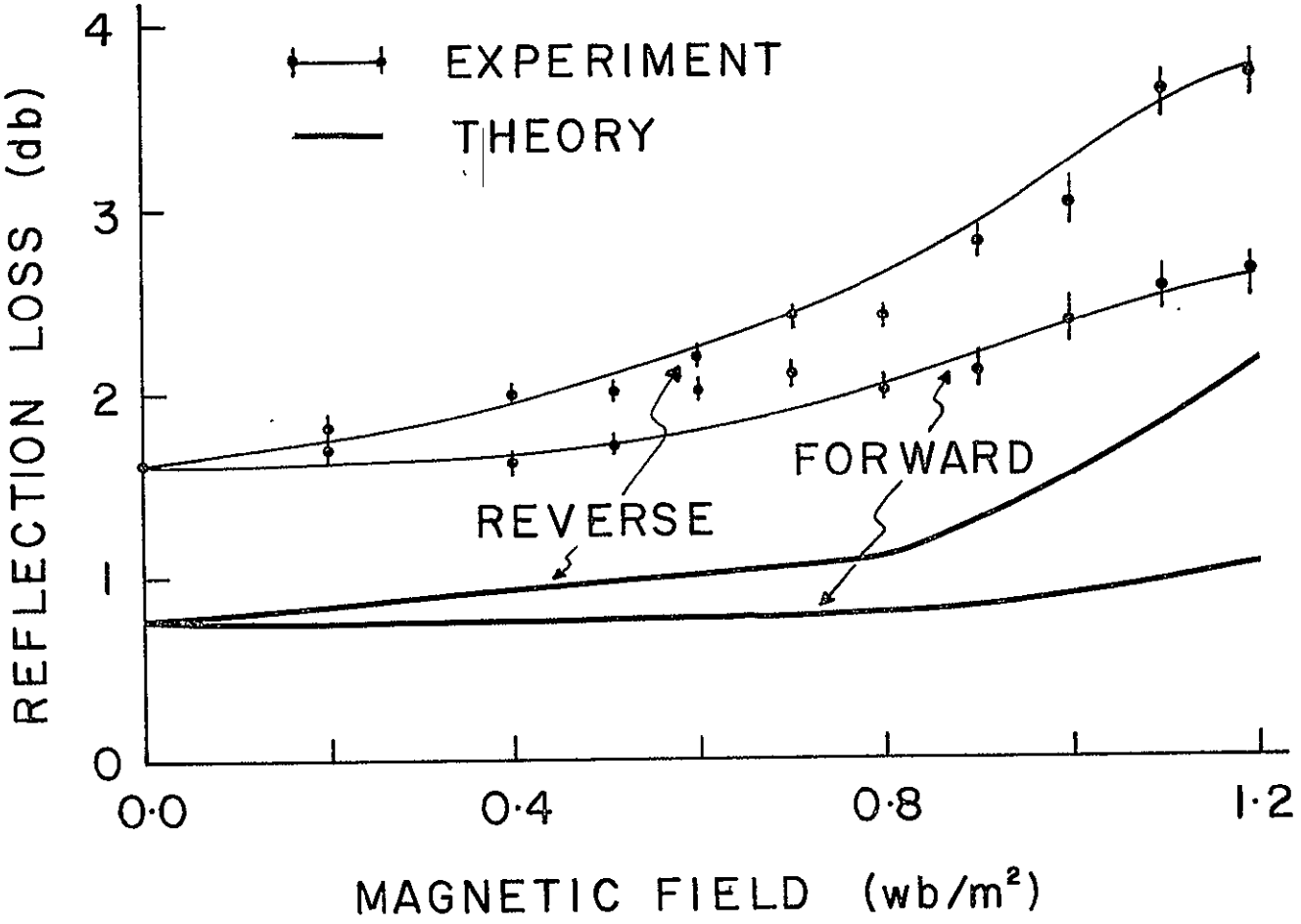


Fig. 9-10. Theoretical and Experimental Reflection Loss for InSb at 337 μm as a Function of Magnetic Field. [Parameters of InSb (T=270.6°K) are listed in Table 8-1. Geometry of IR Reflection Isolator is shown in Fig. 8-4 with ℓ=125μm and θ=60°].

theoretical calculations and in the experiments was 125 μm. The best data obtained experimentally as an application to an isolator were 4.2 db isolation with 2 db insertion loss at an incident angle of 77.5° with the dc magnetic field of 15 kG. With this magnetic field, the theory predicted 16 db isolation with 1 db insertion loss at an incident angle of 86°. Large discrepancies between theoretical and experimental results take place at incident angles over 80°, as discussed earlier. Therefore, further considerations are made in Section 10-2 in order to shift the peak of the isolation curve to a lower incident angle. Except at incident angles over 80°, the experiments seem to indicate that the theory is valid, and general agreement between theoretical and experimental results is quite good within experimental errors. In the next several paragraphs, possible sources of experimental error are discussed.

InSb was flat and smooth to within a small fraction of the wavelength (337 μm). Since the thickness of the InSb was 1.4 mm which was approximately equivalent to 70 skin depths, reflection from the back side of the InSb was negligible. The parameters of the InSb were measured by the van der Pauw method which gives accurate average values for whole samples. The laser output at 337 μm was carefully separated from that at 311 μm by

adjusting the fine tuning of the resonator. The beam splitter was used to extract the polarized output power, and the degree of polarization was ascertained to be over 99.9% [Evenson, 1969]. The long time stability of the output power of HCN laser was reduced to under 5%. The errors introduced in the results from these sources are, therefore, quite negligible.

The output power from HCN laser has an angular spread of around 1° depending on the tilt of the sample to the window of the laser. Therefore the reflection obtained from the experiments was an "average" value of reflection for an angular spread. The spread in incident angles not only smeared out the sharpness, but also reduced the peak of the reflection curve. Therefore the error caused by this source was significant especially at large incident angles where the reflection coefficient changes rapidly with incident angles (see Fig. [9-7] and [9-9]).

The thin layer of high density polyethylene placed on top of the InSb was used as an impedance transformer. Since the wavelength was quite short (337 μm) and interesting experiments had to be performed at large incident angles, the accuracy of the thickness of the high density polyethylene is important. Since the polyethylene was cut by milling, some error was expected due to the limit of machining accuracy.

In order to eliminate the stray reflections and transmission, a window frame made out of lossy material (Eccosorb, Emerson and Cuming) was placed in front of the InSb. This ensured that the detected signal was indeed the signal reflected from the InSb, and not stray transmission or reflection aside from InSb.

The semiconductor was replaced by a metallic conductor (polished brass), and the reflected power was measured again. The net insertion loss from absorption due to the InSb was then determined by comparing the reflected IR signal from the InSb and that from the metal. If the conductor was not positioned exactly in the same place as was InSb, the IR signal incident on each surface would be different, thus causing some error in estimating the insertion loss.

# Chapter 10

## DISCUSSIONS AND CONCLUSIONS OF PART II

In this chapter the behavior of the em waves reflected from a magnetoplasma is discussed. The physical quantities, such as the ellipticity of the electric field and the orbit of electrons in a magnetoplasma excited at the plasma surface due to an incident em waves are evaluated. In all cases the polarization of the incident electric field is in the plane of incidence, and the direction of propagation is transverse to a dc magnetic field. It is hoped that the evaluation of these physical quantities will lead to the physical understanding of the non-reciprocal phenomena. Finally applications of the device and possible refinements for isolators are also discussed.

### 10-1 Physical Explanation of Non-reciprocity

A dc magnetic field makes the plasma anisotropic. The origin of this anisotropy is due to the motion of the electrons in a dc magnetic field. A component of electric field perpendicular to a dc magnetic field can give rise to the transverse motion of electrons. This transverse velocity interacts with a dc magnetic field to produce motion in the Hall or $\vec{v}\times\vec{B}$ direction. As a result, off-diagonal terms appear in the matrix relating

the velocity (and the current) to an electric field. Therefore conductivity and dielectric constant become tensors. It can be shown that the nature of the magnetic force is such that the dielectric tensor is antisymmetric, and off-diagonal terms contain terms linear in the dc magnetic field as long as the field is small. This anisotropic effect in the plasma is one of the essential factors required for non-reciprocity.

As discussed in Section 2-3, in the case of propagation transverse to a dc magnetic field, the propagation constant is reciprocal. That is, reversal of the direction of propagation, or alternatively the direction of a dc magnetic field, does not change the propagation constant. Thus the question arises why non-reciprocal reflection takes place. In order to settle this, let us consider, first of all, the excitation of em waves due to an incident plane wave on a magnetoplasma.

The non-reciprocity arises from the interface between free space and the plasma. The coupling between the x and y components of the electric field through the dc magnetic field is expected from the Hall current due to the anisotropic property of the tensor dielectric constant. Since the Hall current has a definite sense with respect to the dc magnetic field, the amplitude of the electric field contributed by the Hall current contains the term linear in the field. That is, for

one direction of magnetic field the x component of electric field, for example, is coupled to the y component of electric field through a positive coefficient, and for the other direction of magnetic field is coupled through a negative coefficient as shown in Fig. [10-1]. Therefore, total electric field in the plasma is not reciprocal when the dc magnetic field is reversed. Consequently, the reflection coefficient at the interface between free space and InSb is non-reciprocal.

An explanation for the non-reciprocal reflection based on the changes in electron orbits in a magnetoplasma was proposed by K. Davies [1969]. His argument is extended here in order to give a more convincing physical explanation for the non-reciprocal reflection. Consider the situation when two identical waves are traveling through a plasma medium at equal but opposite angles to the vertical (see Fig. [7-1a]). In the absence of a dc magnetic field, the ratio of the x and y components of the electric field in a plasma is given by

$$\frac{E_y}{E_x} = \frac{-\sin\theta}{(K_\perp - \sin^2\theta)^{\frac{1}{2}}} \qquad (10\text{-}1)$$

where

$$K_\perp = K_L - \frac{\omega_p^2}{\omega(\omega - j\nu)} \qquad (10\text{-}2)$$

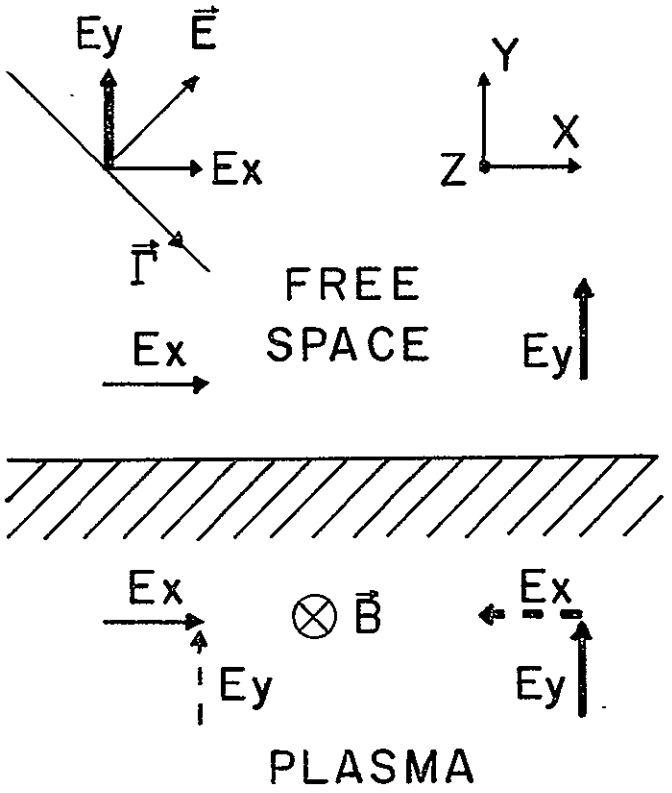


Fig. 10-1. Electric Field Excited in a Magnetoplasma (Electric fields excited through the Hall current are indicated by - - → and ▬▬→).

Thus if the plasma is lossy, i.e. $K_\perp$ is complex, the electric field in the plasma is elliptically polarized in the plane of incidence as shown in Fig. [10-2], (note the difference in x and y scales). Hence the orbits of electrons responding to this electric field are also elliptic. These elliptical motions can be decomposed into two oppositely rotating circular orbits with different radii. When a transverse dc magnetic field is applied, the radius of each circle is increased or decreased depending on the direction of a transverse dc magnetic field. The resulting electron orbits obtained by summing the two oppositely rotating circular orbits may be drastically different from those without a transverse dc magnetic field. That is, for one sense of magnetic field, the ellipse will be flatter than the case with no magnetic field, and for the other direction of magnetic field the ellipse will be more round, as indicated pictorially in Fig. [10-3a].

Fig. [10-4] shows the validity of the above physical interpretation. Fig. [10-4a] shows the orbits of electrons in a magnetoplasma with a dc magnetic field of 2 kG when non-reciprocity is quite small. It is found in Fig. [10-4a] that the orbits of electrons in a magnetoplasma are almost reciprocal with reversal of the dc magnetic field and hence small non-reciprocal reflection is expected. Fig. [10-4b] shows the orbits

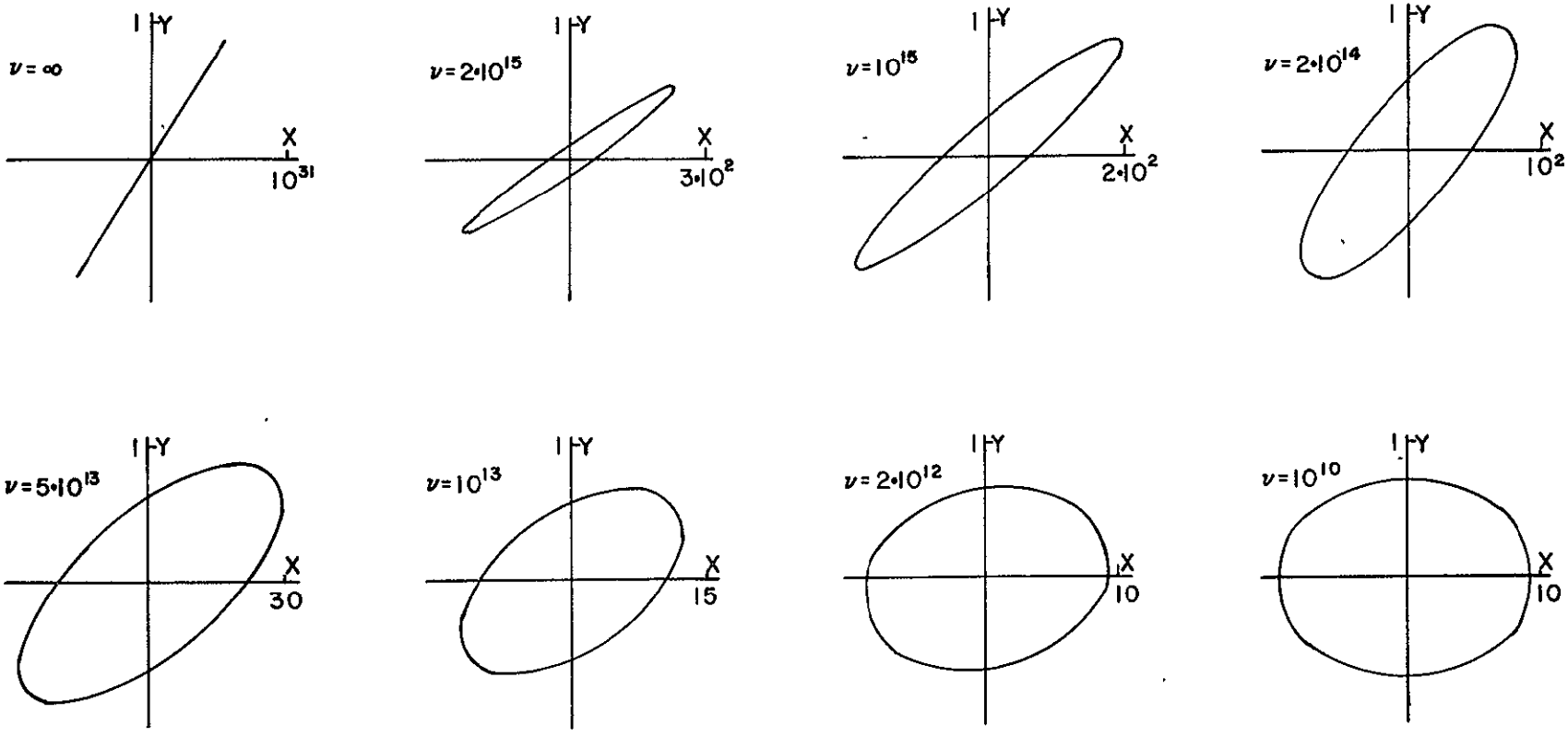


Fig. 10-2. Ellipticity of Electric Field in InSb [Other parameters of InSb (T=289°) are listed in Table 8-1].

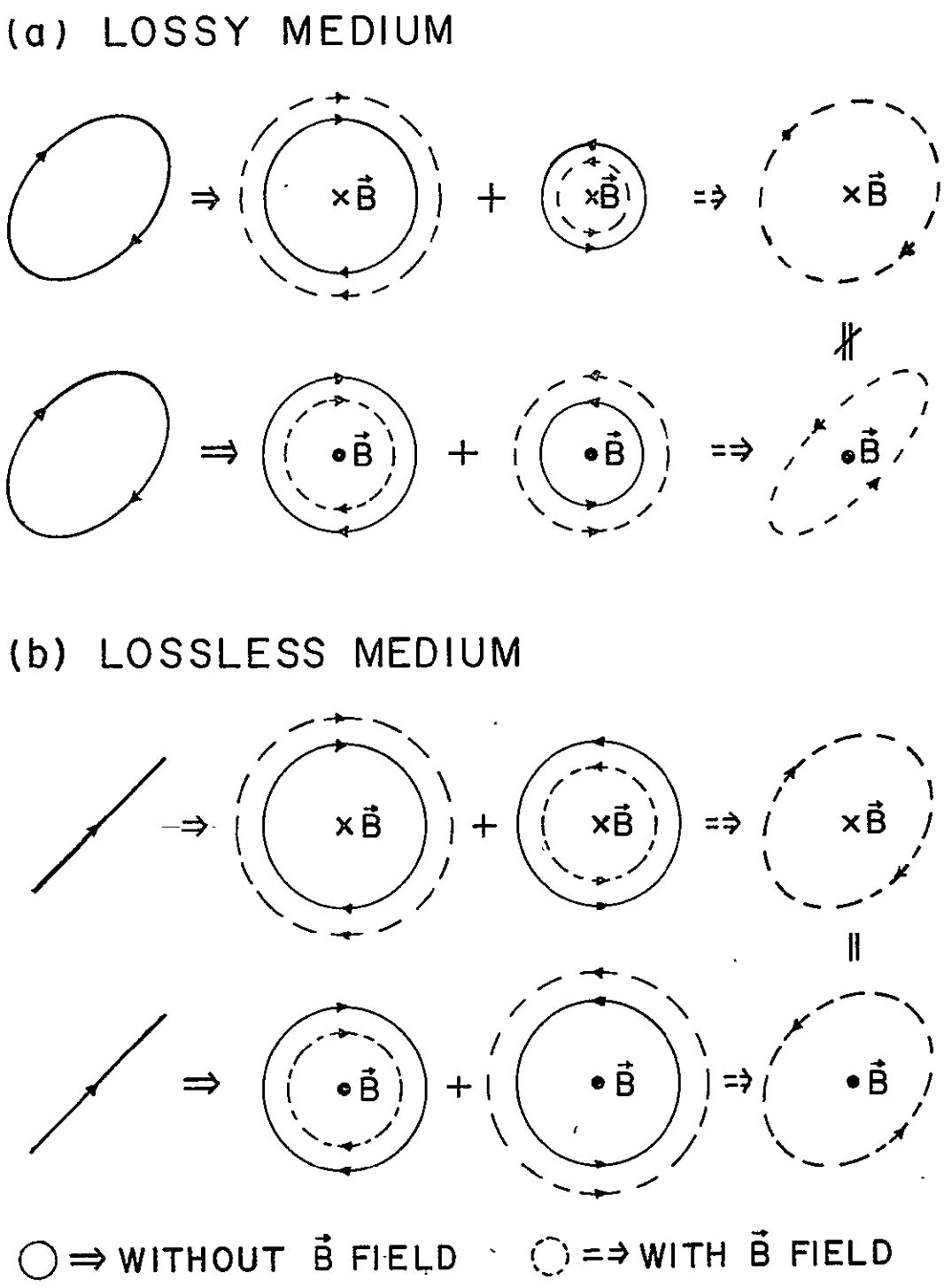


Fig. 10-3. Pictorial Explanation for Non-reciprocal Reflection.

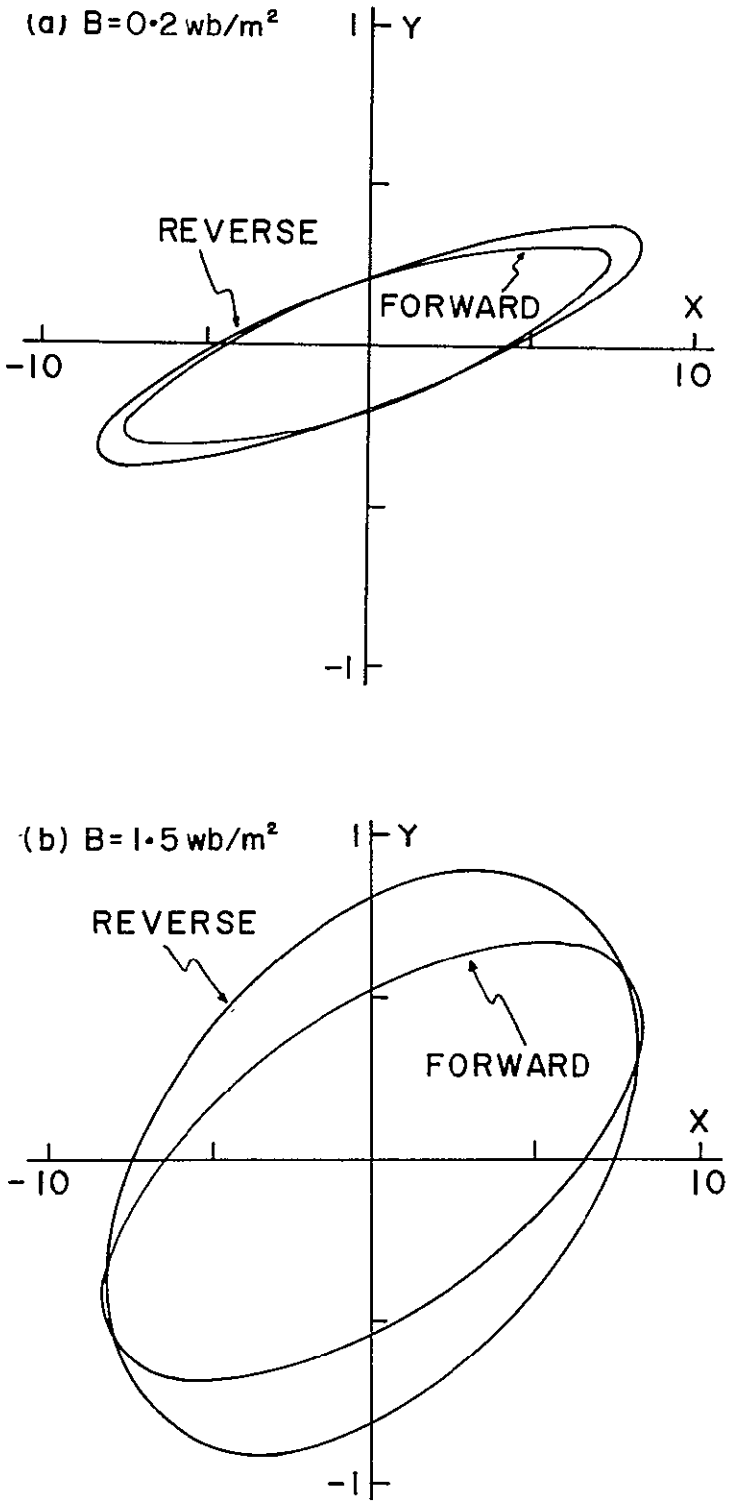


Fig. 10-4. Orbits of Electrons in the InSb with Reversal of dc Magnetic Field [Parameters of InSb (T=284°K) are listed in Table 8-1. Geometry considered is shown in Fig. 7-1a with θ=50°].

of electrons in a magnetoplasma with the dc magnetic field of 15 kG when non-reciprocity is quite large. Fig. [10-4b] indicates large change in electron orbits with reversal of the dc magnetic field,and therefore large non-reciprocal reflection is observed.

The explanation based on changes in electron orbits with reversal of the magnetic field also explains why collisions must be present; if not, the reversal of the direction of propagation does not change the magnitude of the reflection coefficient but only its phase. Also if the collision rate is too high, only small non-reciprocal reflection takes place. The orbit of electrons in a collision-less medium or in a semiconductor with a small mobility is almost linear, as already shown in Fig. [10-2], (note difference in x and y scales). This linear polarization can be decomposed in right and left circular polarizations with equal radii. Application of a dc magnetic field causes one polarization to increase in magnitude and the other to decrease, and hence the polarization becomes elliptic. Reversing the field causes the whole process to reverse, but elliptic orbits of an electron for two directions of the dc magnetic field are identical. Therefore no non-reciprocal reflection is expected, but there is a change in phase, as already shown in Fig. [10-3b].

From the discussions given above, it appears that a maximum difference in a reflection from a magneto-plasma with reversal of the dc magnetic field would take place if the orbit of electrons with B=0 is nearly circular. Of course, it cannot be completely circular because of loss in the plasma as shown in Fig. [10-2]. Fig. [10-5a] shows that the orbit of electrons in the InSb with a low motility of 50 $cm^2$/V-sec, where the reflection is found to be nearly reciprocal, is almost linear. On the other hand, Fig. [10-5b] shows that the orbit of electrons in the InSb with a much higher mobility of 7 $10^4 cm^2$/V-sec, where an isolation of 1 db is observed with B=15kG at an incident angle of 60°, is elliptic. The isolation given above is quite small because only the simplest case, reflection from the interface between free space and InSb, was considered. Large isolation was, however, observed in the reflection from the interface between free space and dielectric coated InSb as given in Section 9-2.

Thus, let us investigate the eccentricity ε of the orbit of electrons with B=0. (Recall that ε=1 for a straight line, ε<1 for an ellipse and ε=0 for a circle). For our case the eccentricity ε is given by

$$\varepsilon = \left[ 1 - \frac{-M^2+1+\frac{4M^2\cos^2\psi}{1-M^2} + (1+M^2)\sqrt{\left(\frac{2M\cdot\cos\psi}{1-M^2}\right)^2+1}}{M^2-1-\frac{4M^2\cos^2\psi}{1-M^2} + (1+M^2)\sqrt{\left(\frac{2M\cdot\cos\psi}{1-M^2}\right)^2+1}} \right]^{\frac{1}{2}}, \quad (10\text{-}3)$$

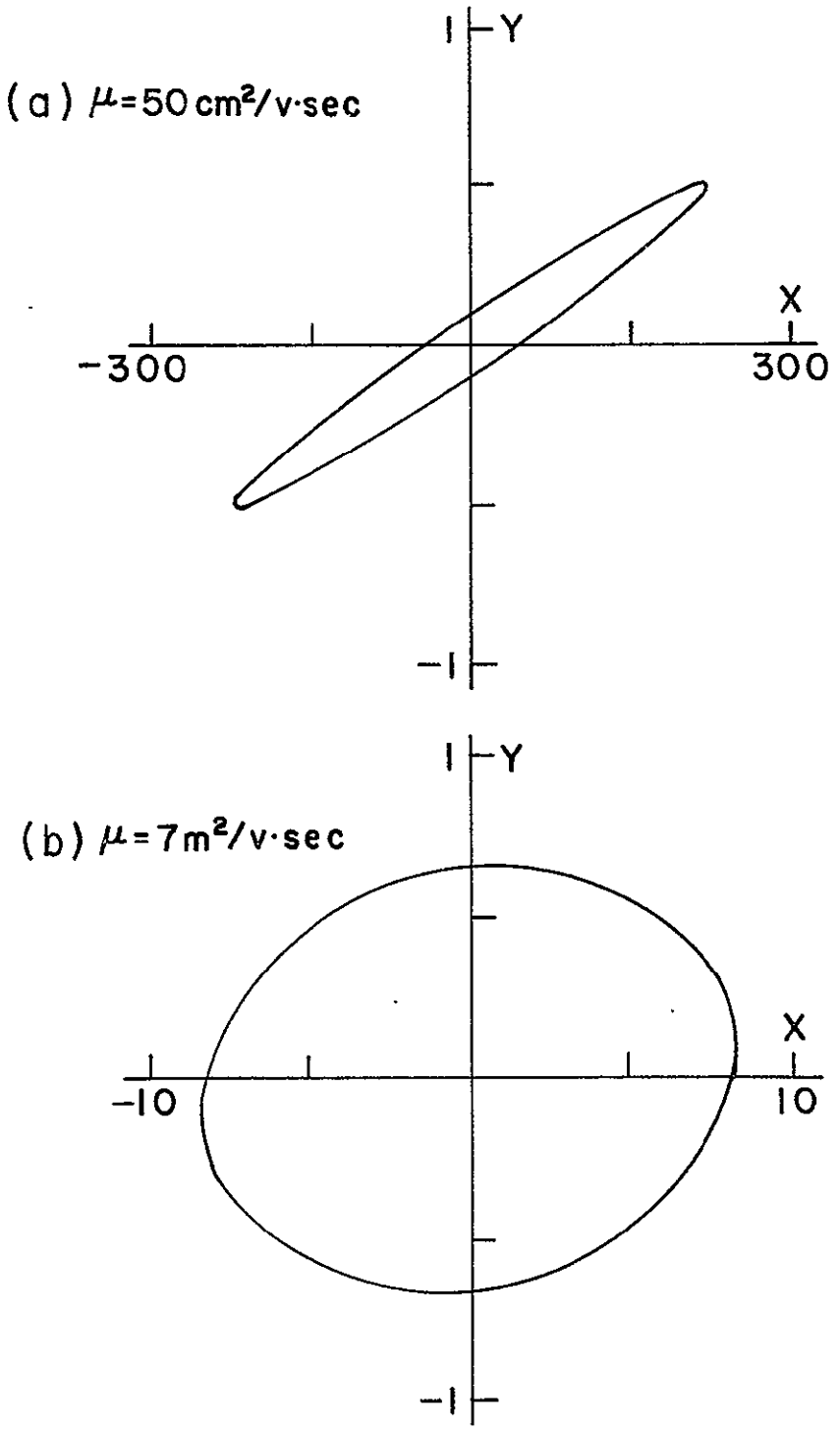


Fig. 10-5. Change in Electron Orbits in InSb with no Magnetic Field for Different Mobilities [Other parameters of InSb (T=284°) are listed in Table 8-1. Geometry considered is shown in Fig. 7-1a with θ=50° and B=0].

where

$$M = \frac{\sin\theta}{\left[\left(K_L - \sin^2\theta - \frac{\omega_p^2}{\omega^2+\nu^2}\right)^2 + \left\{\frac{\omega_p^2\nu}{\omega(\omega^2+\nu^2)}\right\}^2\right]^{1/4}}, \qquad (10\text{-}4)$$

and

$$\psi = -\frac{1}{2}\tan^{-1}\frac{\dfrac{\omega_p^2\nu}{\omega(\omega^2+\nu^2)}}{K_L - \sin^2\theta - \dfrac{\omega_p^2}{\omega^2+\nu^2}} + \pi \; . \qquad (10\text{-}5)$$

The eccentricity $\varepsilon$ as a function of incident angle $\theta$ is shown in Fig. [10-6] for several boundary conditions. Since the eccentricity decreases, i.e. the orbit of electrons in a plasma becomes more circular, with increasing incident angle, it is expected that the difference in reflection from a magnetoplasma with reversal of the dc magnetic field should increase with incident angle. However, at large incident angles (over 85°) the reflection is quite large and hence only a small em wave is transmitted in a plasma. Thus the change in reflection with reversal of the dc magnetic field decreases at large incident angles simply because the wave does not interact much with the plasma. It is also found that the eccentricities of the orbits of electrons for the cases of dielectric-plasma and free space-dielectric coated plasma

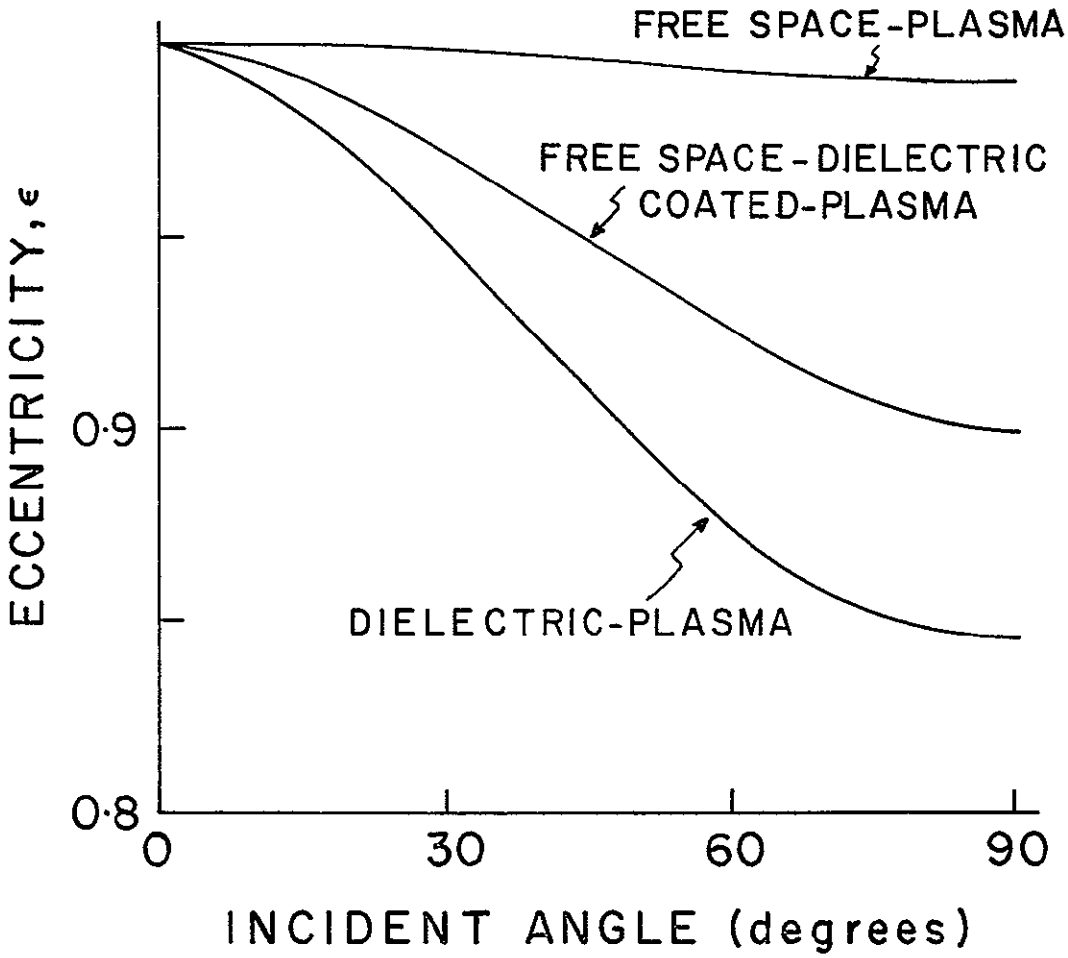


Fig. 10-6. Eccentricity ε of Electron Orbits in InSb as a Function of Incident Angle [Parameters of InSb (T=284°K) are listed in Table 8-1. Geometry considered is shown in Fig. 7-1 with θ=50° and B=0].

interfaces are much smaller than that for the case of free space-plasma interface as shown in Fig. [10-6]. That is, the orbit of the electrons is much less linear, and hence greatly enhanced non-reciprocal reflection can be observed for the cases of dielectric-plasma and free space-dielectric coated plasma interfaces. Therefore, the combined effects of both collisions, which are required to have an elliptic motion of electrons in a plasma without a magnetic field, and a dc magnetic field produce non-reciprocal effects on the electron orbits when the dc magnetic field is reversed, and thus explain the non-reciprocal reflection.

It should be pointed out that, since the electric field is elliptically polarized in a lossy magneto-plasma, there is a component of the electric field along the direction of the propagation. Because of this longitudinal component, the existence of space charge might be expected. The deviation in carrier concentration from equilibrium can be calculated from the Poisson's equation and is given by

$$n' = H_o \frac{\omega \mu_o \varepsilon_o}{e} \sin\theta \, \mathrm{Im}\left[\left(\frac{1}{A} - \sin^2\theta\right)\right]^{\frac{1}{2}} \qquad (10\text{-}6)$$

This turns out to be around $10^4/cm^3$ whereas the equilibrium carrier concentration is $10^{16}/cm^3$. Therefore, the

charge neutrality condition holds. This is also confirmed from the fact that the dielectric relaxation time is on the order of $10^{-13}$ to $10^{-14}$ sec, on the other hand, the period of the phenomena that we are interested in is around $10^{-11}$ to $10^{-12}$ sec. Thus the space charge can be neglected.

## 10-2 Possible Refinements for Isolators

Large discrepancies between theoretical and experimental results take place at incident angles over 80° due to experimental difficulties as discussed in Section 9-2. Thus further considerations are made in this section in order to shift the peak of the isolation curve to a lower incident angle.

First making use of a thin dielectric layer with a dielectric constant less than unity or even with a negative dielectric constant was considered in order to have no reflection at a reasonable incident angle. Such a layer can be realized by using either a semiconductor or an artificial dielectric. For a semiconductor, the carrier concentration must be chosen so that total relative dielectric constant contributed from lattice as well as free carriers is less than unity or even negative. For the ideal case when $\tau=\infty$ and $\omega>>\omega_c$, Eq.(2-14), (2-15) and (2-16) become

$$K_{\perp} = K_{||} \cong K_L - \frac{\omega_p^2}{\omega^2} < 1 \qquad (10\text{-}7)$$

$$K_x \cong 0 \ , \qquad (10\text{-}8)$$

if the carrier concentration of the semiconductor is chosen properly. A dielectric medium whose dielectric constant is less than unity can be also realized using an artificial dielectric. The arrays of conducting rods or plates were proposed as an artificial dielectric [Harvey, 1970]. When the dielectric layer on top of the InSb has a dielectric constant of 0.697, it is possible to create the condition that no reflection takes place at a reasonable incident angle ($\theta$=60°) as shown in Fig. [10-7]. However, the peak of the isolation curve is very critical with incident angle, and hence with a carrier density and mobility, and with dc magnetic field. This sharpness of the isolation curve is essentially due to the critical impedance match which results from the large impedance difference between free space and the InSb. However, the sharpness of the isolation curve could be made broader by the use of multiple layer matching transformers. By tolerating a certain mismatch at the central incident angle, it is possible to match at N incident angles by using N matching transformers to give an even wider handwidth [Young, 1959]. It may be possible to make

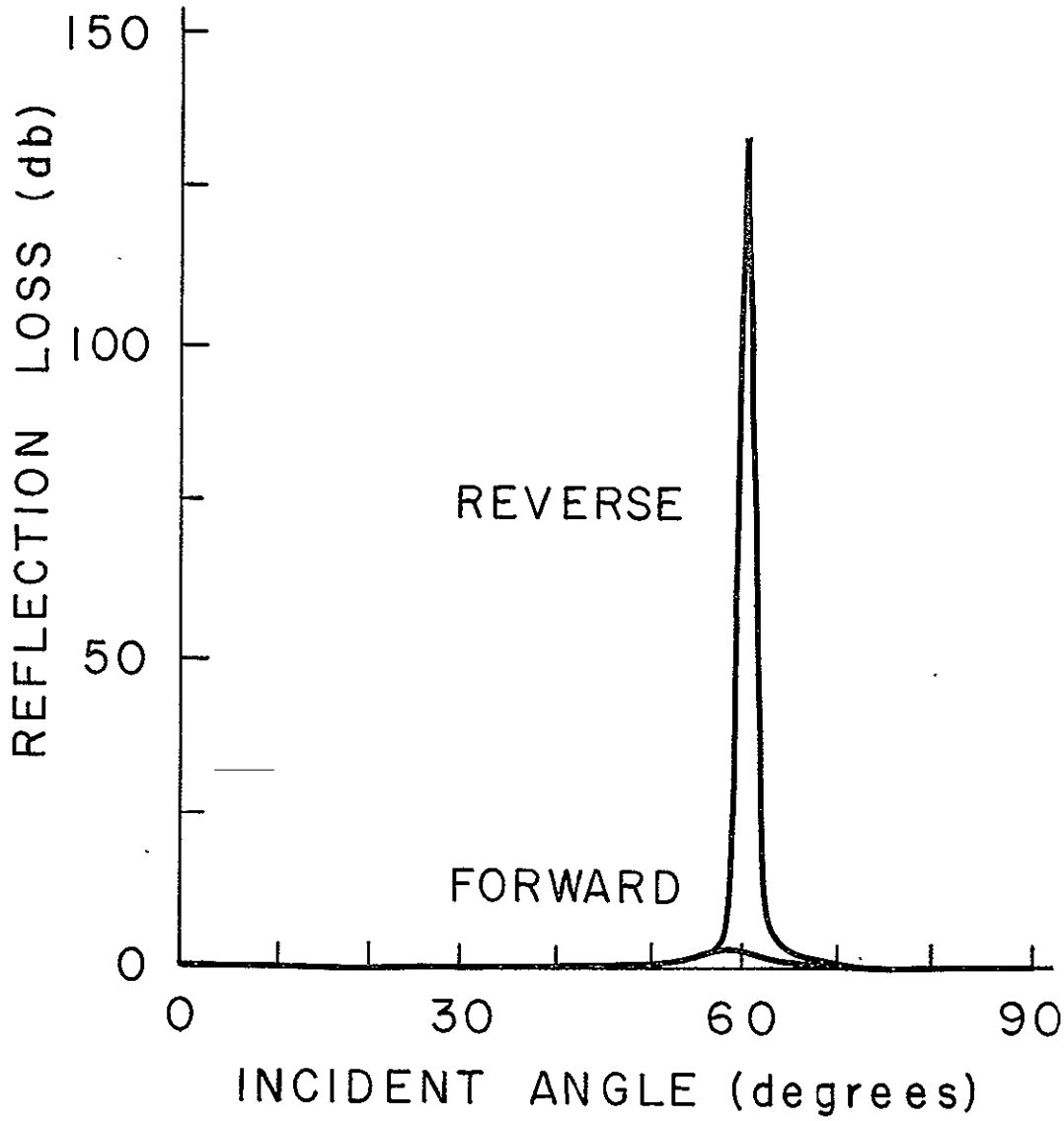


Fig. 10-7. Theoretical Reflection Loss of InSb at 337 μm as a Function of Incident Angle [Parameters of InSb (T=289°) are listed in Table 8-1. Geometry of IR Reflection Isolator is shown in Fig. 8-4 with B=16kG, $K_M$=0.697 and ℓ=276μm].

use of this sharpness of the isolation for the development of the angle resolving devices.

The utilization of Alfvén effect was also considered. The typical materials considered here are bismuth and bismuth-antimony alloy which have a relatively high mobility, and low carrier concentration for both electrons and holes. The existence of both electrons and holes with almost equal mobilities and masses requires some modifications in the calculation of the reflection coefficient. This might, in turn, help in shifting the peak of the isolation curve to a lower incident angle. It turns out, unfortunately, that the cancellation takes place in the off-diagonal component of the relative dielectric tensor, $K_x$, which plays a vital role in the non-reciprocal phenomena. Therefore the relative dielectric tensor becomes diagonal, and non-reciprocal phenomena cannot be expected.

## 10-3 Summary

The theoretical and experimental investigations reported in Part II were performed for the purpose of the development of the reflection beam isolator at millimeter and submillimeter wavelengths using non-reciprocal reflection of em waves incident on a semiconductor. The best data obtained in our experiments at 94 GHz were 12 db isolation with 11 db insertion

loss, and corresponding theoretical data were 44 db isolation with 5 db insertion loss. At a wavelength of 337 μm the experiments demonstrated 4.1 db isolation with 2 db insertion loss, whereas the theory predicts 16 db isolation with an insertion loss of less than 1 db. However, since theoretical values given above occur at very large incident angles, difficulties arose in the experiments. Otherwise, the experimental results indicated the validity of the theory in general. The theoretical result for a wavelength of 118 μm shows a very broad reflection loss curve (about 4 db) as a function of incident angle and an excellent ratio of isolation to insertion loss of about 50 in db scale as shown in Fig. [10-8]. The reverse loss can be increased by the multiple reflection. This result indicates that the development of the practical reflection beam isolator should be possible using solid state magnetoplasmas.

One of the great advantages of utilization of semiconductors in the development of non-reciprocal devices lies in the flexibility of design that comes with a wide range of semiconductor parameters. Thus it is possible to expect significant improvement of the non-reciprocal semiconductor devices as a result of continued research and development effort.

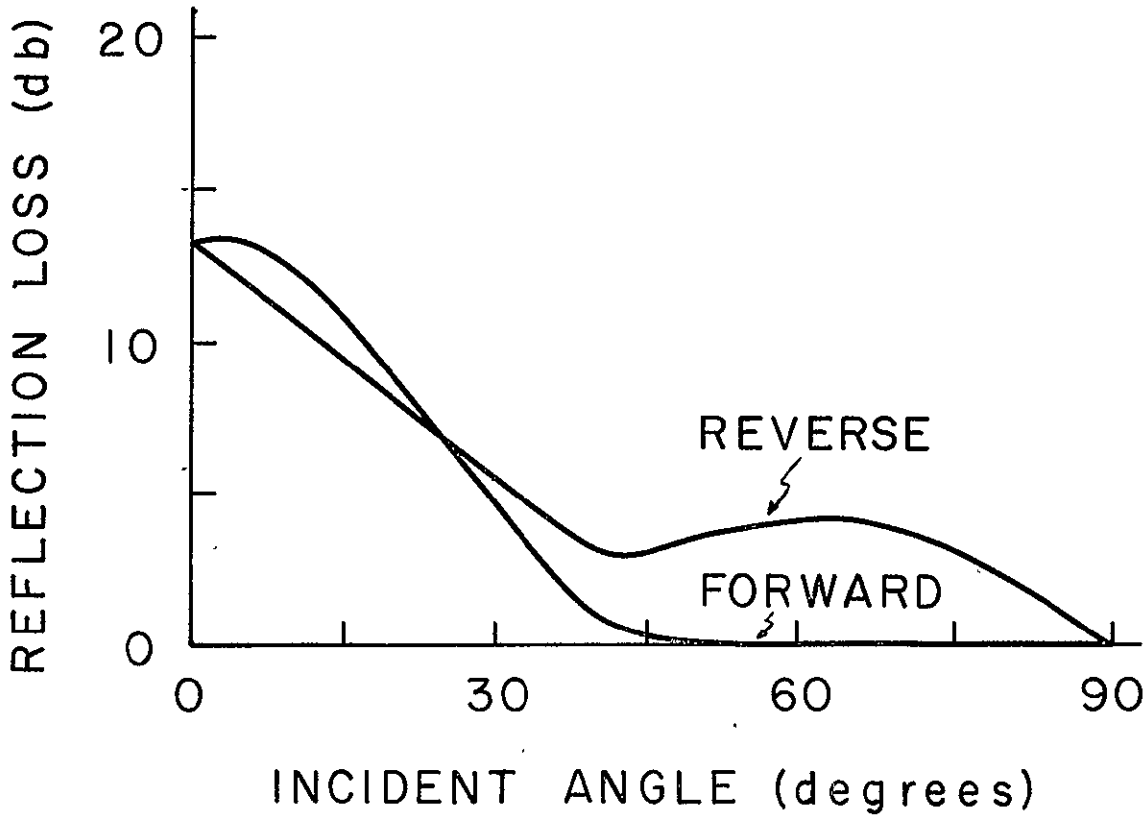


Fig. 10-8. Theoretical Reflection Loss for InSb at 118μm as a Function of Incident Angle [Parameter of InSb (T=284°K) are listed in Table 8-1. Geometry of IR Reflection Isolator is shown in Fig. 7-1b with $K_M$=50 and B=13.2kG].

## APPENDIX A. ENERGY DEPENDENCE OF RELAXATION TIME

It is known that the relaxation time is dependent on the energy of electrons. This Appendix will estimate the error caused by the assumption that the relaxation time is not dependent on the energy of electrons.

The equations given in this thesis, such as propagation constants, reflection coefficients and etc., can be expressed in terms of the elements of the relative dielectric tensor, $K_{\perp}$, $K_{\times}$ and $K_{\parallel}$. When the relaxation time is a function of energy, the Boltzmann equation must be used to derive the relative dielectric tensor. The solution of the Boltzmann equation requires the averaging of the quantities containing the relaxation time in the relative dielectric tensor with respect to energy. But otherwise, the forms of the elements of the relative dielectric tensor are the same as for the case when the relaxation time is not a function of energy. The results are

$$K_{\perp} = K_L - \frac{j\omega_p^2}{\omega} \left\langle \frac{(j\omega\tau+1)\tau}{(j\omega\tau+1)^2 + (\omega_c\tau)^2} \right\rangle , \quad \text{(A-1)}$$

$$K_{\times} = \frac{j\omega_p^2}{\omega} \left\langle \frac{\omega_c\tau^2}{(j\omega\tau+1)^2 + (\omega_c\tau)^2} \right\rangle , \quad \text{(A-2)}$$

and

$$K_{||} = K_L - \frac{j\omega_p^2}{\omega} \left\langle \frac{\tau}{j\omega\tau+1} \right\rangle \tag{A-3}$$

where <> indicates the appropriate averaging of $\tau$ with respect to energy. Since the averaging of $\tau$ in these expressions is quite complicated, we consider these in the following cases:

1. High Frequency Approximation ($\omega\tau >> 1$):

   1.1 High Field Case ($\omega_c >> \omega$):

$$K_{\perp} = K_L + \frac{\omega_p^2}{\omega_c^2} \left[1 + \frac{1}{j\omega} \left\langle \frac{1}{\tau} \right\rangle\right] \tag{A-4}$$

$$K_{\times} = - \frac{j\omega_p^2}{\omega\omega_c} \tag{A-5}$$

$$K_{||} = K_L - \frac{\omega_p^2}{\omega^2} \left[1 - \frac{1}{j\omega} \left\langle \frac{1}{\tau} \right\rangle\right] \tag{A-6}$$

   1.2 Low Field Case ($\omega >> \omega_c$):

$$K_{\perp} = K_L - \frac{\omega_p^2}{\omega^2} \left[1 - \frac{1}{j\omega} \left\langle \frac{1}{\tau} \right\rangle\right] \tag{A-7}$$

$$K_{\times} = \frac{j\omega_p^2\omega_c}{\omega^3} \left[1 - \frac{2}{j\omega} \left\langle \frac{1}{\tau} \right\rangle\right] \tag{A-8}$$

$$K_{||} = K_L - \frac{\omega_p^2}{\omega^2} \left[1 - \frac{1}{j\omega} \left\langle \frac{1}{\tau} \right\rangle\right] \tag{A-9}$$

2. Low Frequency Approximation ($\omega\tau << 1$):

2.1 High Field Case ($\omega_c >> \omega$):

$$K_{\perp} = K_L - \frac{j\omega_p^2}{\omega} \left\langle \frac{1 + j\omega\tau}{\omega_c^2 \tau} \right\rangle , \qquad \text{(A-10)}$$

$$K_x = \frac{-j\omega_p^2}{\omega\omega_c} , \qquad \text{(A-11)}$$

$$K_{||} = K_L - \frac{j\omega_p^2}{\omega} \langle \tau(1 - j\omega\tau) \rangle \qquad \text{(A-12)}$$

2.2 Low Field Case ($\omega >> \omega_c$):

$$K_{\perp} = K_{\perp} - \frac{j\omega_p^2}{\omega} \langle \tau(1 - j\omega\tau) \rangle \qquad \text{(A-13)}$$

$$K_x = - \frac{j\omega_p^2}{\omega} \langle \omega_c \tau^2 (1 - 2j\omega\tau) \rangle \qquad \text{(A-14)}$$

$$K_{||} = K_L - \frac{j\omega_p^2}{\omega} \langle \tau(1 - j\omega\tau) \rangle \qquad \text{(A-15)}$$

Since in our experiments, the value of $\omega\tau$ was greater than unity ($\omega\tau \sim 4$), for the first order approximation, the values of $K_{\perp}$, $K_x$ and $K_{||}$ for the case of $\omega\tau >> 1$ can be used in the development of the theories. If the relaxation time $\tau$ is isotropic, then $\tau$ may be expressed as a function of energy $\varepsilon$, rather than as a function of the wave vector $\vec{k}$. For the non-degenerate

case, the average value of the reciprocal of the relaxation $\tau$, which occurs in the formula of K's are then evaluated by

$$\left\langle \frac{1}{\tau} \right\rangle = \frac{\int_0^\infty \frac{1}{\tau} \varepsilon^{3/2} e^{-\frac{\varepsilon}{kT}} d\varepsilon}{\int_0^\infty \varepsilon^{3/2} e^{-\frac{\varepsilon}{kT}} d\varepsilon} \quad . \tag{A-16}$$

When the energy dependence of $\tau$ is assumed to be $\tau = a\varepsilon^{-S}$, then

$$\langle \tau \rangle \left\langle \frac{1}{\tau} \right\rangle = \frac{\Gamma(\frac{5}{2} - S)\Gamma(\frac{5}{2} + S)}{[\Gamma(\frac{5}{2})]^2} \quad . \tag{A-17}$$

For the acoustic scattering where $S = \frac{1}{2}$,

$$\langle \tau \rangle \left\langle \frac{1}{\tau} \right\rangle \Big|_{S=\frac{1}{2}} = \frac{32}{9\pi} = 1.13 \quad , \tag{A-18}$$

and for the ionized impurity scattering where $S = -\frac{3}{2}$,

$$\langle \tau \rangle \left\langle \frac{1}{\tau} \right\rangle \Big|_{S=-\frac{3}{2}} = \frac{32}{3\pi} = 3.38 \quad . \tag{A-19}$$

In the case of polar scattering, the average of $\langle \tau \rangle \langle \frac{1}{\tau} \rangle$ has not been calculated. Judging from the temperature dependence of the mobility of free carriers for n-type InSb and n-type GaAs at room temperature, the acoustic

scattering is probably dominant. Thus the maximum error caused by using $\langle\tau\rangle$ should be 13% from Eq.(A-18).

## APPENDIX B. CHARACTERISTIC EQUATION FOR CIRCULAR WAVEGUIDE CONTAINING ANNULAR PLASMA COLUMN

Appendix B outlines the boundary value problem that results from the configuration shown in Fig.(3-1).

In the region r<a, the wave equations describing the longitudinal components of em waves are

$$\nabla_T^2 E_z^o + q^2 E_z^o = 0 \qquad \text{(B-1)}$$

$$\nabla_T H_z^o + q^2 H_z^o = 0 \qquad \text{(B-2)}$$

The appropriate solutions for the longitudinal field components for r<a are

$$E_z^o = U J_m(qr)\, e^{jm\phi - \Gamma z} \qquad \text{(B-3)}$$

and

$$H_z^o = V J_m(qr)\, e^{jm\phi - \Gamma z} \qquad \text{(B-4)}$$

where U and $\overline{V}$ are arbitrary, complex constants. Corresponding transverse components of em waves are calculated from the equations:

$$\vec{E}_T^o = (-\Gamma/q^2)\nabla_T E_z + (j\omega\mu_o/q^2)(\vec{a}_z \times \nabla_T H_z) \qquad \text{(B-5)}$$

$$\vec{H}_T^o = (-\Gamma/q^2)\nabla_T H_z - (j\omega\varepsilon_o/q^2)(\vec{a}_z \times \nabla_T E_z) \qquad \text{(B-6)}$$

Then the transverse E field components for r<a are

$$E_r^o = \left[ Uq\xi J_m'(qr) - Vj\zeta \frac{Z_o m}{qr} J_m(qr) \right] e^{jm\phi - \Gamma z} , \qquad \text{(B-7)}$$

$$E_\phi^o = \left[ U \frac{jm}{r} \xi J_m(qr) + V\zeta Z_o J_m'(qr) \right] e^{jm\phi - \Gamma z} . \qquad \text{(B-8)}$$

Also the transverse H field components for r<a are

$$H_r^o = \left[Uj\zeta \frac{Y_o^m}{qr} J_m(qr) + Vq\xi J_m'(qr)\right] e^{jm\phi - \Gamma z} \qquad \text{(B-9)}$$

and

$$H_\phi^o = \left[-U\zeta Y_o J_m'(qr) + V\frac{jm}{r}\xi J_m(qr)\right] e^{jm\phi - \Gamma z} \qquad \text{(B-10)}$$

In the region of the annular plasma column a<r<b, Maxwell's equations yield the coupled wave equations:

$$\nabla_T^2 E_z + aE_z = bH_z \qquad \text{(B-11)}$$

$$\nabla_T^2 H_z + cH_z = dE_z \qquad \text{(B-12)}$$

This coupled set of second-order equations can be transformed into uncoupled set of fourth-order equations:

$$\left[\nabla_T^4 + (a+c)\nabla_T^2 + (ac-bd)\right] E_z = 0 \qquad \text{(B-13)}$$

$$\left[\nabla_T^4 + (a+c)\nabla_T^2 + (ac-bd)\right] H_z = 0 \qquad \text{(B-14)}$$

Assuming the solutions of the form $\exp(-jp\cdot r_T)$, the dispersion equation becomes

$$p^4 - (a+c)p^2 + (ac-bd) = 0 \ . \qquad \text{(B-15)}$$

Then the wave equation describing the transverse components of em waves is given by

$$(\nabla_T^2 + p_i^2) E_{zi} = 0 \ . \qquad \text{(B-16)}$$

The longitudinal field components inside the annular plasma (a<r<b) are

$$E_z = E_{z1} + E_{z2}$$

$$= \left[AJ_m(p_1 r) + BN_m(p_1 r) + CJ_m(p_2 r) + DN_m(p_2 r)\right] e^{jm\phi - \Gamma z}, \qquad \text{(B-17)}$$

and

$$H_z = h_1 E_{z1} + h_2 E_{z2}$$

$$= \left[ A h_1 J_m(p_1 r) + B h_1 N_m(p_1 r) + C h_2 J_m(p_2 r) + D h_2 N_m(p_2 r) \right] e^{jm\phi - \Gamma z} . \tag{B-18}$$

where A, B, C and D are arbitrary, complex constants.

Using

$$\begin{vmatrix} \vec{E}_T \\ \vec{H}_T \end{vmatrix} = \begin{vmatrix} -1/\Gamma & R/b & -K_\perp/\Gamma K_x & S/b \\ \Gamma/b & P/b & 0 & Q/b \end{vmatrix}$$

$$\cdot \begin{vmatrix} \begin{vmatrix} \nabla_T \\ p_2^2 \nabla_T \end{vmatrix} E_{z1} + \begin{vmatrix} \nabla_T \\ p_1^2 \nabla_T \end{vmatrix} E_{z2} \\ \begin{vmatrix} \vec{a}_z \times \nabla_T \\ p_2^2 \vec{a}_z \times \nabla_T \end{vmatrix} + \begin{vmatrix} \vec{a}_z \times \nabla_T \\ p_1^2 \vec{a}_z \times \nabla_T \end{vmatrix} \end{vmatrix} , \tag{B-19}$$

the transverse E field component inside the annular plasma column (a<r<b) are

$$E_r = \Big[ A \Big\{ -\frac{jm}{r} L_2 J_m(p_1 r) + \ell_2 p_1 J_m'(p_1 r) \Big\} + B \Big\{ -\frac{jm}{r} L_2 N_m(p_1 r) + \ell_2 p_1 N_m'(p_1 r) \Big\} + C \Big\{ -\frac{jm}{r} L_1 J_m(p_2 r) + \ell_1 p_2 J_m'(p_2 r) \Big\} + D \Big\{ -\frac{jm}{r} L_1 N_m(p_2 r) + \ell_1 p_2 N_m'(p_2 r) \Big\} \Big] e^{jm\phi - \Gamma z} , \tag{B-20}$$

and

$$E_\phi = \left[A\left\{\frac{jm}{r}\ell_2 J_m(p_1 r) + L_2 p_1 J_m'(p_1 r)\right\} + B\left\{\frac{jm}{r}\ell_2 N_m(p_1 r)\right.\right.$$
$$\left. + L_2 p_1 N_m'(p_1 r)\right\} + C\left\{\frac{jm}{r}\ell_1 J_m(p_2 r) + L_1 p_2 J_m'(p_2 r)\right\}$$
$$\left. + D\left\{\frac{jm}{r}\ell_1 N_m(p_2 r) + L_1 p_2 N_m'(p_2 r)\right\}\right] e^{jm\phi - \Gamma z} . \qquad \text{(B-21)}$$

For the transverse H field components:

$$H_r = \left[A\left\{-\frac{jm}{r}Y_2 J_m(p_1 r) + Y_2 p_1 J_m'(p_1 r)\right\} + B\left\{-\frac{jm}{r}Y_2 N_m(p_1 r)\right.\right.$$
$$\left. + Y_2 p_1 N_m'(p_1 r)\right\} + C\left\{-\frac{jm}{r}Y_1 J_m(p_2 r) + Y_1 p_2 J_m'(p_2 r)\right\}$$
$$\left. + D\left\{-\frac{jm}{r}Y_1 N_m(p_2 r) + Y_1 p_2 N_m'(p_2 r)\right\}\right] e^{jm\phi - \Gamma z} , \qquad \text{(B-22)}$$

and

$$H_\phi = \left[A\left\{\frac{jm}{r}Y_2 J_m(p_1 r) + Y_2 p_1 J_m'(p_1 r)\right\} + B\left\{\frac{jm}{r}Y_2 N_m(p_1 r)\right.\right.$$
$$\left. + Y_2 p_1 N_m'(p_1 r)\right\} + C\left\{\frac{jm}{r}Y_1 J_m(p_2 r) + Y_1 p_2 J_m'(p_2 r)\right\}$$
$$\left. + D\left\{\frac{jm}{r}Y_1 N_m(p_2 r) + Y_1 p_2 N_m'(p_2 r)\right\}\right] e^{jm\phi - \Gamma z} , \qquad \text{(B-23)}$$

Now the boundary conditions at the plasma surface (r=a) shall be taken as the continuity of the tangential E and H fields:

$$AJ_m(p_1 a) + BN_m(p_1 a) + CJ_m(p_2 a) + DN_m(p_2 a) = UJ_m(qa), \qquad \text{(B-24)}$$

$$Ah_1 J_m(p_1 a) + Bh_1 N_m(p_1 a) + Ch_2 J_m(p_1 a) + Dh_2 N_m(p_2 a) = VJ_m(qa), \qquad \text{(B-25)}$$

$$A\left\{\frac{jm}{a}\ell_2 J_m(p_1a) + L_2p_1J_m'(p_1a)\right\} + B\left\{\frac{jm}{a}\ell_2 N_m(p_1a) + L_2p_1N_m'(p_1a)\right\}$$

$$+ C\left\{\frac{jm}{a}\ell_1 J_m(p_2a) + L_1p_2J_m'(p_2a)\right\} + D\left\{\frac{jm}{a}\ell_1 N_m(p_2a) + L_1p_2N_m'(p_2a)\right\}$$

$$= U\frac{jm}{a}\xi J_m(qa) + V\zeta Z_o J_m'(qa) \quad , \qquad \text{(B-26)}$$

$$A\left\{\frac{jm}{a}Y_2 J_m(p_1a) + Y_2p_1J_m'(p_1a)\right\} + B\left\{\frac{jm}{a}Y_2 N_m(p_1a) + Y_2p_1N_m'(p_1a)\right\}$$

$$+ C\left\{\frac{jm}{a}Y_1 J_m(p_2a) + Y_1p_2J_m'(p_2a)\right\} + D\left\{\frac{jm}{a}Y_1 N_m(p_2a) + Y_1p_2N_m'(p_2a)\right\}$$

$$= -U\zeta Y_o J_m'(qa) + V\frac{jm}{a}\xi J_m(qa) \quad . \qquad \text{(B-27)}$$

Also at the boundary of the perfect conductor waveguide wall (r=b),

$$AJ_m(p_1b) + BN_m(p_1b) + CJ_m(p_2b) + DN_m(p_2b) = 0 \quad , \qquad \text{(B-28)}$$

$$A\left\{\frac{jm}{b}\ell_2 J_m(p_1b) + L_2P_1J_m'(p_1b)\right\} + B\left\{\frac{jm}{b}\ell_2 N_m(p_1b)\right.$$

$$\left. + L_2P_1N_m'(p_1b)\right\} + C\left\{\frac{jm}{b}\ell_1 J_m(p_2b) + L_1P_2J_m'(p_2b)\right\}$$

$$+ D\left\{\frac{jm}{b}\ell_1 N_m(p_2b) + L_1P_2N_m'(p_2b)\right\} = 0 \quad . \qquad \text{(B-29)}$$

In order to have non-trivial solutions of A, B, C, D, U and V, the 6×6 determinant of these coefficients must be zero:

$$
\begin{vmatrix}
J_m(p_1 b) & N_m(p_1 b) & J_m(p_2 b) & N_m(p_2 b) & 0 & 0 \\
S_1(p_1 b) & S_2(p_1 b) & S_3(p_2 b) & S_4(p_2 b) & 0 & 0 \\
J_m(p_1 a) & N_m(p_1 a) & J_m(p_2 a) & N_m(p_2 a) & -J_m(qa) & 0 \\
h_1 J_m(p_1 a) & h_1 N_m(p_1 a) & h_2 J_m(p_2 a) & h_2 N_m(p_2 a) & 0 & -J_m(qa) \\
S_1(p_1 a) & S_2(p_1 a) & S_3(p_2 a) & S_4(p_2 a) & -\frac{jm}{a}\xi J_m(qa) & -\zeta Z_o J_m'(qa) \\
T_1(p_1 a) & T_2(p_1 a) & T_3(p_2 a) & T_4(p_2 a) & \zeta Y_o J_m'(qa) & -\frac{jm}{a}\xi J_m(qa)
\end{vmatrix} = 0 \quad . \qquad \text{(B-30)}
$$

## APPENDIX C. MATCHING FIELDS AT AIR-PLASMA INTERFACE

Let us consider the configuration shown in Fig.(3-1) when the incident wave is $TE_{11}$.

Region 1

All components of E field in region 1 are

$$E_z = 0 + \sum_n -R^M_{n1} J_m(q^M_n r) e^{jm\phi+\Gamma^M_n z}, \qquad (C\text{-}1)$$

$$E_\phi = \zeta Z_o J'_m(q^E_1 r) e^{jm\phi-\Gamma^E_1 z} + \sum_n \Big[ -R^M_{n1} [\frac{jm}{r}\xi J_m(q^M_n r)] \cdot e^{jm\phi+\Gamma^M_n z} + [R^E_{n1}\zeta Z_o J'_m(q^E_n r)] e^{jm\phi+\Gamma^E_n z} \Big], \qquad (C\text{-}2)$$

and

$$E_r = -j\zeta \frac{Z_o m}{q^E_1 r} J_m(q^E_1 r) e^{jm\phi-\Gamma^E_1 z} + \sum_n \Big[ -R^M_{n1} [q^M_n \xi J'_m(q^M_n r)] \cdot e^{jm\phi+\Gamma^M_n z} - [R^E_{n1} j\zeta \frac{Z_o m}{q^E_n r} J_m(q^E_n r)] e^{jm\phi+\Gamma^E_n z} \Big]. \qquad (C\text{-}3)$$

Similarly all components of H field in region 1 is

$$H_z = J_m(q^E_1 r) e^{jm\phi-\Gamma^E_1 z} + \sum_n -R^E_{n1} J_m(q^E_n r) e^{jm\phi+\Gamma^E_n z}, \qquad (C\text{-}4)$$

$$H_\phi = \frac{jm}{r}\xi J_m(q_1^E r)\, e^{jm\phi-\Gamma_1^E z} + \sum_n \Big[ R_{n1}^M \; [-\zeta Y_o J_m'(q_n^M r)] \cdot e^{jm\phi+\Gamma_n^M z} + [-R_{n1}^E \; \frac{jm}{r}\, \xi J_m(q_n^E r)]\, e^{jm\phi+\Gamma_n^E z} \Big] \quad , \qquad (C\text{-}5)$$

and

$$H_r = q_1^E \xi J_m'(q_1^E r)\, e^{jm\phi-\Gamma_1^E z} + \sum_n \Big[ R_{n1}^M \; [j\xi \frac{Y_o m}{q_n^M r} J_m(q_n^M r)] \cdot e^{jm\phi-\Gamma_n^M z} + [-R_{n1}^E q_n^E \xi J_m'(q_n^E r)]\, e^{jm\phi+\Gamma_n^E z} \Big] \quad . \qquad (C\text{-}6)$$

Here the propagation constant, $\Gamma_n^E$, is determined from the characteristic equation of TE wave, i.e.,

$$J_m'(q_n^E b) = 0 \quad , \qquad (C\text{-}7)$$

where

$$q_n^{E\,2} = \Gamma_n^{E\,2} + k_o^{\,2} \quad . \qquad (C\text{-}8)$$

Also the propagation constant, $\Gamma_n^M$, is determined from the characteristic equation of TM waves, i.e.,

$$J_m(q_n^M b) = 0 \quad , \qquad (C\text{-}9)$$

when

$$q_n^{M\,2} = \Gamma_n^{M\,2} + k_o^{\,2} \quad . \qquad (C\text{-}10)$$

Region 2

A: In the plasma a<r<b, all components of F field in the plasma region are

$$E_z = \sum_n T_{n2}\Big[A_n J_m(p_1 r) + B_n N_m(p_1 r) + C_n J_m(p_2 r) + D_n N_m(p_2 r)\Big] e^{jm\phi - \Gamma_n z} + \sum_n R_{n2}\Big[A_n J_m(p_1 r) + B_n N_m(p_1 r) + C_n J_m(p_2 r) + D_n N_m(p_2 r)\Big] e^{jm\phi + \Gamma_n z}, \quad \text{(C-11)}$$

$$E_\phi = \sum_n T_{n2}\Big[A_n\{\frac{jm}{r}\ell_2^t J_m(p_1 r) + L_2^t P_1 J_m'(p_1 r)\} + B_n\{\frac{jm}{r}\ell_2^t N_m(p_1 r) + L_2^t p_1 N_m'(p_1 r)\} + C_n\{\frac{jm}{r}\ell_1^t J_m(p_2 r) + L_1^t p_2 J_m'(p_2 r)\} + D_n\{\frac{jm}{r}\ell_1^t N_m(p_2 r) + L_1^t p_2 N_m'(p_2 r)\}\Big] \cdot e^{jm\phi - \Gamma_n z} + \sum_n R_{n2}\Big[A_n\{\frac{jm}{r}\ell_2^r J_m(p_1 r) + L_2^r p_1 J_m'(p_1 r)\} + B_n\{\frac{jm}{r}\ell_2^r N_m(p_1 r) + L_2^r p_1 N_m'(p_1 r)\} + C_n\{\frac{jm}{r}\ell_1^r J_m(p_2 r) + L_1^r p_2 J_m'(p_2 r)\} + D_n\{\frac{jm}{r}\ell_1^r N_m(p_2 r) + L_1^r p_2 N_m'(p_2 r)\}\Big] e^{jm\phi + \Gamma_n z}, \quad \text{(C-12)}$$

and

$$E_r = \sum_n T_{n2}\Big[A_n\{-\frac{jm}{r} L_2^t J_m(p_1r) + \ell_2^t p_1 J_m'(p_1r)$$

$$+ B_n\{-\frac{jm}{r} L_2^t N_m(p_1r) + \ell_2^t p_1 N_m'(p_1r)$$

$$+ C_n\{-\frac{jm}{r} L_1^t J_m(p_2r) + \ell_1^t p_2 J_m'(p_2r)\}$$

$$+ D_n\{-\frac{jm}{r} L_1^t N_m(p_2r) + \ell_1^t p_2 N_m'(p_2r)\}\Big]$$

$$e^{jm\phi-\Gamma_n z} + \sum_n R_{n2}\Big[A_n\{-\frac{jm}{r} L_2^r J_m(p_1r)$$

$$+ \ell_2^r p_1 J_m'(p_1r) + B_n\{-\frac{jm}{r} L_2^r N_m(p_1r)$$

$$+ \ell_2^r p_1 N_m'(p_1r)\} + C_n\{-\frac{jm}{r} L_1^r J_m(p_2r)$$

$$+ \ell_1^r p_2 J_m'(p_2r)\} + D_n\{-\frac{jm}{r} L_1^r N_m(p_2r)$$

$$+ \ell_1^r p_2 N_m'(p_2r)\Big] e^{jm\phi+\Gamma_n z} \quad . \qquad \text{(C-13)}$$

Similarly all components of H field in the plasma region are

$$H_z = \sum T_{n2}\Big[A_n h_1^t J_m(p_1 r) + B_n h_1^t N_m(p_1 r) + C_n h_2^t J_m(p_2 r) + D_n h_2^t N_m(p_2 r)\Big] e^{jm\phi - \Gamma_n z} + \sum R_{n2}\Big[A_n h_1^r J_m(p_1 r) + B_n h_1^r N_m(p_1 r) + C_n h_2^r J_m(p_2 r) + D_n h_2^r N_m(p_2 r)\Big] e^{jm\phi + \Gamma_n z}, \quad \text{(C-14)}$$

$$H_\phi = \sum_n T_{n2}\Big[A_n\{\frac{jm}{r} Y_2^t J_m(p_1 r) + Y_2^t p_1 J_m'(p_1 r)\} + B_n\{\frac{jm}{r} Y_2^t N_m(p_1 r) + Y_2^t p_1 N_m'(p_1 r)\} + C_n\{\frac{jm}{r} Y_1^t J_m(p_2 r) + Y_1^t p_2 J_m'(p_2 r)\} + D_n\{\frac{jm}{r} Y_1^t N_m(p_2 r) + Y_1^t p_2 N_m'(p_2 r)\}\Big] \cdot e^{jm\phi - \Gamma_n z} + \sum_n R_{n2}\Big[A_n\{\frac{jm}{r} Y_2^r J_m(p_1 r) + Y_2^r p_1 J_m'(p_1 r)\} + B_n\{\frac{jm}{r} Y_2^r N_m(p_1 r) + Y_2^r p_1 N_m'(p_1 r)\} + C_n\{\frac{jm}{r} Y_1^r J_m(p_2 r) + Y_1^r p_2 J_m'(p_2 r)\} + D_n\{\frac{jm}{r} Y_1^r N_m(p_2 r) + Y_1^r p_2 N_m'(p_2 r)\}\Big] e^{jm\phi + \Gamma_n z}, \quad \text{(C-15)}$$

and

$$H_r = \sum_n T_{n2}\Big[A_n\{-\frac{jm}{r} Y_2^t J_m(p_1 r) + Y_2^t p_1 J_m'(p_1 r)\}$$

$$+ B_n\{-\frac{jm}{r} Y_2^t N_m(p_1 r) + Y_2^t p_1 N_m'(p_1 r)\}$$

$$+ C_n\{-\frac{jm}{r} Y_1^t J_m(p_2 r) + Y_1^t p_2 J_m'(p_2 r)\}$$

$$+ D_n\{-\frac{jm}{r} Y_1^t N_m(p_2 r) + Y_1^t p_2 N_m'(p_2 r)\}\Big]$$

$$e^{jm\phi - \Gamma_n z} + \sum_n R_{n2}\Big[A_n\{-\frac{jm}{r} Y_2^r J_m(p_1 r)$$

$$+ Y_2^r p_1 J_m'(p_1 r)\} + B_n\{-\frac{jm}{r} Y_2^r N_m(p_1 r)$$

$$+ Y_2^r p_1 N_m'(p_1 r)\} + C_n\{-\frac{jm}{r} Y_1^r J_m(p_2 r)$$

$$+ Y_1^r p_2 J_m'(p_2 r)\} + D_n\{-\frac{jm}{r} Y_1^r N_m(p_2 r)$$

$$+ Y_1^r p_2 N_m'(p_2 r)\}\Big] e^{jm\phi + \Gamma_n z} . \qquad \text{(C-16)}$$

B: In the center section ($o<r<a$) all of the components of E fields are

$$E_z = \sum_n T_{n2} U_n J_m(q_n r) e^{jm\phi - \Gamma_n z} + \sum_n -R_{n2} V_n J_m(q_n r) e^{jm\phi + \Gamma_n z} ,$$

(C-17)

$$E_\phi = \sum_n T_{n2}[U_n \frac{jm}{r}\xi J_m(q_n r) + V_n \zeta Z_o J'_m(q_n r)]e^{jm\phi-\Gamma_n z}$$

$$+ \sum_n R_{n2}[-U_n \frac{jm}{r}\xi J_m(q_n r) + V_n \zeta Z_o J'_m(q_n r)]e^{jm\phi+\Gamma_n z}, \quad (C-18)$$

and

$$E_r = \sum_n T_{n2}[U_n q_n \xi J'_m(q_n r) - V_n j\zeta \frac{Z_o m}{q_n r} J_m(q_n r)]$$

$$\cdot e^{jm\phi-\Gamma_n z} + \sum_n R_{n2}[-U_n q_n \xi J'_m(q_n r) - V_n j\zeta \frac{Z_o m}{q_n r}$$

$$\cdot J_m(q_n r)]e^{jm\phi+\Gamma_n z}. \quad (C-19)$$

Similarly all components of H field in the center section are

$$H_z = \sum_n T_{n2} V_n J_m(q_n r) e^{jm\phi-\Gamma_n z} + \sum_n -R_{n2} V_n J_m(q_n r) e^{jm\phi+\Gamma_n z}, \quad (C-20)$$

$$H_\phi = \sum_n T_{n2}[-U_n \zeta Y_o J'_m(q_n r) + V_n \frac{jm}{r}\xi J_m(q_n r)]e^{jm\phi-\Gamma_n z}$$

$$+ \sum_n R_{n2}[-U_n \zeta Y_o J'_m(q_n r) - V_n \frac{jm}{r}\xi J_m(q_n r)]e^{jm\phi+\Gamma_n z}, \quad (C-21)$$

and

$$H_r = \sum_n T_{n2}[U_n j\zeta \frac{Y_o m}{q_n r} J_m(q_n r) + V_n q_n \xi J'_m(q_n r)]e^{jm\phi-\Gamma_n z}$$

$$+ \sum_n R_n[U_n j\zeta \frac{Y_o m}{q_n r} J_m(q_n r) - V_n q_n \xi J'_m(q_n r)]e^{jm\phi+\Gamma_n z}. \quad (C-22)$$

Here the propagation constant, $\Gamma_n$, is determined from the zeros of 6×6 determinant obtained from the boundary

conditions, which is given in Appendix B.

Region 3

All components of E fields in the region 3 are

$$E_z = \sum_n T^M_{n3} J_m(q^M_n r) e^{jm\phi - \Gamma^M_n z} , \qquad \text{(C-23)}$$

$$E_\phi = \sum_n \left[ T^M_{n3} \left[ \frac{jm}{r} \xi J_m(q^M_n r) \right] e^{jm\phi - \Gamma^M_n z} + \left[ T^E_{n3} \zeta Z_o J'_m(q^E_n r) \right] e^{jm\phi - \Gamma^E_n z} \right], \qquad \text{(C-24)}$$

and

$$E_r = \sum_n \left[ T^M_{n3} \left[ q^M_n \xi J'_m(q^M_n r) \right] e^{jm\phi - \Gamma^M_n z} - T^E_{n3} \left[ j\zeta \frac{Z_o m}{q^E_n r} \cdot J_m(q^E_n r) \right] e^{jm\phi - \Gamma^E_n z} \right] . \qquad \text{(C-25)}$$

Similarly all components of H fields in the region 3 are

$$H_z = \sum_n T^E_{n3} J_m(q^E_n r) e^{jm\phi - \Gamma^E_n z} , \qquad \text{(C-26)}$$

$$H_\phi = \sum_n \left[ T^M_{n3} \{ -\zeta Y_o J'_m(q^M_n r) \} e^{jm\phi - \Gamma^M_n z} + \{ T^E_{n3} \frac{jm}{r} \xi J_m(q^E_n r) \} e^{jm\phi - \Gamma^E_n z} \right] , \qquad \text{(C-27)}$$

and

$$H_r = \sum_n \left[ T^M_{n3} \{ j\zeta \frac{Y_o m}{q^M_n r} J_m(q^M_n r) \} e^{jm\phi - \Gamma^M_n z} \right.$$

$$\left. + \{ T^E_{n3} q^E_n \xi J'_m(q^E_n r) \} e^{jm\phi - \Gamma^E_n z} \right] \qquad \text{(C-28)}$$

Tangential components of E and H fields are matched at the air-plasma interface z=0, $\ell$. The reflection and transmission coefficients R's and T's are determined by the point-matching method.

BIBLIOGRAPHY


1. Allis, W.P., Buchshaum, S.J. and Bers, A., "Waves in Anisotropic Plasmas", The M.I.T. Press, Cambridge, Mass. (1963).

2. Barber, N.F. and Crombie, D.D., "V.L.F. Reflections from the Ionosphere in the Presence of a Transverse Magnetic Field", J. Atmosph. Terr. Phys., Vol. 16, Nos. 1/2, pp. 37-45, (Oct., 1959).

3. Bate, R.T., Willardson, R.K. and Beer, A.C., "Transverse Magnetoresistance and Hall Effect in n-type InSb", J. Phys. Chem. Solids, Vol. 9, No. 2, pp. 119-128 (Feb., 1959).

4. Beerman, H.P., "Pyroelectric Infrared Radiation Detector", American Ceramic Society Bulletin, Vol. 46, No. 8, pp. 737-740 (Aug., 1967).

5. Breeden, K.H. and Sheppard, A.P., "A Note on the Millimeter and Submillimeter Wave Dielectric Constant and Loss Tangent Value of Some Common Materials", Radio Science, Vol. 3, No. 2, pp. 205 (Feb., 1968).

6. Carlile, R.N., "Quasi-$TE_{11}$ Modes in an Anisotropic Plasma-Waveguide", IEEE Trans. on Microwave Theory and Techniques, Vol. MTT-14, pp. 350-351 (July, 1966).

7. Champlin, K.S., Glover, G.H., and Holm-Kennedy, J.W., "Plasma-Filled Waveguide with Axial Magnetization. II.Scattering by a Section of Finite Length", J. Appl. Phys., Vol. 40, No. 9, pp. 3538-3544 (Aug., 1969).

8. Clarricoats, P.J.B., Private communication (1970).

9. Collin, R.E., "Field Theory of Guided Waves", McGraw-Hill Book Company, Inc., New York (1960).

10. Davies, K., Ionospheric Radio Waves, Blaisdell Publishing Co., Waltham (1969).

11. Duncan, B.J. and Swern, L., "Effects of Zero Ferrite Permeability on Circularly Polarized Waves", Proc. I.R.E., Vol. 45, pp. 647-655 (May, 1957).

12. Ehrenreich, H., "Transport of Electrons in Intrinsic InSb", J. Phys. Chem. Solids, Vol. 9, No. 2, pp. 129-148 (Feb., 1959).

13. Evenson, K.M., Private communication, N.B.S. (1970).

14. Fox, A.G., Miller, S.E. and Weiss, M.T., "Behavior and Applications of Ferrites in the Microwave Region", Bell Syst. Tech. J., Vol. 34, No. 1, pp. 5-103 (Jan., 1955).

15. Gebbie, H.A., Stone, N.W.B. and Findlay, F.D., "A Stimulated Emission Source at 0.34 Millimeter Wavelength", Nature, 202, No. 4933, pp. 685 (May, 1964).

16. Harvey, A.F., "Coherent Light", Wiley-Interscience, New York (1970).

17. Hogarth, C.A., "Materials Used in Semiconductor Devices", Interscience Publishers, New York (1945).

18. Hirota, R. and Suzuki, K., "Propagation of Waves in a Bounded Solid State Plasma in Transverse Magnetic Field", J. Phys. Soc. Japan, Vol. 21, No. 6, pp. 1112-1118 (June, 1966).

19. Hogan, C.L., "The Ferromagnetic Faraday Effect at Microwave Frequencies and its Applications", Rev. Mod. Phys., Vol. 25, pp. 253-263 (Jan., 1953).

20. Johnson, V.A. and Whitesell, W.J., "Theory of the Magnetoresistive Effect in Semiconductors", Phys. Rev., Vol. 89, No. 5, pp. 941-947 (March, 1953).

21. Kanda, M., Masclet, G., May, W.G., and Hayes, R.E., "The Application of Semiconductors to Quasi-Optical Isolators for Use at Submillimeter Wavelengths", NASA Report No. NGL06-003-088, University of Colorado, Boulder, Colorado (April, 1970).

22. Kanda, M., "HCN Laser", to be published (1971).

23. Kuno, H.J. and Hershberger, W.D., "Microwave Faraday Effect and Propagation in a Circular Solid State Plasma Waveguide", IEEE Trans. on Microwave Theory and Techniques, Vol. MTT-15, No. 12, pp. 661-668 (Dec., 1967).

24. Lax, B., and Button, K.J., "Theory of New Ferrite Modes in Rectangular Waveguide", J. Appl. Phys., Vol. 26, No. 9, pp. 1184-1185 (Sept., 1955).

25. Lewis, B.F. and Sondheimer, E.H., "The Theory of the Magneto-Resistance Effects in Polar Semiconductors", Proc. Royal Soc. London, Ser. A, Vol. 227, No. 1169, pp. 241-251 (Jan., 1955).

26. Libchaber, A. and Veilex, R., "Wave Propagation in a Gyromagnetic Solid Conductor, Helicon Waves", Phys. Rev., Vol. 127, No. 3, pp. 774-776 (Aug., 1962).

27. Lide, Jr., D.R. and Maki, A.G., "On the Explanation of the So-called CN Laser", Appl. Phys. Letters, Vol. 11, No. 2, pp. 62-64 (July, 1967).

28. Madelung, O., Physics of III-V Compounds, John Wiley & Sons, Inc., New York (1964).

29. Mathias, L.E.S., Crocker, A. and Wills, M.S., "Laser Oscillations at Submillimeter Wavelengths from Pulsed Gas Discharges in Compounds of Hydrogen, Carbon and Nitrogen", Electronics Letters, Vol. 1, No. 2, pp. 45-46 (April, 1965).

30. McLeod, B.R., Quasi-Optical and Waveguide Applications of Indium Antimonide, Ph.D. Thesis, University of Colorado (May, 1968).

31. McLeod, B.R. and May, W.G., "A 35 GHz Isolator Using a Coaxial Solid State Plasma in a Longitudinal Magnetic Field", IEEE Trans. on Microwave Theory and Techniques, Vol. MTT-19, No. 6, pp. 510-516 (June, 1971).

32. Müller, W.M. and Flesher, G.T., "Continuous Wave Submillimeter Oscillation in Discharges Containing C, N, and H or D", Appl. Phys. Letters, Vol. 10, No. 3, pp. 93-94 (Feb., 1967).

33. Polder, D., "On the Theory of Ferromagnetic Resonance", Phil. Mag., Vol. 40, pp. 99-115 (Jan., 1949).

34. Seaman, J.M., Non-reciprocal Reflection of Microwaves from a Solid State Magnetoplasma, M.S. Thesis, University of Colorado (Aug. 1969).

35. Smith, R.A., "Semiconductors", Cambridge University Press, London (1964).

36. Stratton, J.A., "Electromagnetic Theory", McGraw-Hill Book Co., Inc., New York (1941).

37. Toda, M., "Propagation in a Solid State Plasma Waveguide in a Transverse Magnetic Field", J. Phys. Soc. Japan, Vol. 19, No. 7, pp. 1126-1130 (July, 1964).

38. van der Pauw, L.J., "A Method of Measuring Specific Resistivity and Hall Effect of Discs of Arbitrary Shape", Philips Research Reports, Vol. 13, No. 1, pp. 1-9 (Feb., 1958).

39. Wait, J.R., Electromagnetic Waves in Stratified Media, The McMillan Co., New York (1962).

40. Young, L., "Synthesis of Multiple Antireflection Films Over a Prescribed Frequency Band", J. Opt. Soc. Am., Vol. 51, No. 9, pp. 967-974 (Sept. 1961).